SYNTHESIS AND ANALYSIS OF A MICROCELLULAR PLASTICS EXTRUSION SYSTEM FOR INSULATION OF FINE WIRES

by

YODDHOJIT SANYAL

B.S., Mechanical Engineering
Jadavpur University
1992

M.S., Mechanical Engineering
Villanova University
1994

Submitted to the Department of Mechanical Engineering
in Partial Fulfillment of the Requirements for
the Degree of

DOCTOR OF SCIENCE
IN MECHANICAL ENGINEERING

at the

MASSACHUSETTS INSTITUTE OF TECHNOLOGY

June 1998

Signature of Author____________________________________
Department of Mechanical Engineering
June 5, 1998

Certified by____________________________________
Nam P. Suh
The Ralph E. and Eloise F. Cross Professor of Manufacturing and Head
Department of Mechanical Engineering
Committee Chairman and Thesis Advisor

Accepted by____________________________________
Anthony T. Patera
Professor of Mechanical Engineering and
Chairman of the Departmental Graduate Committee
Department of Mechanical Engineering

SYNTHESIS AND ANALYSIS OF A MICROCELLULAR PLASTICS EXTRUSION SYSTEM FOR INSULATION OF FINE WIRES

by

YODDHOJIT SANYAL

Submitted to the Department of Mechanical Engineering on June, 1998
in partial Fulfillment of the Requirements for the Degree of
Doctor Of Science in Mechanical Engineering

ABSTRACT

This thesis deals with analytical and experimental work performed on the extrusion of microcellular plastics with cell sizes of 20 microns or less and cell densities of about a billion cells per cm^3.

An analytical model of cell nucleation and cell growth during extrusion was developed. This model predicts the nucleation rate by taking into account Gibbs free energy change due to phase separation, as well as surface energy, in binary systems (such as polymer/gas mixtures). The cell growth kinetics during extrusion is also studied under some limiting cases. The analysis shows that due to the simultaneous occurrence of cell nucleation and cell growth during extrusion, these two phenomena are coupled and compete with each other for the gas dissolved in the polymer. With the aid of this model the important extrusion parameters affecting the microstructure of the foam were identified. An order-of-magnitude prediction of cell size, cell density and foam void fraction were made based on realistic numerical values of these parameters.

The next phase of the project consisted of using the analytical model and Axiomatic Design Theory to design a tandem extrusion system for wire coating. Satisfaction of the Independence Axiom showed that the process was controllable. Preliminary analysis of the Information Axiom indicated that the system would be stable. Experiments were performed over a range of conditions to determine their effects on the final wire insulation diameter and capacitance. The experimental results were compared to the analytical predictions to further verify the validity of the model as well as to determine its limitations.

Thesis Supervisor:	Prof. Nam P. Suh, Ph.D.
Title:	The Ralph E. and Eloise F. Cross Professor of Manufacturing and Head of the Department of Mechanical Engineering

ACKNOWLEDGMENTS

I would like to thank my advisor, Professor Nam Pyo Suh, for his guidance and support throughout this research work. Through his mentoring he has always inspired me to be undauntingly creative and rigorously analytical at the same time. He has instilled in me a true passion for engineering and I shall always strive to be the best wherever I go from here.

I would also like to thank Professor Chris Scott and Dr. Nannaji Saka for their help and guidance as a members of my thesis committee. Their help in developing the analytical model was something I could not afford to do without in this research endeavor. Dr. Eugene Skiens at Precision Interconnect deserves special mention for his efforts in coordinating the research between Precision Interconnect and MIT. Without his support and encouragement the goals of this research work could never have been met. Doris Beck and Art Buck at Precision Interconnect have also been a constant source of technical support, help and information.

The Laboratory for Manufacturing and Productivity has provided a supportive environment for performing this research. Sally Stiffler has been an immense help as a financial wiz and as a dear friend. Karuna Mohindra has been one of the warmest and sweeetest people during my four years in the LMP. I would like to thank Fred Cote and Gerry Wenthworth for all their expertise and help in machining the many components of the extrusion system. I would like to thank Chin Yee Ng for his friendship and his immensely important part in this research work. The fabrication of the tandem extrusion system was done by the two of us as a team. Yes, I think we made a great team and I would like to thank him for teaching me a lot about working on a project that is "hands-on". I would like to thank Ravi Patil and Torsten Hermann for introducing me to this project and teaching me the first basic things about extrusion and equipment operation. The undergraduate students who helped in the fabrication of the equipment were Wendy Cheng and Paul Balun. Wendy and Paul did a truly outstanding job and often went beyond all expectations in their roles as undergraduate researchers. I would also like to thank Gabriel Gomez, Mark Sun and Jen Cho for their help in running experiments and their admirable patience while doing so.

My parents have been a constant source of encouragement during all my academic endeavors. Their love and support have constantly kept me going. It was my family's respect for intellectual growth and accomplishment that has led me along the path of achievement in the field of higher learning. My uncle Bish and my aunt Diane are have always edged me along this path. They have also provided a haven for me during my stay in Boston. Their love, help, encouragement, and friendship has helped me over so many rough spots during my four years here at MIT. My aunt Sreelekha and uncle Ashish have also given me so much love, affection, and encouragement to excel academically, that I cannot even thank them enough. They have also a given me a great place to spend a few days at whenever I felt the urge take a break from my usual stressful routine and get spoiled.

Lastly, I would like to thank Alessandra for all her love and for believing in me. We have been through a lot these past few years. Together, we have had to cope with the pressures of graduate school, professional aspirations, and the unexpected and often painful circumstances that life has thrown at us. Together, we can look ahead to a new tomorrow and a new chapter in our lives. You are truly the most precious thing that I have earned at MIT.

TABLE OF CONTENTS

LIST OF FIGURES

LIST OF TABLES

NOMENCLATURE

a	shield correction factor [dimensionless]
A	interfacial area [m^2]
A	cross sectional are of extrudate [m^2]
A*	Avagadro number [gmole^{-1}]
c	gas concentration in polymer/gas mixture [moles/m^3]
c_{eq}	equilibrium concentration of gas in polymer [g gas/ g polymer]
c_{pol}	polymer concentration in polymer/gas mixture [moles/m3]
C	capacitance [F]
C_p	specific heat of foam [J/kg K]
d_b	average bubble diameter [m]
d_{bw}	bare wire diameter [in]
d_{cw}	coated wire diameter [in]
D	diffusion coefficient of gas in polymer [m2/sec]
f	stranding correction factor [dimensionless]
f	mass flux of gas at cell/solution interface [gas moles/m^2-sec]
F	frequency [MHz]
G_A	Gibbs free energy of component A [J]
G_B	Gibbs free energy of component B [J]
G_{AB}	Gibbs free energy of mixture of A and B [J]
ΔG	change in Gibbs free energy [J]
ΔG_v	change in volume free Gibbs free energy [J]
ΔG_s	change in surface Gibbs free energy [J]
g_m	Gibbs free energy of mixing per molecule [J/molecule]
G_m	Gibbs free energy of mixing [J]
h	forced heat transfer coefficient [W/m^2 K]
J	nucleation rate [nuclei/m^3-sec]
k	Boltzman constant [J/K]
K	dielectric constant [dimensionless]
K	thermal conductivity of foam [J/m K]
L	die length
K_s	Henry's constant [g gas/g polymer-Pa]
$\overset{o}{M}$	mass flow rate into gas cell [moles/sec]
$\overline{M}_A$	molecular weight of A [dimensionless]
$\overline{M}_B$	molecular weight of B [dimensionless]
$\overline{M}_{gas}$	molecular weight of gas [dimensionless]
$\overline{M}_{mon}$	molecular weight of monomer group [dimensionless]
N	total number of molecules of A and B in mixture
N	extruder screw speed [rpm]
N_{gas}	number of gas molecules
$N_{monomer}$	number of monomer groups
P	pressure [Pa]
P	perimeter of extrudate [m]
P_i	die inlet pressure
P_o	die outlet pressure
ΔP	pressure drop across die [Pa]
P_g	pressure inside gas cell [Pa]

$(P_g)_{outlet}$	pressure inside gas cell at die outlet [Pa]
Q	volume flow rate of foam [m^3/sec]
Q_D	drag volume flow rate [m^3/sec]
Q_P	pressure volume flow rate [m^3/sec]
r	radius of gas cluster [m]
r	die radius [m]
r_{crit}	radius of critical cluster [m]
$R_{crit}(t^*)$	radius of critical cluster nucleated at time t* [m]
R	universal gas constant [J/gmole K]
R_{cell}	radius of gas cell [m]
s	striation thickness [m]
t_{res}	residence time in die [sec]
T	temperature [K]
T_{air}	air temperature [K]
$U(P)$	energy of interaction between molecules of A and B [J]
V	volume [m^3]
V	velocity of foam [m/sec]
V	wire velocity [m]
V_{prop}	velocity of signal propagation [% speed of light]
v_{av}	average flow velocity inside die [m/sec]
v_g	volume of single gas molecule [m^3]
W	mean circumference of die annular space [m]
W^*	extruder screw channel width [m]
H	die annular thickness [m]
H^*	extruder screw channel depth [m]
z	coordination number for polymer molecule
z	coordinate along the flow direction
Z_o	impedance [Ω]

β	constant in fin equation [m^{-2} $sec\text{-}^{1}$]
ϕ_v	volume fraction of gas [dimensionless]
γ	mean strewtching ratio of gas component [dimensionless]
$\dot{\gamma}$	shear rate [s-1]
λ	viscosity ratio of gas to polymer [dimensionless]
μ	polymer viscosity [Pa/s]
η_g	dynamic viscosity of gas [Pa-s]
η_p	dynamic viscosity of polymer matrix [Pa-s]
θ	difference between foam and air temperature [K]
ρ	density of foam [kg/m^3]
ρ_p	density of foam [kg/m^3]
σ	polymer surface tension [N/m]
τ_{diff}	time for diffusion of gas in polymer [sec]
Ω	pre-exponential factor for homogeneous nucleation [nuclei/m^3-sec]
ξ	molecule fraction of gas in polymer/gas mixture [dimensionless]
ψ	ratio of gas mass to polymer mass

CHAPTER 1

INTRODUCTION

1.1 INTRODUCTION

The wire and cable industry is the largest consumer of plastics in the electronics sector, accounting for roughly half of the total polymer usage (Graff, 1993). The consumers include the communications, test equipment, and medical industries. Coaxial cables carry bundles of wires which can be as small as 25 µm in diameter. Each coaxial cable can carry several hundred wires. The possibility of cross-talk between these different channels poses a serious design problem. In such designs the performance of the primary insulation which is in the form of some appropriate dielectric material is of crucial importance. The dielectric insulation also separates the conducting wire from the grounded sheath located just outside the wire.

In keeping with the world-wide trend in electronics technology, the recent thrust has been toward miniaturization of wires and coaxial cables. Such developments have led to high performance standards being demanded of the dielectric insulation. Miniaturization restricts insulation thickness on the wires. At the other extreme, the quality of the insulation requires a low dielectric constant and higher velocity of signal propagation through the wire.

1.2 COAXIAL CABLE PERFORMANCE

The key performance characteristics of coaxial cables have evolved as a result of experience over several decades. Several empirical relations are widely used in the cable industry to characterize cable performance. These characteristics are now briefly reviewed (Patil, 1995).

(1) Velocity of propagation:

The speed at which data can be transmitted through a coaxial cable is called the velocity of propagation and is expressed as a percentage of the velocity of light.

$$V_{prop}(\%) = \frac{100}{\sqrt{K}} \tag{1.1}$$

where,

K=Dielectric constant of insulation

(2) Capacitance:

$$C = \frac{7.359}{\log[d_{cw} + a] - \log[f\, d_{bw}]}K \quad (1.2)$$

where,

a = Shield correction factor

d_{bw} = Bare wire diameter

d_{cw} = Coated wire diameter

f = Stranding correction factor

(3) Impedance:

$$Z_o = \frac{138}{\sqrt{K}}\left[\log(d_{cw} + a) - \log(f\, d_{bw})\right] \quad (1.3)$$

(4) Attenuation:

$$G = 4.34\frac{R_t}{Z_o} + 2.75lF\sqrt{K} \quad (1.4)$$

where,

$R_t = 0.1[1/d_{bw} + 1/d_{cw}]\sqrt{F}$ = line resistance

F = frequency

λ = power factor

(5) Time delay:

$$t_d = 1.016\sqrt{K} \quad (1.5)$$

1.3 EFFECT OF FOAMING ON INSULATION

A review of the empirical relations in Section 1.2 shows that all the performance parameters are dependent on the dielectric constant K. Foaming the insulation reduces the dielectric constant significantly, and leads to the following desirable changes in the performance parameters:

(1) Increases velocity of propagation,
(2) Reduces capacitance,
(3) Reduces impedance,
(4) Lowers attenuation, and
(5) Lowers time delay.

1.4 MICROCELLULAR FOAMS

Microcellular foams are characterized by extremely small cell sizes (of the order of 10 μm) and very high cell densities (about a billion cells/cm^3). Due to these two characteristics, microcellular foams have very high void fractions. Such morphology reduces material consumption when plastic parts are made in large quantities. In most applications the mechanical, electrical and thermal properties of the final foamed product are considerably improved. Since the cell size of microcellular foams is smaller than the preexisting natural flaws in the original polymer, the final foamed product exhibits superior stiffness-to-weight ratio, impact strength, toughness, and fatigue life. Toughness and fatigue life have shown a five-fold and fourteen-fold increase respectively over unfoamed samples (Patil, 1995). Stiffness-to-weight ratio has been shown to increase by a factor of three to five (Collias and Baird, 1992; Seeler and Kumar, 1992, 1993). Density reductions in the range of 30-50% of the original unfoamed material are commonly observed in microcellular foams. The presence of billions of microvoids in the polymer matrix also reduces the thermal conductivity and dielectric constant of the original material (Patil, 1995).

Microcellular foaming technology also uses environmentally safe gases such as carbon dioxide and nitrogen instead of the conventional chlorofluorocarbons (CFCs) and hydrochlorofluorocarbons (HCFCs) which are harmful to the ozone layer. Since the CFCs are gradually being phased out all over the world, alternative foaming techniques such as microcellular processing will receive increased attention.

Microcellular foaming technology has been extended to a wide class of polymer materials such as amorphous thermoplastics, semicrystalline thermoplastics, liquid crystal polymers, elastomers, thermosets, and fluoropolymers. Microcellular plastics technology was originally developed by Martini and Suh (1984). Waldman (1982) investigated the mechanical properties of such foams. A process for producing light-weight polymer composites (LPCs) was developed by Youn (Youn, 1984; Youn and Suh, 1984). Modeling of nucleation in microcellular plastic foaming was performed by Colton (Colton and Suh, 1986; Colton and Suh, 1987 abc; Colton and Suh, 1990) who also explained the behavior of various additives and processing conditions on the number of bubbles nucleated. A semicontinuous thermoforming process was developed by Kumar (Kumar, 1988; Kumar and Suh, 1989, 1990). The use of supercritical carbon dioxide in producing foams was introduced by Cha et al. (1991) while the first system for extrusion of such foams was developed by Park (1993). Baldwin (1994) extended the extrusion process to include sheets while Patil and Herrmann were successful in the initial efforts to develop a wire coating line (Patil, 1995; Herrmann 1995). Patil also performed batch processing of fluoroploymers. Ng developed a tandem extrusion system capable of continuous and stable production of filaments (Ng, 1997).

1.5 RESEARCH MOTIVATIONS AND OBJECTIVES

The present manufacturing process for coaxial cables consists of winding fluoropolymer tape around the wire. This process has many disadvantages, such as a slow rate of production and controllability. The overlapping of the tape in certain regions leads to an undesirable periodic nonuniformity in the insulation thickness. Moreover, when a coaxial cable is in use, a 90° turn can cause the tape to kink or even tear causing failure of the cable.

This research proposes a solution in the form of extruded thin-walled microcellular coatings. The high void fractions result in low dielectric constants and reduce material consumption while maintaining the mechanical strength required during bending. Moreover, even the use of inexpensive polymers such as polyolefins instead of fluoropolymers can suffice in most applications since after foaming the dielectric constant is considerably reduced. The objective of this thesis, accordingly, is to develop a stable and controllable extrusion process for producing wire coatings. The research also seeks to develop a quantitative model to predict the microstructure of the final insulation based on understanding the kinetics of nucleation in binary systems and the dynamics of the cell growth process during extrusion. Once such a quantitative model is developed, the objective of the research is to evaluate the importance of various extrusion parameters in the production of profiles including wire coatings.

1.6 THESIS OUTLINE

The thesis begins with a review of the basic process of microcellular foaming in Chapter 2. It discusses the steps of cell nucleation and growth in batch processing. The mechanism of polymer/gas solution formation in extrusion process is also reviewed in this chapter. Chapter 3 outlines the process of wire coating as it is done in industry today. Some important equipment used in wire coating applications are detailed.

Chapter 4 discusses in detail the quantitative model that was developed to predict nucleation rate and cell growth rates during extrusion. This chapter discusses the thermodynamics of phase separation in binary systems and utilizes the results to derive explicit quantitative predictions of nucleation rates. It also discusses the mechanism of cell growth and shows how the nucleation and cell growth phenomena occur concurrently during extrusion and hence compete for the available gas in solution in the polymer.

Chapter 5 discusses the basic theory of Axiomatic Design which was used throughout this research work as a framework for developing the extrusion system. Chapter 6 discusses how the principles of Axiomatic Design were utilized to design a controllable and stable extrusion process. Chapter 7 outlines the design specifications for all the major components used in the extrusion system.

The experimental procedures and the results are described in Chapter 8. The experiments were performed with both filament extrusion dies as well as wire coating dies. These experimental results are compared with the theoretical predictions made with the aid of the model developed in Chapter 4. Finally, Chapter 9 concludes the research work with recommendations and suggestions for future work.

CHAPTER 2

REVIEW OF MICROCELLULAR PLASTICS TECHNOLOGY

2.1 INTRODUCTION

In order to develop a controllable and stable continuous extrusion system for producing microcellular foams, a review of the basic steps required in processing of microcellular foams is needed. Microcellular plastics were invented in the early 1980's by researchers at MIT. The initial research in the field of microcellular plastics consisted of batch processing. Such processing methods involved the saturation of a piece of plastic in a pressure chamber and then subjecting the saturated sample to a rapid pressure drop to nucleate and grow billions of gas nuclei. This chapter discusses this basic process of batch processing and then describes the development of a process to form polymer gas solutions continuosly (Park, 1993) for producing extruded micrcellular profiles. It also describes a modified extrusion system known as a tandem extrusion system to make the process of solution formation more controllable.

2.2 THEORY OF MICROCELLULAR PLASTICS

The basic theory behind microcellular technology can be summarized by Figure 2.1. The first step comprises of the formation of a saturated solution of polymer and gas. The equilibrium concentration of a gas in a polymer (i.e., the solubility of the gas in the polymer) is a function of pressure and temperature (Durril and Griskey, 1966 and 1969; Koros and Paul, 1980; Lundberg et al., 1966; Newitt and Weale, 1948; Van Krevelen, 1976; Veith et al., 1966; Weinkauf and Paul, 1990) and is expressed as the following relation:

$$dc_{eq} = dc_{eq}(P,T) = \left(\frac{\partial c_{eq}}{\partial P}\right)_T dP + \left(\frac{\partial c_{eq}}{\partial T}\right)_P dT \qquad (2.1)$$

Point B denotes such a saturated solution. If a sudden change in pressure or temperature (or both) is induced, then the system of polymer and gas ends up at point C where the solubility of the gas in the polymer is lower than at point B. Consequently, some of the gas which was previously dissolved in the polymer (at B) will now come out of solution by the mechanism of nucleation. The thermodynamic instability induced by rapid change in pressure and temperature thus causes the nucleation of billions of microvoids inside the polymer matrix. Following the primary step of cell nucleation, the second step consists of the growth of these nucleated cells to their final size.

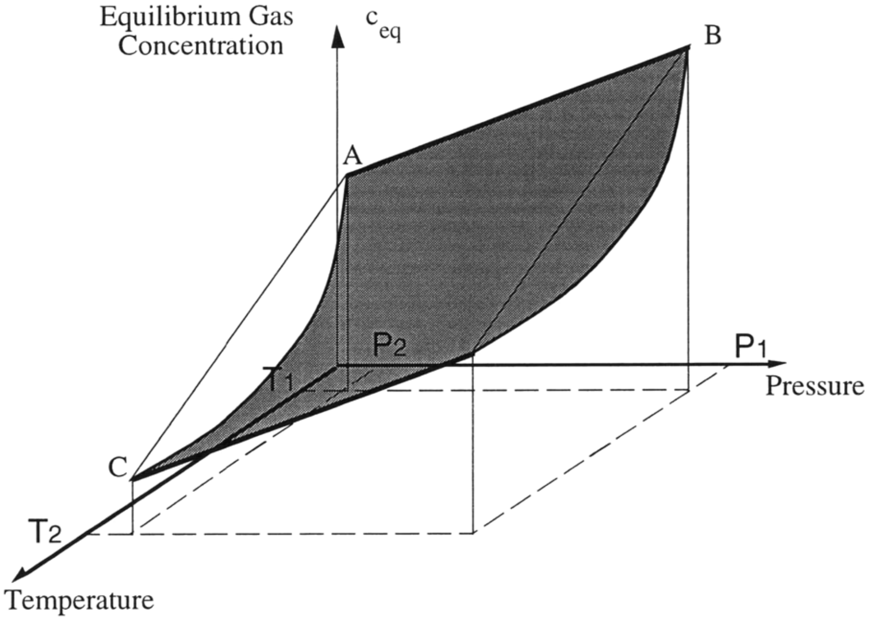

Figure 2.1 Schematic of microcellular foaming process.

2.3 CONTINUOUS PROCESSING OF MICROCELLULAR FOAMS

The previous section described the two basic steps for microcellular foaming. However, the process needs to be adapted to continuous processing at industrially feasible rates. The key steps in the continuous processing are summarized in Figure 2.2. The first step consists of processing or plasticating the polymer (which can be done in a plasticating extruder). The second step consists of introducing gas into the polymer melt and the subsequent formation of a polymer/gas solution. The third step is the nucleation of microvoids through the inducement of a rapid thermodynamic instability. Since rapid pressure drops are much easier to achieve in practice than rapid temperature rise, therefore the choice of rapid pressure drop is the obvious solution. The fourth and final step consists of simultaneous shaping of the nucleated flow into the desired cross section as well as the growth and stabilization of the nucleated cells.

Of the above four steps, only the step consisting of forming polymer/gas solutions is discussed in this Chapter in detail. The first step of plasticating has been studied by Baldwin (1994). The steps consisting of nucleation and cell growth and shaping are analyzed in detail in Chapters 4 and 8.

2.4 GAS DISSOLUTION IN POLYMER IN CONTINUOUS PROCESSING

The first step in the gas dissolution process is to estimate the equilibrium gas concentration in the polymer melt, i.e., the maximum amount of gas that can be dissloved in the melt at a particular pressure and temperature. This is the amount of gas needed to form a saturated solution and this can be estimated using Henry's Law (Park, 1993; Baldwin, 1994). Henry's Law gives the equilibrium gas concentration as

$$C_s = K_s\, P_s \tag{2.2}$$

where,

C_s=Equilibrium gas concentration

K_s=Henry's constant which is particular for a chosen combination of polymer and gas

P_s=Saturation pressure

Using the data of Durril and Griskey, Park (1993) concluded that for a saturation pressure of 4000 psi (27.6 Mpa) and temperature of 200°C, the equilibrium concentration of carbon dioxide and nitrogen in most polymers is about 10 percent and 2 by weight.

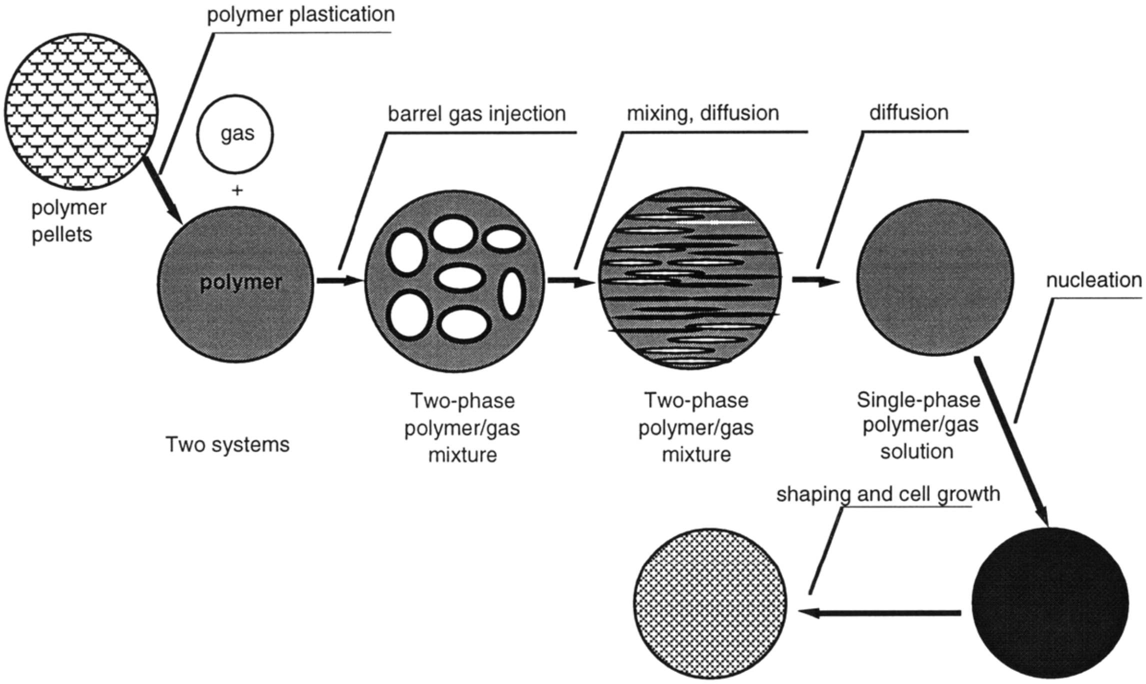

Figure 2.2 Key steps in continuous production of microcellular plastics.

Dispersive mixing

Once a stream of high pressure gas has been injected into the polymer stream, dispersive mixing theory can be used to study the dispersion of the gas bubbles in the polymer melt during continuous processing. The interfacial area per unit volume, A/V, is a key parameter quantifying mixing. The striation thickness is defined as the average distance between interfaces of the same component in the mixture and is given by the following relationship:

$$s = \frac{2}{A/V} \tag{2.3}$$

Using the results of Mohr et al. (1957) and Kim et al. (1972), the striation thickness can be expressed as

$$s \approx \frac{d_b}{\Phi_v \gamma} \tag{2.4}$$

where d_b is the average diameter of the dispersed bubbles, ϕ_v is the volume fraction of the gas, and γ is the mean stretching ratio of the gas component given by

$$\gamma = \frac{d_{max}}{d_b} \tag{2.5}$$

where d_{max} is the maximum diameter of the elongated bubbles in a shear field.

The mean stretching ratio γ was experimentally estimated by Park and Suh (1992a). The initial void fraction ϕ_v of carbon dioxide in the polymer was calculated by Park to be about 0.22. The average bubble diamter d_b was calculated by Park using the critical Weber number for a gas phase in a continuos phase of polymer melt.

$$We = \frac{\text{shear forces}}{\text{surface forces}} = \frac{\dot{\gamma} d_b \eta_p f(\lambda)}{2\sigma} \tag{2.6}$$

where,

$$f(\lambda) = \frac{19\lambda + 16}{16\lambda + 16} \tag{2.7}$$

λ=viscosity ratio (=η_g/η_p)

η_g=dynamic viscosity of gas, Pa-s

η_p=dynamic viscosity of polymer matrix, Pa-s

$\dot{\gamma}$ =shear rate in extruder, s^{-1}

d_b=average bubble diameter, m

σ=surface tension, N/m

For polymer/gas systems the critical Weber number is estimated to be about 300 (Karan and Bellinger, 1968). The Weber number is the ratio of shear forces to surface tension forces. Based on the work done by Weber, Park estimates that an extruder screw rotating at 90 rpm and having a diameter of 19 mm and channel depth of 0.8 mm will disintegrate the initially injected gas bubbles into small bubbles of 1mm diameter.

Gas Diffusion

Diffusion coefficient of carbon dioxide in polypropylene is about 4.2 x 10^{-5} cm^2/sec (Durril and Griskey). For the disintegrated gas bubbles of 1mm diameter the estimated striation thickness is 90 microns (Park, 1993). From this striation thickness and the diffusion coefficient, the diffusion time can be estimated as

$$\tau_{diff} \sim s^2 / D = 80 \text{ sesonds}$$

2.5 TANDEM EXTRUSION SYSTEM FOR POLYMER/GAS SOLUTION FORMATION

A tandem extrusion system (Ng, 1997) which consists of two separate extruders is shown in Figure 2.3. The first extruder (also known as the primary extruder) has a plasticating section which essentially serves the dual purpose of solids conveying and melting of the polymer pellets. After the pellets have been melted, a stream of high pressure gas (N_2 or CO_2) is injected into the melt. The rest of the primary extruder serves as a dispersive mixer which breaks down the injected gas stream into smaller and smaller bubbles through mechanical energy input. At the same time this section of the extruder (i.e., the section after the gas injection port) acts as a melt pump which serves to build up the pressure of the polymer melt.

After exiting this primary extruder the melt is fed into a secondary extruder. This secondary extruder acts mainly as a melt pump which pressurizes the melt. This extruder also acts a diffusion chamber which provides enough residence time for the dispersed gas bubbles to diffuse into the polymer melt and form a single-phase homogeneous solution. It should be noted that the temperature of the melt can be very effectively controlled in this secondary extruder in order to adjust the viscosity of the melt.

After the secondary extruder, the melt is fed into a crosshead and a wire coating die. The crosshead turns the flow through 90 degrees and is then extruded through the die. The die serves the dual function of being a shaping as well as a nucleating device (because of the rapid pressure drop across its length).

Since two extruders are connected in series in this tandem arrangement, the residence time of the melt and injected gas bubbles in the extruder is much larger than is the case in a single screw extruder. Thus, the formation of a single phase homogeneous solution is aided by the use of a tandem extrusion system. Moreover, the first extruder speed can be high to aid in dispersive mixing while the second extruder speed can be kept low and adjusted independently to control the overall flow rate. Thus, the use of a tandem extrusion system would be ideal for microcellular processing since it would simplify the process of solution formation.

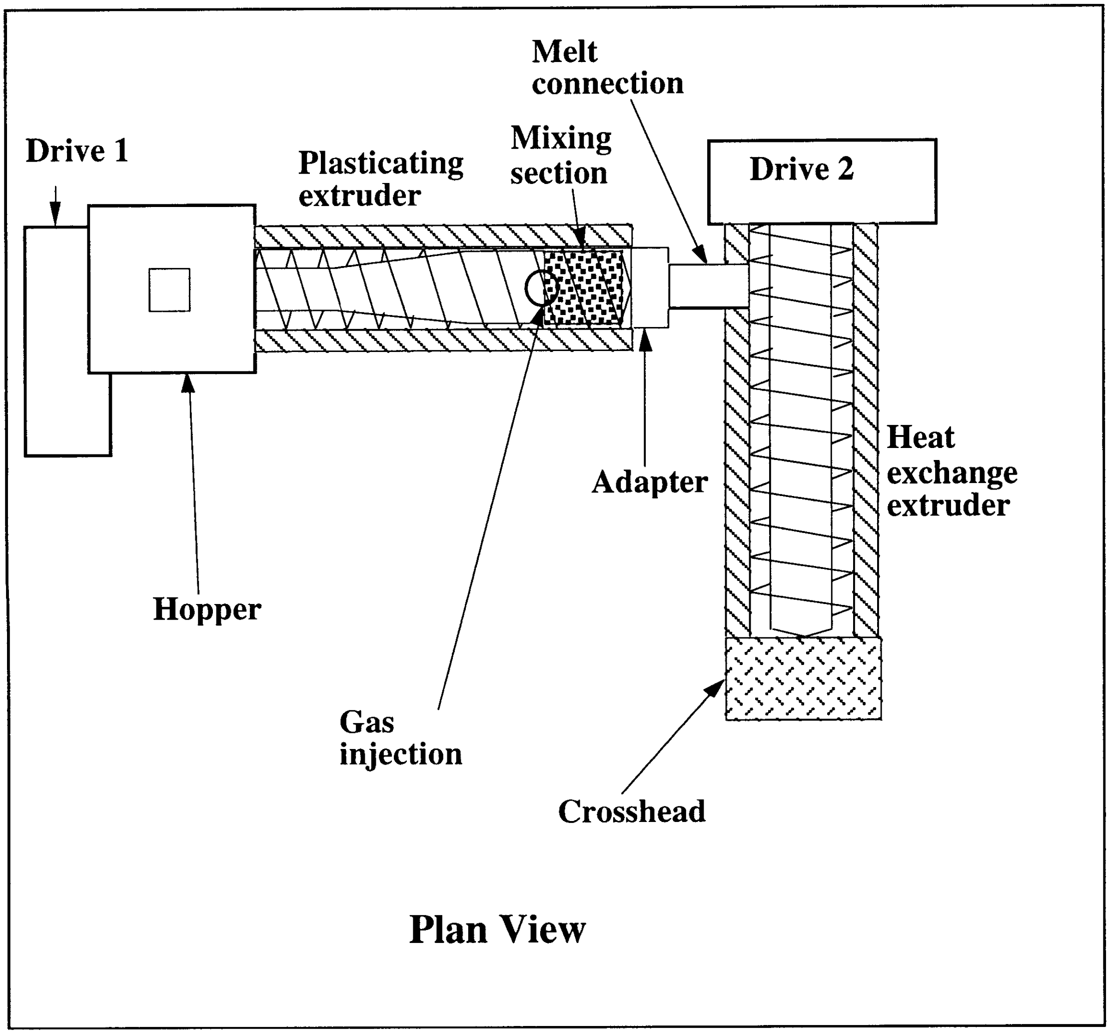

Figure 2.3 Tandem extrusion system for polymer/gas solution formation.

2.4 CONCLUSION

In this chapter the basic mechanism of microcellular processing has been studied. The work done by Park(1993) and Baldwin (1994) to form polymer/gas solutions in continuous microcellular processing has been reviewed. Based on this past research on polymer/gas solution formation, an improved system has been suggested which utilizes two extruders connected in series to form a polymer/gas solution. This extrusion setup is discussed in detail in Chapter 7 and has been utilized in this research work to continuously form polymer/gas solutions and extrude profiles with microcellular cell morphology.

CHAPTER 3

EXTRUSION OF WIRE COATING

3.1 INTRODUCTION

Since the wire and cable industry is the largest consumer of plastics in the electronics industry, therefore the extrusion of plastic insulation onto wires has been a technology studied, analyzed, and optimized for a long time. There are two kinds of insulation that are extruded. A *primary insulation* is the first coating or covering on an uninsulated wire. It consists of the conductor directly in contact with the plastic. *Jacketing* or *sheathing* consists of covering a wire or a group of wires with a plastic coating for mechanical or other nonelectric protection. Jackets are often put on wires already having primary insulation. This chapter reviews some of the basic concepts related to the wire coating process

3.2 PROCESS DESCRIPTION

Extrusion of wire coating in the form of insulation is a process in which the molten plastic is extruded into a crosshead through which the wire to be coated passes. On emerging from the crosshead, the coated wire is quenched in a water bath, continuously tested, and then wound on a reel. The process is shown schematically in Figure 3.1.

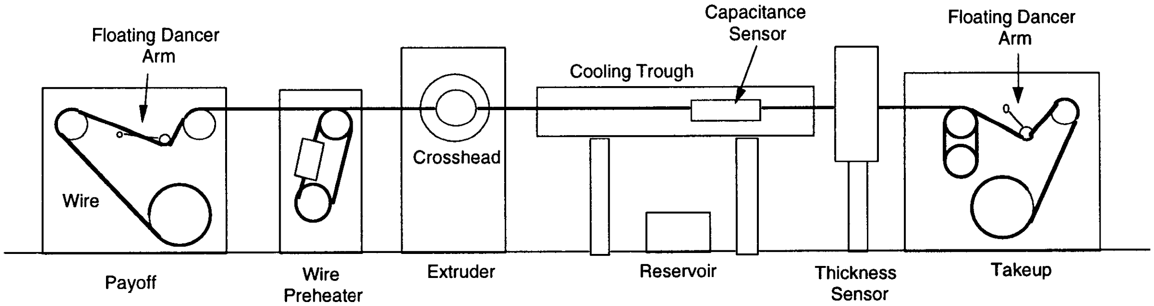

Figure 3.1 Schematic of wire coating process.

3.3 WIRE COATING EQUIPMENT

The equipment required for a wire coating line are now discussed.

3.3.1 Extruders

The range of wire sizes that are coated with the extrusion method is large. Wires from 0.008" diameter to cables as large as 5" in diameter can be coated by the process. Extruders from 1 in. to 10 in. diameters are appropriate for the range of wire sizes mentioned above. Flowrates can vary from 10 lb/hr to as large as 1000 lb/hr.

3.3.2 Crosshead

A conventional crosshead schematic is shown in Figure 3.2. The function of the crosshead is to turn the flow of the polymer being fed into it from the extruder by 90°. The deflector in the crosshead streamlines the flow which flows along the annular region between the inside of the crosshead and the core tube. The wire passes through the guide tip.

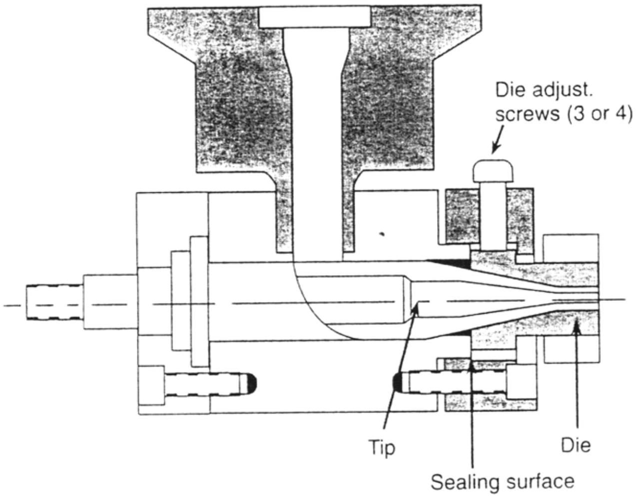

Figure 3.2 Wire coating crosshead.

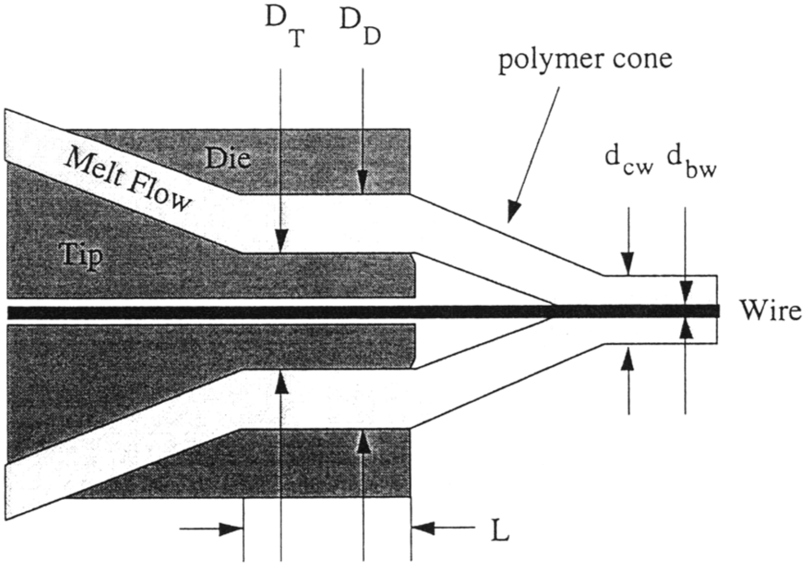

Figure 3.3 Tube die.

3.3.3 Wire Coating Dies

There are two types of wire coating dies resulting in two types of wire coating process.

Tube Die

A tube die is shown schematically in Figure 3.3. In this case the coating is first extruded in the form of a tube and then drawn down onto the bare conductor. The drawing down is achieved by means of applying a vacuum through the same passage in which the conductor travels. Tubing dies require a larger clearance between the conductor and the passage because the vacum must be drawn through the passage. The typical clearance is about 0.010 in. while the strength of the vacuum should be about 1 inch of mercury

The draw down ratio for a tube die is the ratio of the area of the annular die opening to the cross-sectional area of the finished insulation.

$$\mathrm{DDR} = \frac{D_D^2 - D_T^2}{d_{cw}^2 - d_{bw}^2} \tag{3.1}$$

The draw down ratio can vary from one material to another. If the draw down ratio is too large, then the large internal stresses will lead to rough surface finish. Typical draw down ratios are as follows:

Nylon:	4.0
Vinyls:	1.5
Low-density polyethylenes:	1.5
High-density polyethyelene:	1.2

Another important parameter for use of tube dies is the draw ratio balance which can be summarized as

$$\mathrm{DRB} = \frac{D_D/d_{cw}}{D_T/d_{bw}} \tag{3.2}$$

The draw ratio balance should be approximately equal to unity.

Pressure Dies

A pressure die is shown in Figure 3.4 where the conductor comes in contact with the plastic inside the die. The die opening is very close to the final insulation outside diameter. The plastic swelling at the die is compensated for by adjusting the wire speed which leads to a slight drawdown. The clearance betwen the bare conductor and the passage through the guide tip is usually small (about 0.002 or 0.003 in.) which prevents the plastic from entering the passage and obstructing the conductor.

3.3.4 Cooling Trough

After the wire has been coated it passes through the cooling trough where the wire is cooled down to room temperature. The length of the cooling trough is an important consideration since the rate of cooling will determine the length of the water bath required. In most applications the length of cooling trough is about 15 to 20 feet.

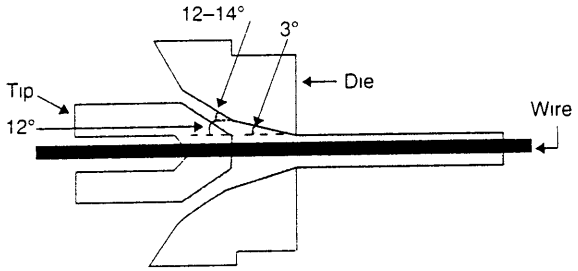

Figure 3.4 Pressure die.

3.4 CONCLUSION

In this chapter a description of the basic industrial process of wire coating has been outlined. The list of basic extrusion equipment required for the process has also been presented. When the method of foaming is applied to wire coatings, some important changes need to be made to some of the equipment such as the crosshead and the dies. These new designs are discussed in Chapter 7 in detail.

CHAPTER 4

THEORETICAL MODEL OF CELL NUCLEATION AND CELL GROWTH DURING EXTRUSION OF MICROCELLULAR PLASTICS

4.1 INTRODUCTION

The key steps involved in the extrusion of microcellular plastics are outlined in Chapter 2. The process of solution formation during extrusion has been analyzed extensively by Park (1993). The mechanism of nucleation and cell growth was first studied by Martini (1981) using classical nucleation theory applied to batch processing. This Chapter treats the mechanism of cell nucleation in an extrusion process using the Gibbs free energy of mixing in binary component systems and applying it to classical nucleation theory. The method of cell growth has also been studied by analyzing the diffusion and Navier Stokes Equation for bubble growth in an isothermal Newtonian fluid. Since the cell nucleation and growth process take place simultaneously inside the die in an extrusion process, these two mechanisms are inherently coupled and the guiding equations need to be solved simultaneously in order to fully understand and comprehend the nature of the foaming process. After making several simplifying assumptions and approximations, a computer code is developed to solve the equations numerically. It should be mentioned that the solutions are only rough and approximate and give only order-of-magnitude estimates of final cell size, cell density, and void fraction of the foam. However, the solutions can still be used to make qualitative predictions when various extrusion parameters are changed.

4.2 THERMODYNAMICS OF NUCLEATION PROCESS IN TWO COMPONENT SYSTEMS

Let us consider the mixing of two low molecular weight components A and B where the mixing process occurs with molecules of A and B occupying lattice sites as shown in Figure 4.1. Then, using the tools of statistical thermodynamics an approximate expression for the Gibbs free energy of mixing of two components A and B can be summarized as follows (Flory, 1953; Cha, 1994; Walton, 1987):

$$G_m = G_{AB} - (G_A + G_B) = N\left[zU(P)\xi(1-\xi) + kT\left\{\xi \ln\xi + (1-\xi)\ln(1-\xi)\right\}\right] \quad (4.1)$$

where,

N=Total number of molecules of A and B
z=Coordination number
U(P)=Energy of interaction between molecules of A and B
ξ=Molecule fraction of B in the mixture of A and B
k=Boltzman constant
T=Temperature
G_m=Gibbs free energy of mixing
G_A=Gibbs free energy of component A
G_B=Gibbs free energy of component B

G_{AB}=Gibbs free energy of the mixture of A and B

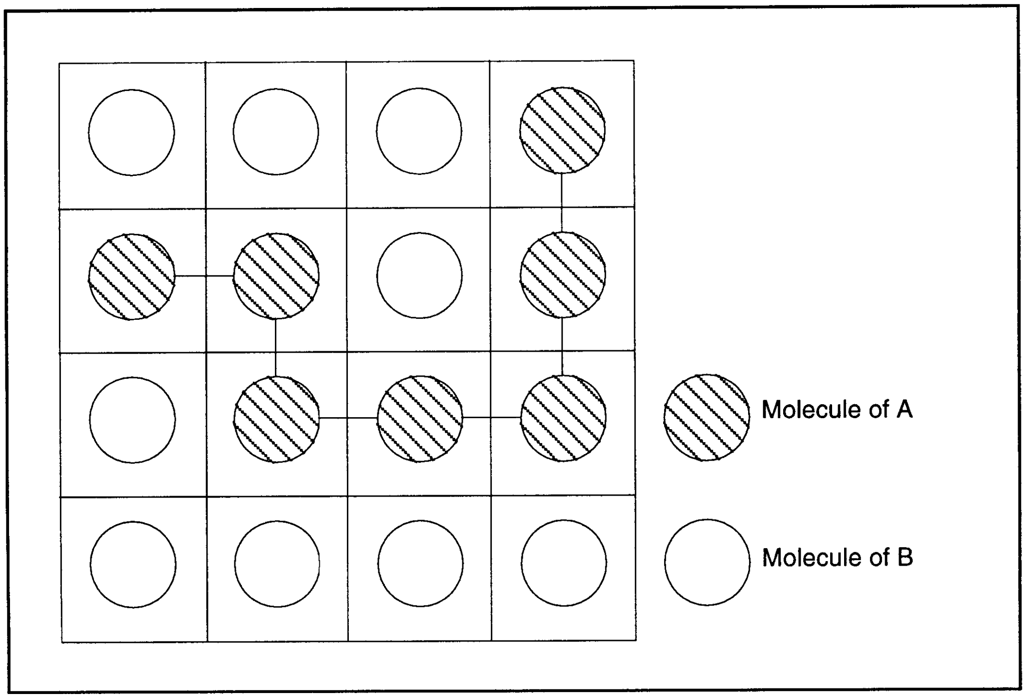

Figure 4.2 Lattice mixing model for components A and B.

The interaction energy function U(P) is derived later in this chapter in Section 4.10 and is expressed here as

$$U(P) = -\frac{kT \ln[K_s P \overline{M}_A/\overline{M}_B]}{z[\frac{1 - K_s P \overline{M}_A/\overline{M}_B}{1 + K_s P \overline{M}_A/\overline{M}_B}]} \qquad (4.2)$$

where K_s is Henry's constant for corresponding to the solution of A and B and $\overline{M}_A$ and $\overline{M}_B$ are the molecular weights of the components A and B respectively.

The graphical representation of Gibbs free energy of mixing is shown in Figure 4.2. Let us consider component A to be monomer groups of a polymer and component B to be gas. Equation (4.1) is valid for mixing of low molecular weight components involving occupation of lattice sites. We assume that each monomer group of a polymer occupies a lattice site. Each molecule of gas also occupies one lattice site. The saturated solution of gas in polymer will then be denoted by State 0 where at a particular condition of temperature and pressure the Gibbs free energy of mixing is minimum. The nucleation process starts when the pressure of the system is reduced instantaneously so that the new Gibbs free energy of mixing curve is reached. State 1 represents the new state that the system reaches. This obviously corresponds to a thermodynamic instability because the present state of the system is different from the new equilibrium state at the new pressure which corresponds to the lowest Gibbs free energy of mixing at the new pressure P_1. The gas concentration in the mixture exceeds the equilibrium gas concentration and so the gas phase starts to separate out of the system. The nucleation process is guided by the change in Gibbs free energy between State 2 and a neighboring state where some gas has separated out of the mixture (State 1).

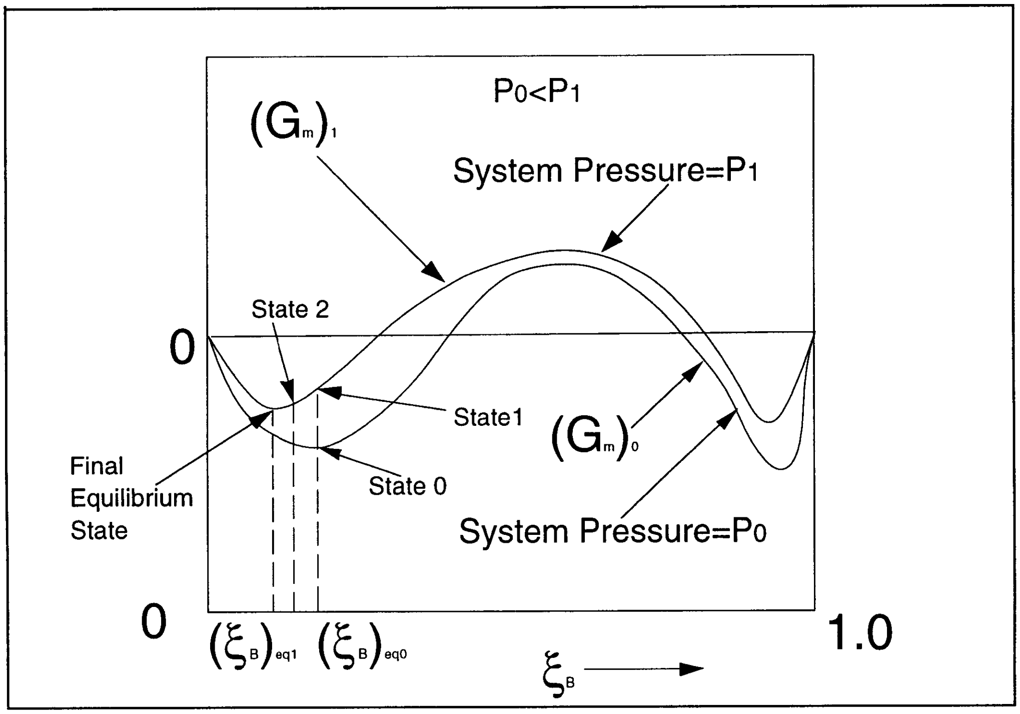

Figure 4.1 Gibbs Free Energy of mixing as a function of the molecule fraction of component B and pressure of the system.

The following expressions for Gibbs free energy of the mixture of A and B can be noted:

$$(G_{AB})_1 = (G_A)_1 + (G_B)_1 + (G_m)_1 \tag{4.3}$$

$$(G_{AB})_2 = (G_A)_2 + (G_B)_2 + (G_m)_2 \tag{4.4}$$

The total Gibbs free energy change between State 1 and State 2 is given by

$$\Delta G_v = (G_{AB})_2 - (G_{AB})_1 + (G_B)_3 \tag{4.5}$$

where $(G_B)_3$ is the Gibbs free energy of the separated gas phase.

Using (4.3) and (4.4) this total change in Gibbs free energy due to phase separation can be further expressed as

$$\Delta G_v = \left[(G_m)_2 - (G_m)_1\right] + \left[(G_A)_2 - (G_A)_1\right] + \left[(G_B)_2 - (G_B)_1\right] + (G_B)_3 \tag{4.6}$$

i.e.,

$$\Delta G_v = \Delta G_m + \Delta G_A + \Delta G_B \qquad (4.7)$$

The Gibbs free energy of mixing $(G_m)_1$ and $(G_m)_2$ are given by

$$(G_m)_1 = N_1\left[zU(P_1)\xi_1\left(1-\xi_1\right)+kT\xi_1\ln\xi_1+\left(1-\xi_1\right)\ln\left(1-\xi_1\right)\right] \qquad (4.8)$$

$$(G_m)_2 = N_2\left[zU(P_2)\xi_2\left(1-\xi_2\right)+kT\xi_2\ln\xi_2+\left(1-\xi_2\right)\ln(\left(1-\xi_2\right)\right] \qquad (4.9)$$

The change in the Gibbs free energy of the polymer is given by

$$\Delta G_A = 0 \qquad (4.10)$$

The Gibbs free energy of the gas at States 1 and 2, if it existed freely, could be expressed by considering it to be an ideal gas and recognizing the fact that for a pure substance the specific Gibbs free energy is the chemical potential $\mu(T,P)$ (Gyftopolous, 1991).

$$(G_B)_1 = (N_1\xi_1/A^*)\left[\mu(T_o,P_o)+C_p(T-T_o)+RT\ln(P_1/P_o)-C_pT\ln((T/T_o)\right] \qquad (4.11)$$

$$(G_B)_2 = (N_2\xi_2/A^*)\left[\mu(T_o,P_o)+C_p(T-T_o)+RT\ln(P_2/P_o)-C_pT\ln((T/T_o)\right] \qquad (4.12)$$

where T_o and P_o are some reference temperature and pressure and the specific heat C_p as well as the chemical potential $\mu(T_o,P_o)$ are expressed on a per mole basis. A^* is the Avagadro number.

If the separated gas is also assumed to be an ideal gas, then the Gibbs free energy can be expressed as follows:

$$(G_B)_3 = \left(\frac{N_1\xi_1-N_2\xi_2}{A^*}\right)\left[\mu(T_o,P_o)+C_p(T-T_o)+RT\ln(P_g/P_o)-C_pT\ln((T/T_o)\right] \qquad (4.13)$$

where P_g is the pressure of the separated gas phase.

Simplifying the above equations gives the following results:

$$\begin{aligned}\Delta G_v = {} & N_1\left[zU(P_1)\xi_1(1-\xi_1)+kT\xi_1\ln\xi_1+(1-\xi_1)\ln(1-\xi_1)\right] \\ & -N_2\left[zU(P_2)\xi_2(1-\xi_2)+kT\xi_2\ln\xi_2+(1-\xi_2)\ln((1-\xi_2)\right] \\ & +\left(\frac{RT}{A^*}\right)\left[N_1\xi_1\ln(P_g/P_1)-N_2\xi_2\ln(P_g/P_2)\right]\end{aligned} \qquad (4.14)$$

If we further observe that P_1 is equal to P_2 and note the relationship

$$N_1(1-\xi_1) = N_2(1-\xi_2) \qquad (4.15)$$

then Equation (4.14) can be written as (Walton, 1987):

$$\Delta G_v \approx (\xi_1 - \xi_2)\frac{d}{d\xi}\left[N_1 zU(P_1)\xi(1-\xi) + N_1 kT\{\xi \ln \xi + (1-\xi)\ln(1-\xi)\}\right]\Big|_{\xi=\xi_1} + \left(\frac{N_1\xi_1 - N_2\xi_2}{A^*}\right)RT\ln(P_g/P_1) \tag{4.16}$$

On further simplification the above expression reduces to

$$\Delta G_v = N_1(\xi_1 - \xi_2)\left[zU(1-2\xi_1) + kT\ln\left(\frac{\xi_1}{1-\xi_1}\right)\right] + \left(\frac{N_1\xi_1 - N_2\xi_2}{A^*}\right)RT\ln(P_g/P_1) \tag{4.17}$$

We further assume that $N_1(x_1 - x_2) \approx N_1x_1 - N_2x_2$ =Number of gas molecules that have separated out of the mixture. If the separated gas phase forms a cluster of radius r and the volume of a single molecule of gas is v_g, then

$$N_1(\xi_1 - \xi_2) \approx N_1\xi_1 - N_2\xi_2 = \frac{\frac{4}{3}\pi r^3}{v_g} \tag{4.18}$$

and

$$v_g = \frac{RT}{P_g A^*} \tag{4.19}$$

Setting ξ_1=ξ in order to generalize the results, the total Gibbs free energy change due to the formation of the nucleus is

$$\Delta G = \Delta G_v + \Delta G_s \tag{4.20}$$

i.e.,

$$\Delta G = \frac{4}{3}P_g A^* \frac{r^3}{v_g}\left[zU(P)(1-2\xi) + kT\ln\{\xi/(1-\xi)\} + \frac{RT}{A^*}\ln(P_g/P)\right] + 4\pi r^2\sigma \tag{4.21}$$

To find the size of the critical cluster we set

$$\frac{d}{dr}(\Delta G) = 0 \tag{4.22}$$

i.e.,

$$\frac{4\pi\, r_{crit}^2}{v_g}\left[zU(P)(1-2\xi) + kT\ln\{\xi/(1-\xi)\} + \frac{RT}{A^*}\ln(P_g/P)\right] + 8\pi\, r_{crit}\sigma = 0 \tag{4.23}$$

$$r_{crit} = \frac{2\sigma v_g}{zU(P)(1-2\xi) + kT\ln\left\{\xi/(1-\xi)\right\} + \frac{RT}{A*}\ln(P_g/P)}$$

$$= \frac{2\sigma RT}{P_g A*\left[zU(P)(1-2\xi) + kT\ln\left\{\xi/(1-\xi)\right\} + \frac{RT}{A*}\ln(P_g/P)\right]} \tag{4.24}$$

The corresponding change in Gibbs free energy is given by

$$\Delta G_{crit} = \frac{16}{3}\pi\sigma^3\left[\frac{RT}{P_g A*\left\{zU(1-2\xi) + kT\ln\left(\frac{\xi}{1-\xi}\right) + \frac{RT}{A*}\ln(P_g/P)\right\}}\right]^2 \tag{4.25}$$

The nucleation rate can then be expressed as

$$J = \Omega\exp\left(-\frac{\Delta G_{crit}}{kT}\right) = \Omega\exp\left[-\frac{16}{3kT}\pi\sigma^3\left[\frac{RT}{P_g A*\left\{zU(1-2\xi) + kT\ln\left(\frac{\xi}{1-\xi}\right)\right\} + RT\ln(P_g/P)}\right]^2\right]$$

$$= C_o f_o \exp\left[-\frac{16}{3kT}\pi\sigma^3\left[\frac{RT}{P_g A*\left\{zU(1-2\xi) + kT\ln\left(\frac{\xi}{1-\xi}\right)\right\} + RT\ln(P_g/P)}\right]^2\right] \tag{4.26}$$

where the pre-exponential factor Ω is given by the product of the concentration of available homogeneous sites C_o and the frequency factor of gas molecules joining the nucleus.

It should be noted that we still do not know the value of the pre-exponential factor Ω. However, the value of Ω lies in the range of 10^{36} nuclei/m^3-sec and 10^{39} nuclei/m^3-sec for most situations (Walton, 1987). For the case of nucleation of gas clusters in polymers the value of Ω needs to be determined. Section 4.10 discusses the value of Ω that was obtained after some preliminary numerical simulation. The pressure P_g of a critical gas cluster can be estimated from the pressure of the bulk solution. This derivation is discussed in Section 4.10.

4.3 NUCLEATION DURING THE EXTRUSION PROCESS

Equation (4.26) gives us the nucleation rate as a function of several different variables. In a batch process the nucleation rate can be calculated by knowing all these variables. The same holds true for an extrusion process except that some of the variables such as pressure vary with time as the flow undergoes pressure drop in the extrusion die. Thus, the nucleation rate becomes a function of time inside the die. Moreover, since U is itself a function of P, therefore time also has an indirect effect on the nucleation rate. The diffusion of gas to the nucleated clusters (which is discussed in the next section) leads to an overall change in the concentration of the solution (determined by ξ) and thus also has a significant effect on nucleation rate. Thus as the flow proceeds through the die and undergoes pressure drop, the variables P, U(P), and ξ change and determine the nucleation rate at any particular instant of time t.

4.4 IDENTIFICATION OF KEY EXTRUSION PARAMETERS FOR NUCLEATION

It is obvious from Equation (4.26) that the key extrusion parameters are the pressure drop through the die, the degree of saturation that exists at the inlet to the die, the function U(P) which is the energy of interaction between gas and polymer molecules at different pressures, the surface tension σ, and the temperature T. In addition to these factors there are a number of other factors which affect the nucleation process. These factors affect the nucleation process through gas diffusion that takes place for cell growth. Since nucleation and the cell growth occur simultaneously, the factors that affect one of these two processes directly also affect the other one indirectly.

4.5 CELL GROWTH

The cell growth process starts as soon as critical clusters are nucleated. It continues till all the gas in the bulk solution had diffused into the nucleated cells or the temperature of the polymer matrix becomes sufficiently low such that any displacement of the matrix/gas interface becomes impossible. In general the cell growth process is a combination of gas diffusion as well as inertia controlled growth (growth of the cells due to high pressure inside).

The guiding differential equations for the cell growth process in a Newtonian medium can be summarized below (Baldwin, 1995)

$$\rho\left[\frac{3}{2}\left(\frac{dR_{cell}}{dt}\right)^2+R_{cell}\frac{d^2R_{cell}}{dt^2}\right]=-4\frac{\mu}{R_{cell}}\frac{dR_{cell}}{dt}+\left(P_g-P_\infty-\frac{2\sigma}{R_{cell}}\right)\qquad(4.27)$$

$$\frac{\partial}{\partial t}\left(\frac{P_gR_{cell}^{\ 3}}{RT}\right)=3\rho_pDr^2\left.\frac{\partial c}{\partial r}\right|_{R_{cell}}\qquad(4.28)$$

$$\frac{\partial c}{\partial t}+\frac{R_{cell}{}^{2}\frac{dR_{cell}}{dt}}{r^{2}}\frac{\partial c}{\partial r}=\frac{1}{r^{2}}\frac{\partial}{\partial r}\left(r^{2}D\frac{\partial c}{\partial r}\right) \tag{4.29}$$

where,

D=Diffusion coefficient
c=Gas concentration in the bulk solution
R_{cell}=Radius of a cell
μ=Melt viscosity
σ=Melt surface tension
ρ_p=Polymer density
P_g=Gas pressure inside a cell.

The initial condition for the above equations is $c(r,0)=c_i$. The boundary conditions for the equation are

$$c(R_{cell},t)=K_s\,P \tag{4.30}$$

implying that the region next to the cell has equilibrium gas concentration.

and

$$\left(\frac{\partial c}{\partial t}\right)_{t,r\to\infty}=0 \tag{4.31}$$

The above equations need to be solved simultaneously along with the nucleation rate equation. For the cell growth process in microcellular foaming, since the bubble grows in a highly viscous polymer/gas solution medium, the inertia terms (the terms on the left hand side) in Equation (4.27) can be neglected.

4.6 CELL GROWTH DURING EXTRUSION

In the case of microcellular foam extrusion the cell growth process can be studied under a few extreme cases.

4.6.1 Case 1:Cell growth in a viscous polymer/gas bulk solution with surface tension effects

In the first case the we assume that the diffusion of gas into the nucleated cells occurs in the die during the flow of the nucleating solution along the length of the die. Gas diffusion will continue outside the die if there is enough gas dissolved in the polymer. We can make some simplifying assumptions and approximate the cell growth process as discussed subsequently.

In cases where the diffusion process is extremely fast the cell growth process is controlled by the diffusion of gas from the bulk solution to the nucleated cells. The diffusion of the gas from the bulk solution into the cells through the gas/bulk solution interface can be modeled as diffusion in a semi-infinite body with a time dependent boundary condition where the concentration of gas in the bulk solution changes with time. This changing boundary condition is a result of the diffusion of the gas molecules into the nucleated clusters whereby the concentration in the bulk solution decreases. The guiding differential equation for gas diffusion can be summarized as follows:

$$\frac{\partial c}{\partial t^*} = D\frac{\partial^2 c}{\partial x^2} \tag{4.32}$$

where D is the diffusion coefficient. The initial condition for the above equation is

$$c\left(t^* = 0, x\right) = c_i \tag{4.33}$$

The boundary conditions are

$$c\left(t^*, x = 0\right) = c_0 \tag{4.34}$$

and

$$c\left(t^*, x = \infty\right) = c_i \tag{4.35}$$

where t* is the time variable relative to the nucleation of a critical cluster and its subsequent growth, i.e., t* is equal to zero when a critical cluster is nucleated and then the diffusion of gas from the solution into the cell varies with t*.

The boundary condition c_i is set by the concentration of gas in the polymer at the time the cell is nucleated. The concentration c_i is thus a function of time where the time variable starts at the beginning of the process of nucleation in the overall solution. The concentration c_0 at the cell boundary is also a function of time and is given by the equilibrium gas concentration in the bulk solution at any instant of time t, i.e.,

$$c_0 = K_s\, P(t) \tag{4.36}$$

It can easily be seen that the time dependent boundary condition $c(t^*,x=0)=K_s\,P(t)$ implies that the standard solution of the diffusion equation cannot be applied here. However, the analogy between this diffusion problem and that of a semi-infinite body can easily be noticed. This is further illustrated in Figures 4.3 and 4.4. Figure 4.3 shows how the time variable is counted during the flow of the solution along the length of the nozzle. Figure 4.4 shows the similarity between the current diffusion problem and that of a semi-infinite body.

From the solution of the differential equation for the semi-infinite body we can approximate the flux at the interface of the cell and polymer/gas solution as

$$f(t, t^*) \approx \frac{c(t^*) - K_s\, P(t^*)}{\sqrt{\pi\left(t - t^*\right) / D}} \tag{4.37}$$

The concentration of gas c(t) in the polymer at any time t can be derived from mass balance in the overall solution. Let $R_{cell}(t,t^*)$ be the radius at time t of a cell nucleated at time t*.

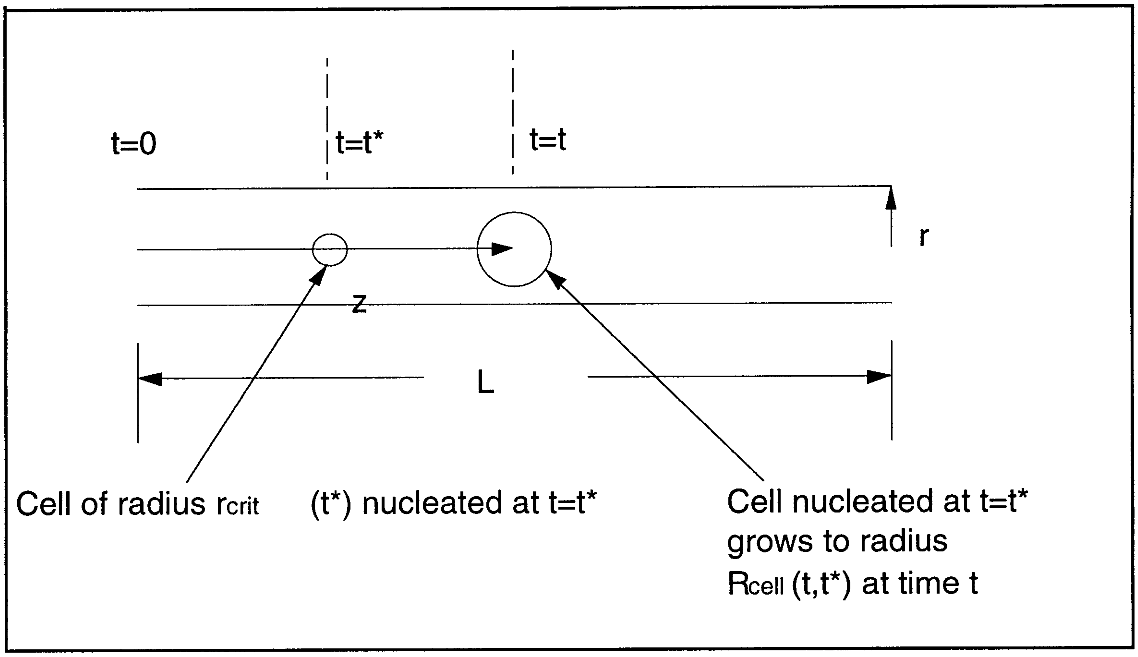

Figure 4.3 Time variables for nucleation and cell growth during extrusion.

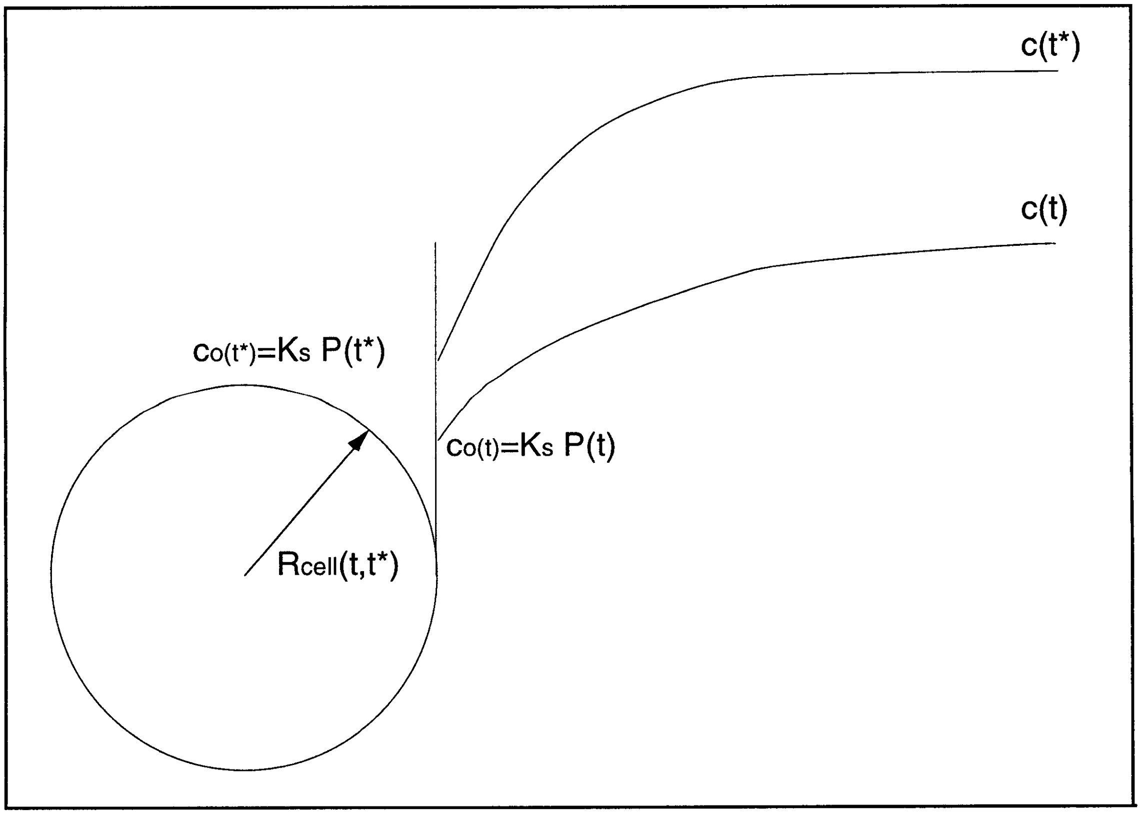

Figure 4.4 Concentration gradient as a function of time in bulk solution.

Thus, the mass flow rate of gas (in terms of moles/sec) into a cell at time t which was nucleated at time t* will be given by

$$\overset{o}{m} = 4\pi\left\{R_{cell}\left(t,t^*\right)\right\}^2 f\left(t,t^*\right) \tag{4.38}$$

If J(t) is the nucleation rate at time t, then the number of cells nucleated per unit volume in time dt is given by J(t)dt. Thus, the total mass flow rate of gas into nucleated cells at time t is given by

$$\overset{o}{M} = \int_{t^*=0}^{t^*=t} 4\pi\left\{R_{cell}\left(t,t^*\right)\right\}^2 f\left(t,t^*\right)J\left(t^*\right)dt^* \tag{4.39}$$

From mass balance of gas in the polymer/gas bulk solution we have

$$\frac{dc(t)}{dt} = -\overset{o}{M} = -\int_{t^*=0}^{t^*=t} 4\pi\left\{R_{cell}\left(t,t^*\right)\right\}^2 f\left(t,t^*\right)J\left(t^*\right)dt^* \tag{4.40}$$

The mass balance in a single cell leads to the following equation

$$\frac{d}{dt}\left[\{P_g(t,t^*))/RT\}(4/3)\pi\left\{R_{cell}\left(t,t^*\right)\right\}^3\right] = 4\pi\left\{R_{cell}\left(t,t^*\right)\right\}^2 f\left(t,t^*\right) \tag{4.41}$$

The pressure inside the cell $P_g(t,t^*)$ can be obtained from the solution of the Fluid Dynamics equations for cell growth:

$$P_g(t,t^*) = P_\infty(t) + 4\frac{\mu}{R_{cell}}\frac{dR_{cell}(t,t^*)}{dt} + \frac{2\sigma}{R_{cell}(t,t^*)} \tag{4.42}$$

It should be noted that Equation (4.42) is the same as Equation (4.27) with the inertia terms being neglected. The mole fraction of gas in the bulk solution can be estimated from the following relation

$$\xi(t) = \frac{c(t)}{c(t) + c_{pol}} \tag{4.43}$$

The initial condition for the equation (4.40) is $c(t=0)=c_{initial}=K_s\, P_{inlet}$, where K_s is Henry's constant. The initial condition for equation (4.41) is $R_{cell}(t=t^*,t^*)=r_{crit}.(t^*)$.

Solving equations (4.26), (4.37), (4.40), (4.41), (4.42) and (4.43) we can find the nucleation rate J(t), the concentration of gas in the bulk solution c(t) at any instant of time, and how the size of a cell $R_{cell}(t,t^*)$ nucleated at time t* varies with time t. It is obvious that analytical solutions for the above equations is not possible. Thus, we resort to numerical techniques.

Upon emergence from the die these cells will continue to expand as discussed later in Section 4.10.

4.6.2 Case 2:Cell growth by restricting cell wall displacement in the die

The second case assumes that the walls of the die restrain displacement of the polymer matrix which would be a necessary condition for cell growth. The cell growth inside the die is minimal and can be neglected. There is no decrease in pressure inside each cell. In fact, the pressure inside the cells increases due to diffusion of gas into the nucleated sites. However, on emergence from the die, the high pressure causes the cells to expand and as long as the polymer matrix is at a high enough temperature to accommodate displacement, the cells undergo expansion.

In this case the equations for the cell growth process can be summarized as follows:

$$R_{cell}(t,t^*) = R_{crit}(t^*) \tag{4.44}$$

$$P_g\left(t,t^*\right) = P_\infty(t) + \frac{2\sigma}{R_{crit}\left(t^*\right)} \tag{4.45}$$

$$\frac{dP_g\left(t,t^*\right)}{dt} = \frac{3RTf(t,t^*)}{R_{crit}(t^*)} \tag{4.46}$$

$$\frac{dc(t)}{dt} = -\overset{o}{M} = -\int_{t^*=0}^{t^*=t} 4\pi\left\{R_{crit}\left(t^*\right)\right\}^2 f\left(t,t^*\right)J\left(t^*\right)dt^* \qquad 4.47)$$

$$\xi(t) = \frac{c(t)}{c(t) + c_{pol}} \tag{4.48}$$

By solving equations (4.26), (4.44), (4.45), (4.46), (4.47) and (4.48) simultaneously we can obtain the pressure inside the cell $P_g(t,t^*)_g$ as a function of time. Once the flow emerges from the die, the cells will expand due to the high pressure inside the cells. This post die expansion of the cells is discussed in Section 4.8.

4.6.3 Case 3: Cell growth with constant pressure inside the cell

The third method of cell growth involves the pressure inside the nucleated cell remaining constant while the flow travels along the nozzle. Diffusion of gas takes place from the bulk solution to the cells and causes the cells to grow. However, the pressure inside the cells remains high and when the cells emerge from the die they grow due to the high pressure inside them. The cell growth process inside the die will then be governed by the following differential equations.

$$P_g\left(t,t^*\right) = P_g(t^*) = P_\infty(t^*) \tag{4.49}$$

$$4\frac{\mu}{R_{cell}(t,t^{*})}\frac{dR_{cell}(t,t^{*})}{dt}+\frac{2\sigma}{R_{cell}(t,t^{*})}=P_g\left(t,t^{*}\right)-P_{\infty}(t) \tag{4.50}$$

$$\frac{d}{dt}\left[\frac{P_g(t,t^{*})\,(4/3)\pi\,\{R_{cell}\left(t,t^{*}\right)\}^{3}}{RT}\right]=4\pi\,\{R_{cell}\left(t,t^{*}\right)\}^{2}f(t,t^{*}) \tag{4.51}$$

$$\frac{dc(t)}{dt}=-\overset{o}{M}=-\int_{t^{*}=0}^{t^{*}=t}4\pi\left\{R_{crit}\left(t^{*}\right)\right\}^{2}f\left(t,t^{*}\right)J\left(t^{*}\right)dt^{*} \tag{4.52}$$

$$\xi(t)=\frac{c(t)}{c(t)+c_{pol}} \tag{4.53}$$

Again, by solving Equations (4.26), (4.49), (4.50), (4.51), (4.52), (4.53) simultaneously we can obtain the function $R_{cell}(t,t^*)$ which is the size at time t of a cell nucleated at time t*. As stated before the cells will expand upon emergence from the die.

4.7 COMPETITION BETWEEN NUCLEATION AND CELL GROWTH IN THE DIE

As is evident both from an intuitive as well as an analytical perspective, there is competition between nucleation and cell growth for the gas that is still in solution in the polymer . Once the first set of critical clusters appear in the flow the gas starts diffusing to these clusters and as a result the concentration of the solution falls reducing the driving force for nucleation which is the degree of supersaturation of the solution at any instant of time. The critical clusters themselves require some critical number of gas molecules to form and as their number per unit volume of the bulk solution increases, the gas still in solution has to diffuse to a larger number of sites. This restricts the growth rate of any individual cell. Thus, the competition between nucleation and cell growth can be understood from a qualitative viewpoint as well as studied quantitatively by numerically solving the coupled nucleation and cell growth equations simultaneously.

4.8 IDENTIFICATION OF KEY PARAMETERS AFFECTING CELL GROWTH DURING EXTRUSION

It can be seen from the analysis of cell growth that the key factors affecting the process are the diffusion coefficient D, the bulk solution viscosity μ, the surface tension of the bulk solution σ, and the initial gas concentration in the polymer which in turn depends on the saturation pressure. It is assumed that this saturation pressure is the pressure at the die inlet. Thus, the cell growth process is influenced by the pressure drop through the die. Ofcourse, as mentioned in Section 4.4, the factors that affect nucleation also indirectly affect cell growth since nucleation and cell growth occur simultaneously and are coupled.

Thus the factors that affect the final microstructure of the foam have been identified. These are all the parameters that affect the nucleation rate and the cell growth process.

4.9 POST SHAPING COOLING AND CELL EXPANSION

If the pressure inside the gas cell is not allowed to relax inside the cell, then the cells undergo further expansion once the flow exits the die. If it is assumed that the cooling rate of the flow after emergence from the die is very slow and that the pressure inside the cells quickly reach atmospheric pressure with the cells being allowed to expand freely, then from the ideal gas law equation the final radius that the cells will reach will be given by

$$[R_{cell}(t^*)]_f = R_{crit}(t^*)\sqrt{\frac{(P_g)_{outlet}}{P_{atm}}} \qquad (4.54)$$

If however, the polymer matrix freezes or becomes highly viscous before the pressure inside the cells can relax to atmospheric pressure, then use of the ideal gas law equation again gives the final radius as

$$[R_{cell}(t^*)]_f = R_{crit}(t^*)\sqrt{\frac{(P_g)_{outlet}T_f}{P_{atm}T_{outlet}}} \qquad (4.55)$$

where T_f is the final temperature at which the cell growth process stops.

4.9.1 Heat Transfer Analysis

A more accurate and exact analysis of this post die cell growth process will involve the change in surface tension and viscosity of the melt with cooling. We can neglect temperature gradients across the cross section in the foam by assuming that the cross section is very thin and essentially approximate the problem as a moving fin problem. The corresponding heat transfer coefficient can be estimated from the forced convection relations taking into account the velocity of the foam upon exit from the die and its temperature. The equations governing this phenomenon of post die plastic cooling can be summarized as follows.

$$\frac{d^2\theta}{dx^2} - \frac{\rho C_p V}{K}\frac{d\theta}{dx} - \frac{hP}{KA}\theta = 0 \qquad (4.56)$$

where,

$\theta = T - T_{air}$
T=Temperature of the foam
T_{air}=Air temperature
V=Velocity of the foam
ρ=Density of foam
C_p=Specific heat of the foam
K=Thermal conductivity of the foam
h=Forced convection heat transfer coefficient
P=Perimeter of the extrudate
A=Cross sectional area of the foam

If we neglect conduction in the axial direction also, then the above equation reduces to

$$\frac{\rho C_p V}{K}\frac{d\theta}{dx} = -\frac{hP}{KA}\theta \qquad (4.57)$$

i.e.,

$$\frac{d\theta}{dx} = -\frac{\beta^2 \alpha}{V}\theta \qquad (4.58)$$

where,

$$\beta^2 = hP/KA \qquad (4.59)$$

$$\alpha = K/\rho C_p \qquad (4.60)$$

The solution to Equation (4.57) is

$$\theta = \theta_{exit} \exp(-\frac{\beta^2 \alpha}{V} x) \qquad (4.61)$$

i.e.,

$$\theta = \theta_{exit} \exp(-\beta^2 \alpha t) \qquad (4.62)$$

Thus the actual temperature of the foam as a function of time is given by

$$T = T_{air} + (T_{exit} - T_{air}) \exp(-\beta^2 \alpha t) \qquad (4.63)$$

4.9.2 Concurrent Cooling and Cell Growth

The surface tension and viscosity will vary as a function of time and are given by the following relations

$$\sigma(\tau) = \sigma_{exit} - \gamma\,[T(\tau) - T_{exit}] \qquad (4.64)$$

$$\mu(\tau) = \mu_{exit} \exp[-\varepsilon\{T(\tau) - T_{exit}\}] \qquad (4.65)$$

The equations governing this post die cell expansion can again be written down as

$$P_g\left(\tau, t^*\right) = P_{atm} + 4\frac{\mu(\tau)}{R_{cell}(\tau, t^*)}\frac{dR_{cell}(\tau, t^*)}{d\tau} + \frac{2\sigma(\tau)}{R_{cell}(\tau, t^*)} \qquad (4.66)$$

$$\frac{d}{d\tau}\left[\frac{P_g(\tau, t^*)\,(4/3)\pi\,\{R_{cell}\left(\tau, t^*\right)\}^3]}{RT(\tau)}\right] = 0 \qquad (4.67)$$

where,

$$\tau = t - t_{res} \tag{4.68}$$

The residence time of the flow in the die is denoted by t_{res}. The initial conditions for the post die cell growth process are

$$P_g(\tau = 0, t^*) = P_g(t = t_{res}, t^*) \tag{4.69}$$

$$R_{cell}(\tau = 0, t^*) = R_{cell}(t = t_{res}, t^*) \tag{4.70}$$

Solving the equations (4.63), (4.64), (4.65), (4.67) simultaneously along with the initial and boundary conditions (4.69), and (4.70) we can obtain the function $R_{cell}(\tau,t^*)$ and then evaluate the final cell size.

4.10 NUMERICAL SIMULATION OF NUCLEATION AND CELL GROWTH DURING EXTRUSION

The effects of some of the important parameters affecting cell microstructure can now be studied after numerical solutions of these equations have been obtained. However, before any meaningful simulation can be run, some important material properties and functions need to be evaluated. The important material properties that determine the dynamics of the process are the melt viscosity μ and the surface tension σ. Under typical conditions of temperature, pressure, and shear rate through the die that the flow experiences during foaming, the following approximate values of viscosity and surface tension are assumed (Tadmor and Gogos, 1979):

$$\mu = 600 \text{ Pa-s} \tag{4.71}$$

$$\sigma = 0.018 \text{ N/m} \tag{4.72}$$

The values of Henry's constant K_s for the two types of gas nitrogen and carbon dioxide are assumed to be the following:

$$(K_s)_{nitrogen} = 1.4 \times 10^{-3} \text{ g of } N_2/\text{g of polymer-MPa} \tag{4.73}$$

$$(K_s)_{carbon\ dioxide} = 3.99 \times 10^{-3} \text{ g of } CO_2/\text{g of polymer-MPa} \tag{4.74}$$

These estimates are based on nitrogen and carbon dioxide solubilities of 4% and 11% at 27.6 MPa in polymers (Park, 1993).

Evaluation of Interaction Energy U(P)

The function U(P) constitutes the enthalpy of mixing in Equation (4.2) and the solubility parameter approach (Hildebrand, 1962) can be used to estimate it. However, data for polymer and gas for different pressures is difficult to obtain and moreover, it would be illustrative to express U(P) in explicit functional form. This can be done by utilizing Equation (4.2) to derive the equilibrium gas concentration in a polymer.

From Equation (4.1) the Gibbs free energy of mixing per molecule is given by

$$g_m = G_m/N = zU(P)\xi(1-\xi) + kT\{\xi \ln\xi + (1-\xi)\ln(1-\xi)\} \tag{4.75}$$

To find the equilibrium concentration of gas molecules in the mixture of polymer and gas the derivative of Equation (4.75) with respect to ξ has to zero, i.e.,

$$\left.\frac{\partial g_m}{\partial \xi}\right|_{\xi=\xi^*} = \frac{\partial}{\partial \xi}\left[zU(P)\xi(1-\xi) + kT\{\xi \ln\xi + (1-\xi)\ln(1-\xi)\}\right]\Big|_{\xi=\xi^*} = 0 \qquad (4.76)$$

where ξ^* is the equilibrium gas concentration given by

$$\xi^* = \frac{N_{gas}}{N} = \frac{N_{gas}}{N_{gas} + N_{monomer}} \qquad (4.77)$$

Simplification of (4.76) leads to the following expression for U(P):

$$U(P) = \frac{kT \ln[\xi^*/(1-\xi^*)]}{z(2\xi^*-1)} \qquad (4.78)$$

The ratio of the number of grams of gas to the number of grams of polymer is given by Henry's law which has also been verified by Park (1993), Cha (1994), etc.

$$\psi^* = \frac{m_{gas}}{m_{polymer}} = K_s P \qquad (4.79)$$

The relation between ψ^* and ξ^* is as follows:

$$\xi^* = \frac{(\overline{M}_{mon}/\overline{M}_{gas})\psi^*}{1 + (\overline{M}_{mon}/\overline{M}_{gas})\psi^*} \qquad (4.80)$$

where,

$\overline{M}_{gas}$ = Molecular weight of gas

$\overline{M}_{mon}$ = Molecular weight of monomer group

From (4.78),(4.79) and (4.80) the explicit functional form for U(P) can be derived as

$$U(P) = -\frac{kT \ln[K_s P\, \overline{M}_{mon}/\overline{M}_{gas}]}{z\left[\dfrac{1 - K_s P\, \overline{M}_{mon}/\overline{M}_{gas}}{1 + K_s P\, \overline{M}_{mon}/\overline{M}_{gas}}\right]} \qquad (4.81)$$

Evaluation of Pressure P(t) in the Bulk Solution

The pressure P(t) can be evaluated from the fluid dynamics equations for flow through a die of any geometry. The assumption here is for steady state, isothermal flow of a Newtonian fluid through the die. For example, for a filament die of length L and inlet and outlet pressures of P_i and P_o respectively, the pressure is given by the following relation:

$$P(z) = P_1 - \frac{P_1 - P_0}{L} z \qquad (4.82)$$

where z is the coordinate along the length of the die and the direction of flow.

The average velocity for such Newtonian fluid flow is

$$v_{av} = \frac{r^2}{8\mu} \frac{P_1 - P_0}{L} \qquad (4.83)$$

where r is the die radius and μ is the fluid viscosity.

The relation between the distance z that the flow travels along the length of the nozzle and the average velocity v_{av} is

$$z = v_{av}\, t \qquad (4.84)$$

where time t is computed from the instant the flow enters the die.

From (4.82), (4.83), and (4.84) the function P(t) can be obtained as

$$P = P_1 - \left(\frac{P_i - P_0}{L} \right)^2 \frac{r^2}{8\mu} t \qquad (4.85)$$

Assumption for Gas Pressure P_g

The pressure P_g of a critical gas cluster also needs to be evaluated as an input into Equation (4.26). It is obvious that this pressure is going to be a function of the initial pressure P_0 and the pressure to which the system is taken, i.e., P_1. It should also depend on the gas and polymer material properties. In this analysis the pressure P_g is assumed to be equal to P_0.

Evaluation of Ω

The pre-exponential factor Ω in Equation (4.26) also needs to be estimated. For nucleation in binary component systems Ω usually lies between 10^{36} nuclei/m^3-sec and 10^{39} nuclei/m^3-sec (Walton, 1987). It was decided that values of Ω in this range would be tried and the final decision on what value to pick would be determined by comparison of theoretical results with preliminary experimental results.

After the material properties and functions have been estimated, a MATLAB code is written to numerically solve the nucleation and cell growth equations simultaneously for foaming of polypropylene (PP). It should be mentioned here that Case 2 and Case 3 models of cell growth did not produce physically realistic results. Also, the value of 10^{38} nuclei/m^3-sec for Ω was found to yield realistic results which predicted cell microstructure within an order-of-magnitude of actual preliminary experimental results. The code produced the results shown in Figures 4.5, 4.6, and 4.7 for filament extrusion through a 0.020"ϕ, 0.500" length die with nitrogen injection and a pressure drop of 20 MPa across the die.

Figure 4.5 shows the nucleation rate as a function of length along the die. Figure 4.6 shows how a cell nucleated at a distance of 50% along the length of the die grows as the flow proceeds along the die. Figure 4.7 shows how a cell nucleated at a distance of 60% along the length of the die grows after nucleation. The same simulation is run for a die of 0.020"φ, 0.500" length with the same pressure drop of 20 MPa across it. Figures 4.8, 4.9, and 4.10 show the results of the calculations. From these figures it can be seen how the nucleation rate and the radius of a nucleated cell vary as the flow proceeds along the die. A comparison of Figures 4.5 and 4.8 shows that the shorter die (implying smaller residence time and higher pressure drop rate) produces higher nucleation rate. Thus, the shorter die can be expected to produce higher cell density for the same pressure drop provided the residence time difference is not too large. A comparison of Figures 4.5 and 4.7 show that the radius of a nucleated cell grows to a slightly larger final size in the case of the shorter die. Figures 4.11, 4.12, and 4.13 show the same variables for a die of 0.020"f, 0.300" length with a pressure drop of 27.6 MPa across it.

Running the code with dies of different geometry and different pressure drop gave the predictions shown in Figures 4.14, 4.15, 4.16, and 4.17. In these figures the effect of die pressure drop and pressure drop rate on final cell radius and cell density are explored. The effects of using nitrogen and carbon dioxide are also studied in these figures. This theoretical model is used again in Chapter 8 to make predictions of foam microstructure and compare them to experimental results.

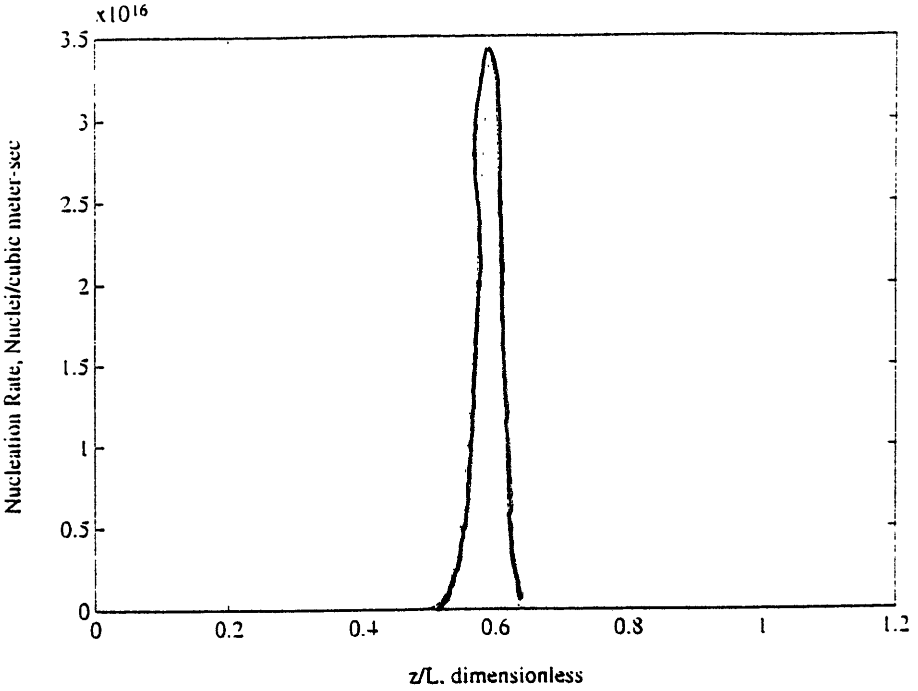

Figure 4.5 Nucleation rate in PP versus dimensionless length along the die for a 0.020"φ, 0.500" length die with ΔP=20MPa, T_{die}=400°F, and N_2 injection.

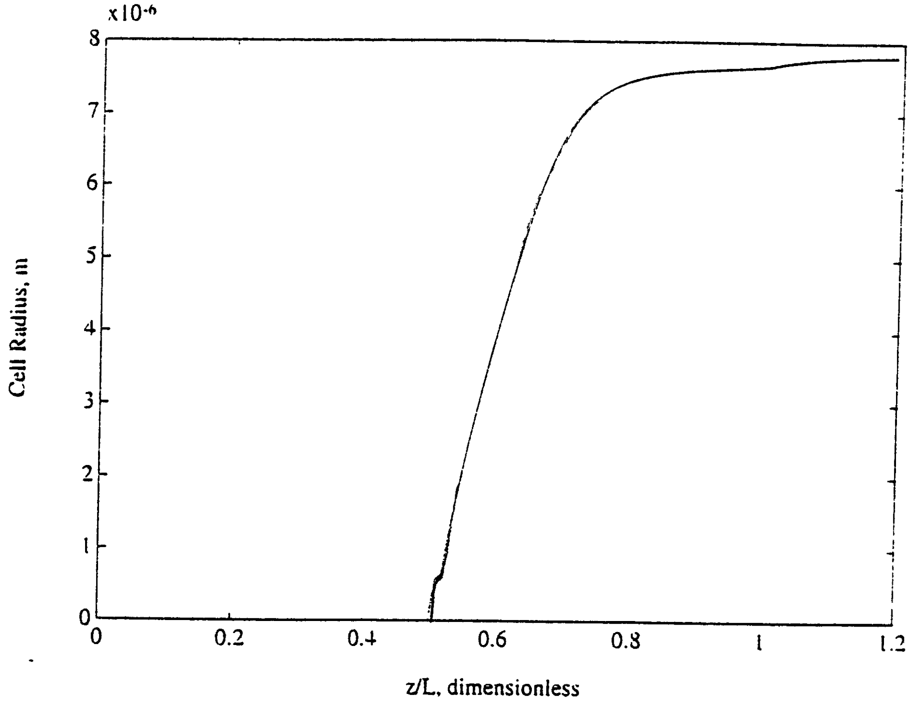

Figure 4.6 Cell radius in PP of a cell (nucleated at z/L=0.5) versus dimensionless length along the die for a 0.020"ϕ, 0.500" length die with ΔP=20MPa, T_{die}=400°F, and N_2 injection.

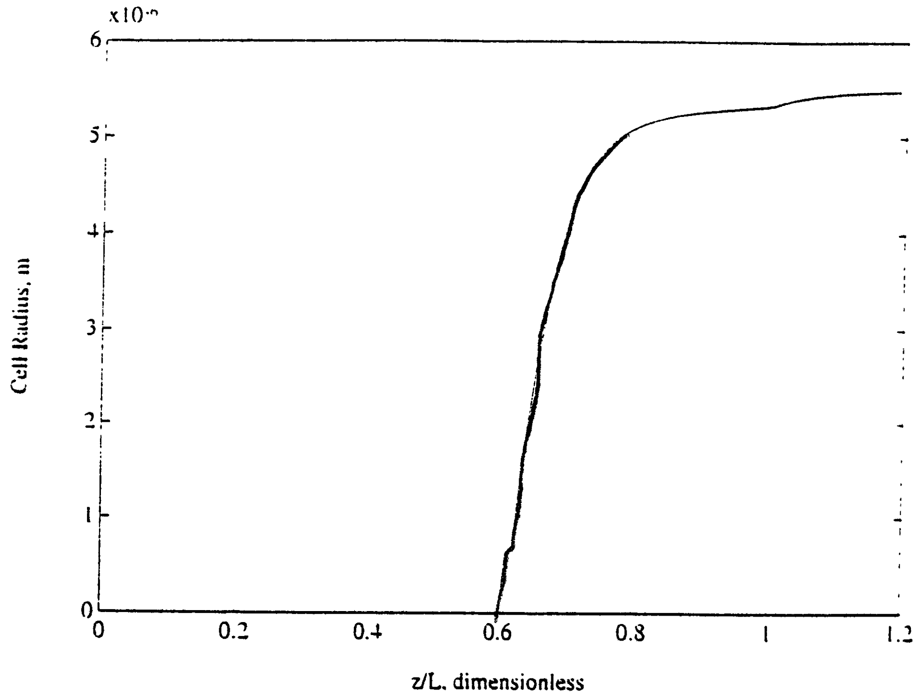

Figure 4.7 Cell radius in PP of a cell (nucleated at z/L=0.6) versus dimensionless length along the die for a 0.020"ϕ, 0.500" length die with ΔP=20MPa, T_{die}=400°F, and N_2 injection.

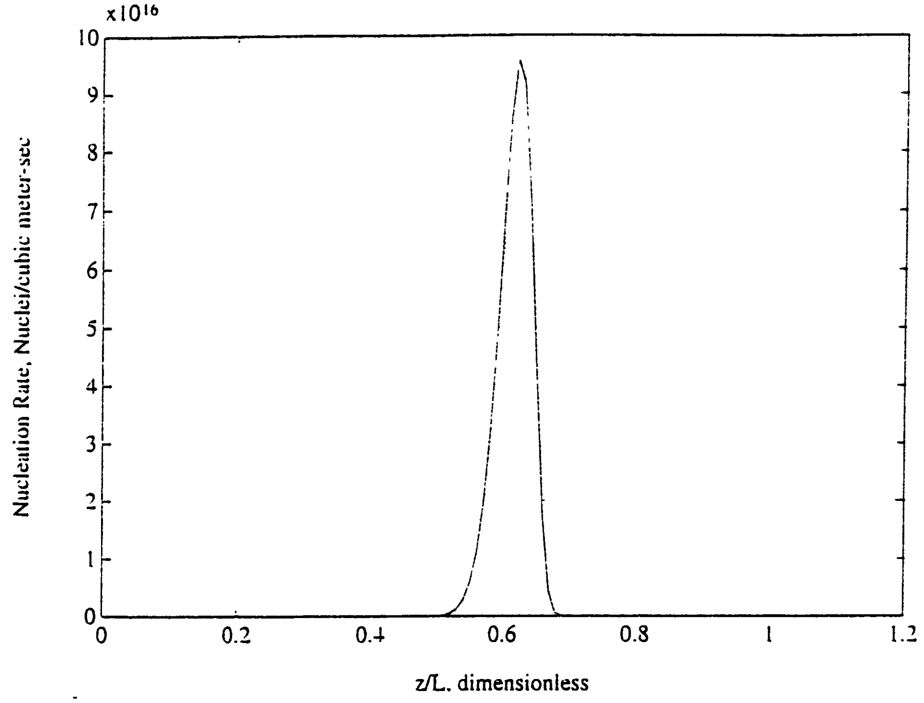

Figure 4.8 Nucleation rate in PP versus dimensionless length along the die for a 0.020"ϕ, 0.300" length die with ΔP=20MPa, T_{die}=400°F, and N_2 injection.

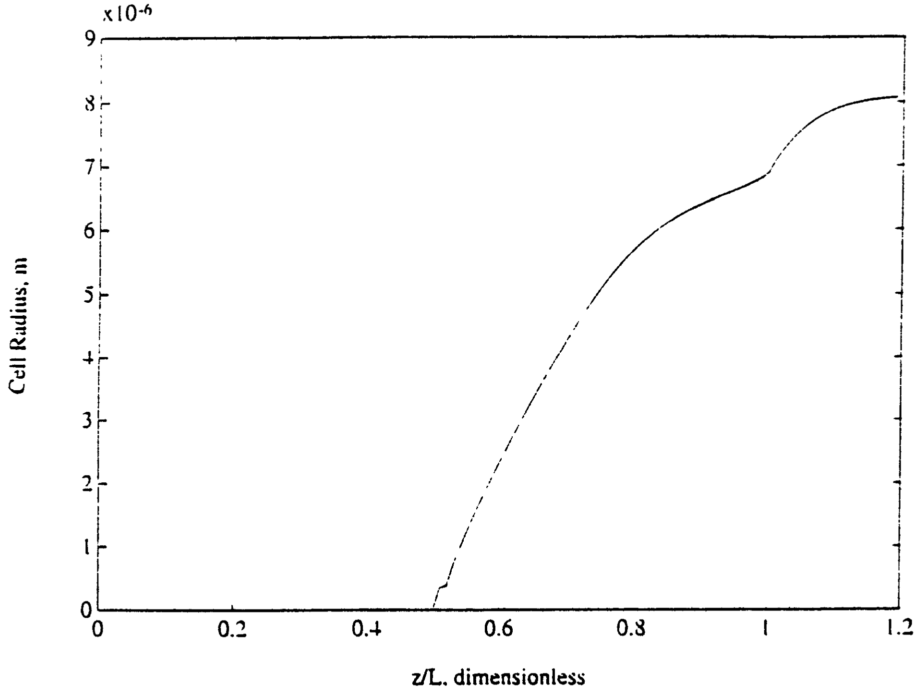

Figure 4.9 Cell radius in PP of a cell (nucleated at z/L=0.5) versus dimensionless length along the die for a 0.020"ϕ, 0.300" length die with ΔP=20MPa, T_{die}=400°F, and N_2 injection.

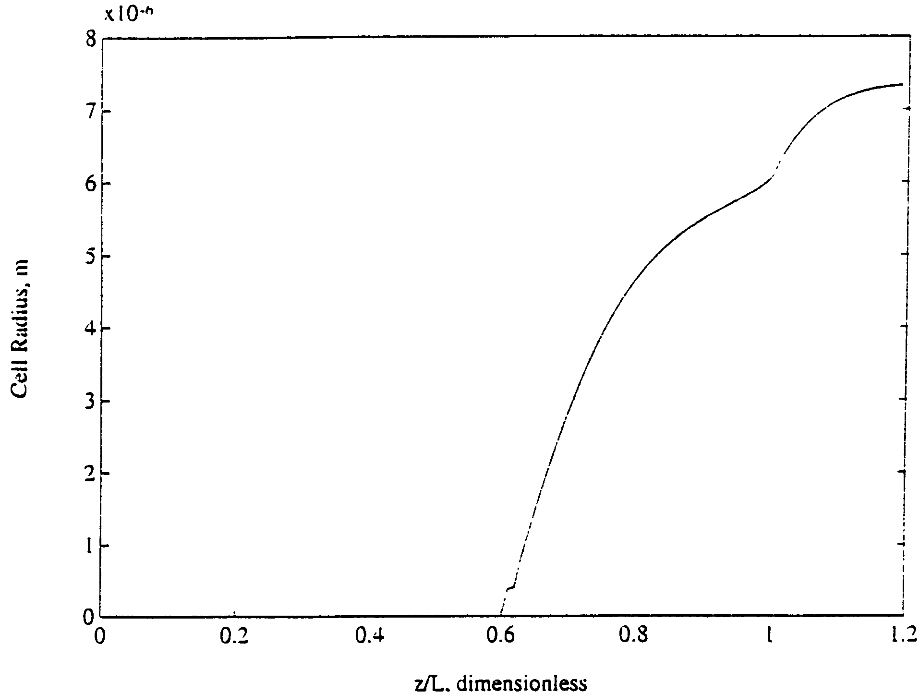

Figure 4.10 Cell radius in PP of a cell (nucleated at z/L=0.6) versus dimensionless length along the die for a 0.020"ϕ, 0.300" length die with ΔP=20MPa , T_{die}=400°F, and N_2 injection.

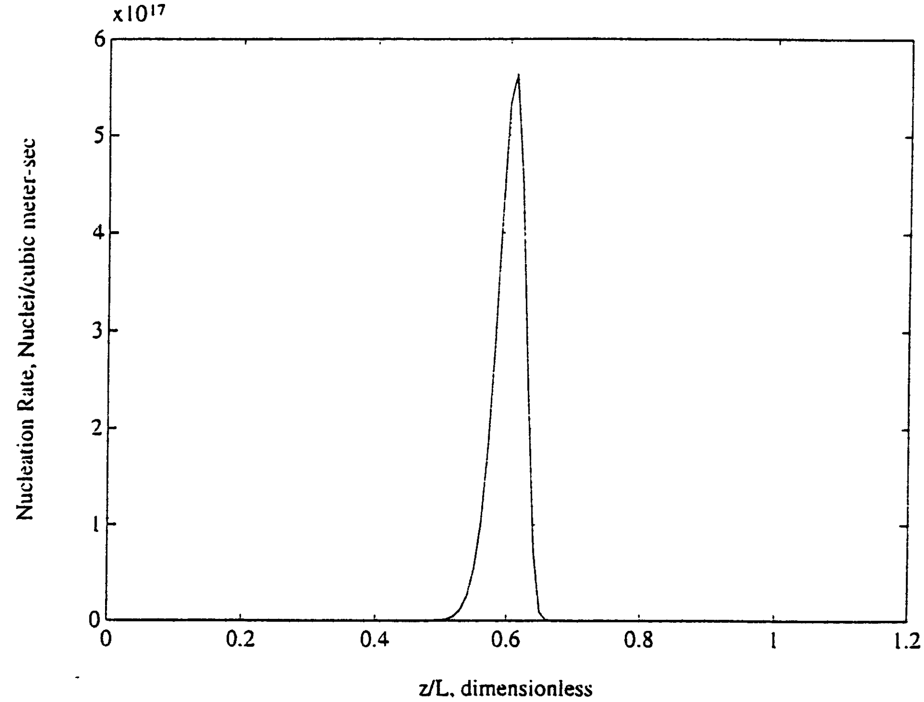

Figure 4.11 Nucleation rate in PP versus dimensionless length along the die for a 0.020"ϕ, 0.300" length die with $\Delta P=27.6$ MPa , $T_{die}=400°F$, and N_2 injection.

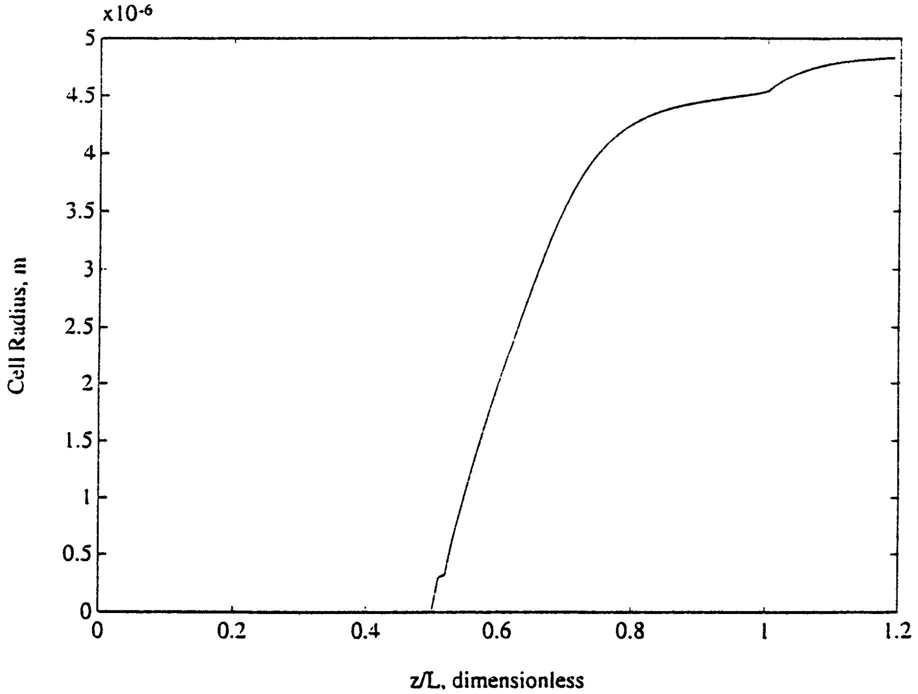

Figure 4.12 Cell radius in PP of a cell (nucleated at z/L=0.5) versus dimensionless length along the die for a 0.020"ϕ, 0.300" length die with $\Delta P=27.6$ MPa , $T_{die}=400°F$, and N_2 injection.

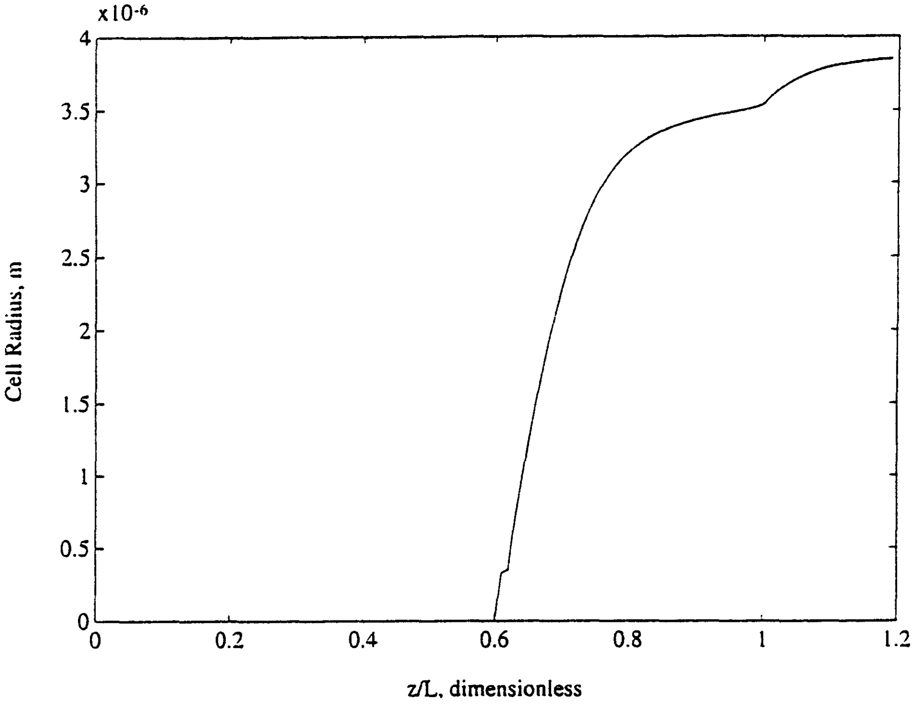

Figure 4.13 Cell radius in PP of a cell (nucleated at z/L=0.6) versus dimensionless length along the die for a 0.020"ϕ, 0.300" length die with $\Delta P=27.6$ MPa , $T_{die}=400°F$, and N_2 injection.

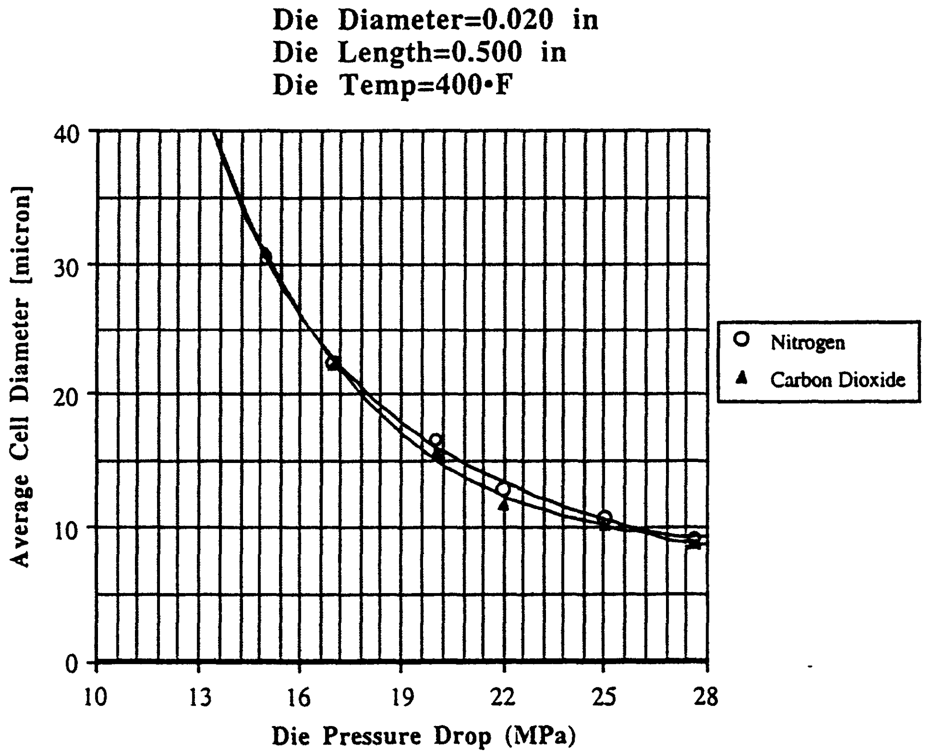

Figure 4.14 Cell diameter in PP versus pressure drop across die for the 0.020"ϕ, 0.500"L die with nitrogen injection and carbon dioxide injection.

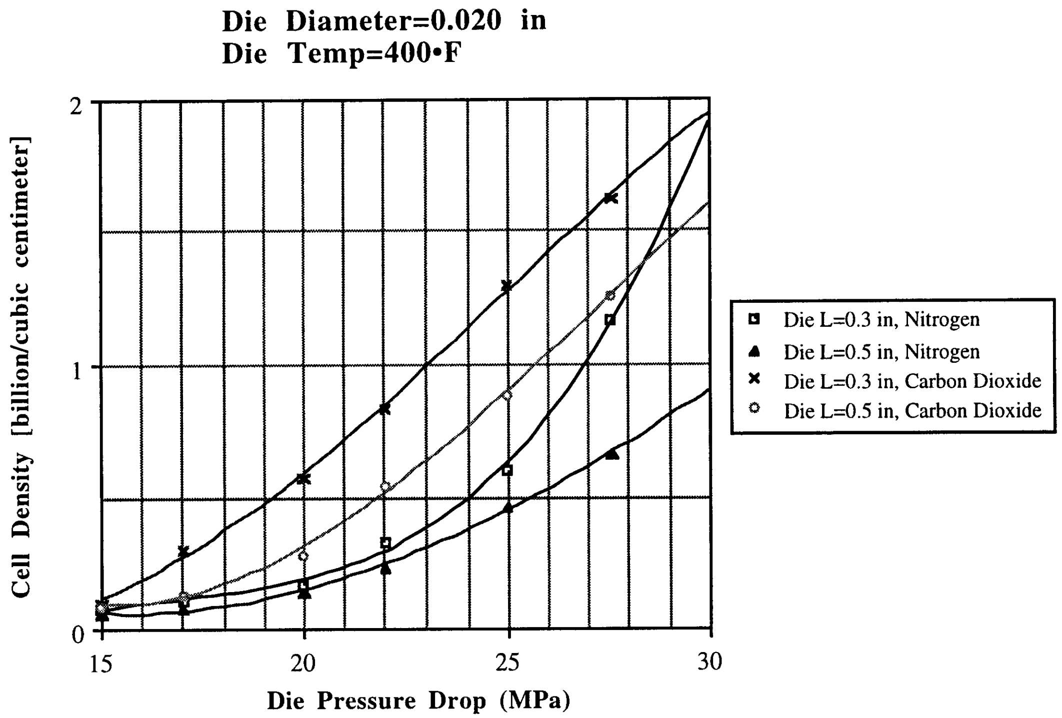

Figure 4.15 Cell density in PP versus pressure drop across die for the 0.020" ϕ die with nitrogen and carbon dioxide injection.

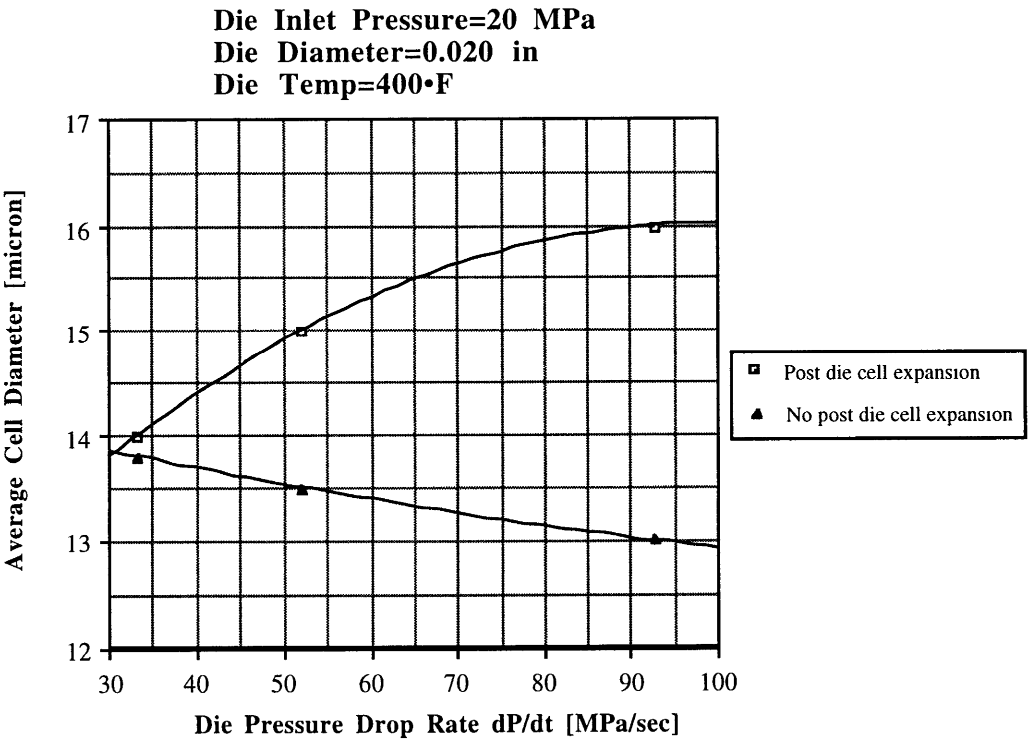

Figure 4.16 Cell diameter in PP versus pressure drop rate across die for the 0.020" ϕ die with nitrogen injection.

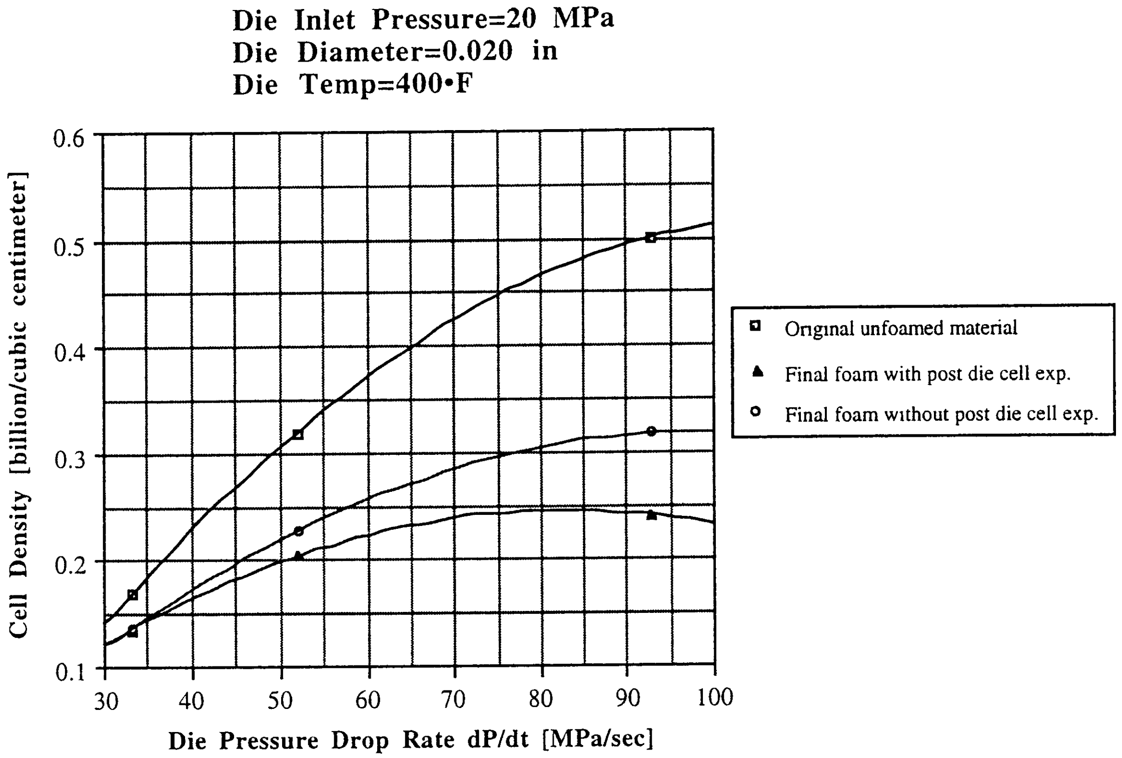

Figure 4.17 Cell density in PP versus pressure drop rate across die for the 0.020"ϕ die with nitrogen injection.

4.11 DISCUSSION OF RESULTS OBTAINED FROM NUMERICAL SIMULATION

The model of simultaneous cell nucleation and cell growth during extrusion shows that the cell size and void fraction increase with decrease in pressure drop across the die, provided all other extrusion parameters are held constant. The same increasing effect on cell size (although to a much smaller degree) and void fraction is observed as the length of the die is decreased with all other extrusion parameters being held constant. Overall, carbon dioxide produces foam of higher void fraction and slightly smaller cell size compared to nitrogen. Reduction in die temperature leads to slightly larger cell size and larger void fractions.

This theoretical model is used again in Chapter 8 to make predictions of foam microstructure and compare them to experimental results.

4.12 CRITICISM OF THE MODEL

The model of cell nucleation and growth developed in this Chapter has several weaknesses due to the many simplifying assumptions made in order to solve the equations. These issues are now summarized:

(1) The value of pressure in Equation (4.26) is assumed to be equal to the initial pressure of the solution. This is a big approximation. Better analysis and understanding of the

chemistry of solutions of polymer and gas can certainly be used to get more accurate and appropriate expressions of the pressure P_g.

(2) The expression (4.37) used to approximate the flux at the boundary of the cell and the bulk solution is only approximate.

(3) The model assumes that expansion of the cells is permitted by free displacement of the polymer matrix. This situation is not exactly true when the flow is inside the die.

(4) The function U(P) in (4.81) has been derived after many simplifying assumptions.

(5) The pre-exponential factor Ω is itself estimated to an order-of-magnitude in order to obtain realistic results when compared to preliminary experimental results.

(6) The computer code is not a finite element or finite difference code. It calculates the values of the variables at time t=0 and then projects those values forward in time to complete calculations for subsequent time steps. This method also makes the solution rather approximate and the solution accuracy depends on the size of the time step.

(7) The values for viscosity μ and surface tension σ were some average values for the estimated temperature, pressure, and shear rate conditions. The polymer is treated as a viscous fluid and not as a visco-elastic medium with shear rate dependent viscosity.

4.13 CONCLUSION

In this chapter a theoretical model for cell nucleation and growth has been developed which takes into account the thermodynamics of mixtures and solutions and the Gibbs free energy of separation of components. A computer code to numerically solve the cell nucleation and growth equations has been developed and has been used for preliminary investigation of extrusion parameters on cell size, cell density, and void fraction. Although the model has several weak issues, it still enables a qualitative understanding of the effect of such parameters and will be useful in their final choice.

CHAPTER 5

THEORY OF AXIOMATIC DESIGN

5.1 INTRODUCTION

Design is the process of clear definition of needs and devising ways and means to satisfy them. The needs of a customer or society at large is the basis for involvement in the design process. Design is also the process of linking disparate engineering fields. There are many methods that are used in engineering design such as design for manufacturing, design for assembly, Taguchi methods, concurrent engineering, and Axiomatic Design (Suh, 1990). Of all these methods, only the Axiomatic Design approach lays the foundation and groundwork for a systematic approach to explicitly stating design goals, conceptualizing design solutions, analyzing and evaluating various options, and finally choosing the most suitable option. This chapter discusses the basic ideas involved in the Axiomatic Design approach.

5.2 DOMAINS AND MAPPING

The needs of a customer or society at large is the basis for involvement in the design process. The needs of a customer are first defined and explicitly stated in the functional domain. These specific requirements are called functional requirements (FRs). In order to satisfy these functional requirements, a physical embodiment characterized in terms of design parameters (DPs) must be created. The DPs are then mapped onto the process domain in terms of process variables (PVs). The design process thus consists of stating FRs in the functional domain and then mapping these to DPs in the physical domain and then PVs in the process domain. Such a mapping process is shown in Figure 5.1. The objective of the design process is to decompose FRs and the corresponding DPs and PVs into a hierarchical structure in increasing level of detail as shown in Figure 5.2. The decomposition should be done through the method of zigzagging which implies that the decomposition in one domain is done with input from the previous level in other domains.

FRs are defined as the minimum set of independent requirements that completely characterize the functional needs of the design in the functional domain. By definition FRs are independent of each other. DPs are tangible physical entities that satisfy these requirements. PVs are process variables in a manufacturing process that can be adjusted to control the specific DPs.

5.3 DESIGN AXIOMS

There are two axioms governing good design. Axiom 1 establishes a guiding relationship between FRs and DPs while Axiom 2 addresses the level of complexity of the design. The statements of the two axioms are as follows:

Axiom 1 *The Independence Axiom*
Maintain the independence of FRs.
Alternate Statement 1: An optimal design always maintains the independence of FRs.

Alternate Statement 2: In an acceptable design, the DPs and the FRs are related in such a way that a specific DP can be adjusted to satisfy its corresponding FR without affecting other functional requirements.

Axiom 2 *The Information Axiom*
Minimize the information content of the design.
Alternate Statement: The best design is a functionally uncoupled design that has minimum information content.

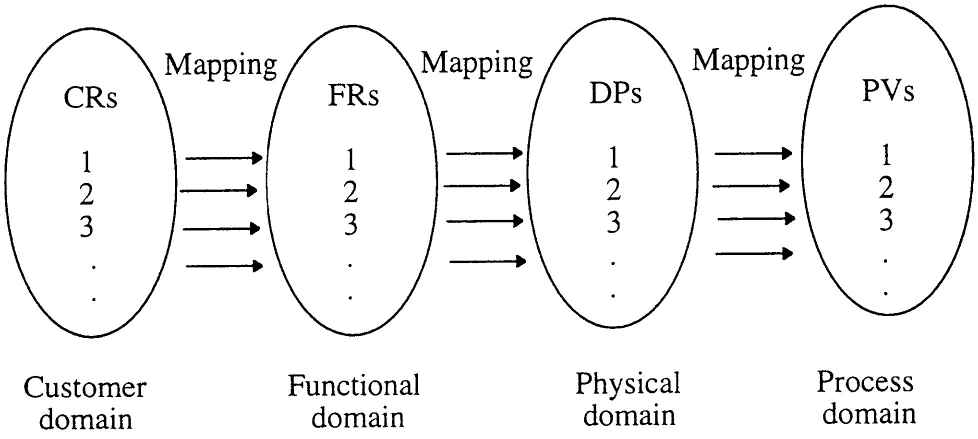

Figure 5.1 Mapping from one domain to another.

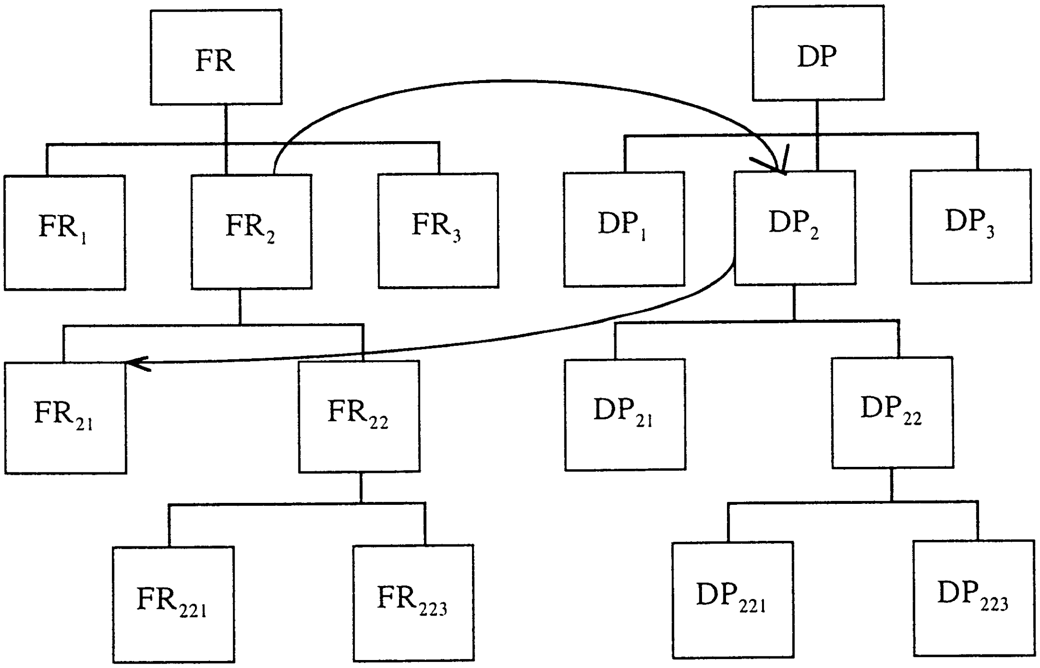

Figure 5.2 Domain hierarchy and decomposition through zigzagging.

5.4 COROLLARIES

There are several corollaries which can be derived from the two Axioms. These corollaries are useful in making specific decisions because they can be applied to actual situations more readily than the original axioms.

Corollary 1	(Decoupling of a Coupled Design) Decompose or separate parts or aspects of a solution if FRs are coupled or become interdependent in the designs proposed.
Corollary 2	(Minimization of FRs) Minimize the number of FRs and constraints.
Corollary 3	(Integration of Physical Parts) Integrate design features in a single physical part if FRs can be independently satisfied in the proposed solution.
Corollary 4	(Use of Standardization) Use standardized or interchangeable parts if the use of these parts is consistent with the FRs and constraints.
Corollary 5	(Use of Symmetry) Use symmetrical shapes and/or arrangements if they are consistent with the FRs and constraints.
Corollary 6	(Largest Tolerance) Specify the largest allowable tolerance in stating FRs.
Corollary 7	(Uncoupled Design with Less Information) Seek an uncoupled design that requires less information than coupled designs in satisfying a set of FRs.

5.5 MATHEMATICAL REPRESENTATION OF THE INDEPENDENCE AXIOM: DESIGN EQUATION

If a design has m independent FRs, then we can think of the set of FRs as a vector with m components. If there are n DPs which have been chosen to satisfy these FRs, then we can think of this set as a vector with n components. The relation between the two vectors can then be written in the following form:

$$\{FR\} = [A]\{DP\}$$

where [A] is the mxn design matrix relating the FRs to the DPs. We can write down each FR as follows

$$FR_i = \sum_j A_{ij} DP_j$$

Each of the elements of [A] can also be written as

$$A_{ij} = \frac{\partial FR_i}{\partial DP_j}$$

The form of the design matrix [A] is crucial to evaluating the satisfaction of the First Axiom. If all the non-diagonal elements of [A] are zero, then the design is uncoupled. Thus the requirements of an uncoupled design are

$$A_{kk} \neq 0$$
$$A_{ij} = 0,\ i \neq j$$

In this case each of the DPs can be adjusted to satisfy each of the corresponding FRs without affecting any other FR. The design equation looks as follows:

$$\begin{Bmatrix} FR_1 \\ FR_2 \\ \cdot \\ \cdot \\ FR_n \end{Bmatrix} = \begin{bmatrix} A_{11} & 0 & \cdot & \cdot & 0 \\ 0 & A_{22} & \cdot & \cdot & 0 \\ \cdot & \cdot & \cdot & \cdot & \cdot \\ \cdot & \cdot & \cdot & \cdot & \cdot \\ 0 & 0 & \cdot & \cdot & A_{nn} \end{bmatrix} \begin{Bmatrix} DP_1 \\ DP_2 \\ \cdot \\ \cdot \\ DP_n \end{Bmatrix} \tag{5.1}$$

In certain situations however, most of the off-diagonal elements are non-zero. In this case we have a coupled design because a change in any DP affects not only the corresponding FR, but some other components of the {FR} vector. This violates the First Axiom and is certainly not an acceptable design. In such a situation, a new set of DPs should be chosen so as to satisfy the First Axiom.

Some design equations can also assume the form shown below:

$$\begin{Bmatrix} FR_1 \\ FR_2 \\ \cdot \\ \cdot \\ FR_n \end{Bmatrix} = \begin{bmatrix} A_{11} & 0 & \cdot & \cdot & 0 \\ A_{21} & A_{22} & \cdot & \cdot & 0 \\ \cdot & \cdot & \cdot & \cdot & \cdot \\ \cdot & \cdot & \cdot & \cdot & \cdot \\ A_{n1} & A_{n2} & \cdot & \cdot & A_{nn} \end{bmatrix} \begin{Bmatrix} DP_1 \\ DP_2 \\ \cdot \\ \cdot \\ DP_n \end{Bmatrix} \tag{5.2}$$

In such a case we have a decoupled or quasi-coupled design. Here it should be noted that FR_2 depends on both DP_1 and DP_2. But once we have picked DP_1 to satisfy FR_1 we can still adjust DP_2 to achieve the desired FR_2. Then we can adjust DP_3 to get to FR_3 (which also depends on DP_1 and DP_2) and so on. In this way we can adjust the successive DPs to obtain the FRs keeping in mind the fact that there is a certain order in which we can proceed. The design matrix for a decoupled design is either upper-triangular or lower-triangular.

If the design equation assumes the form shown below, the design is coupled.

$$\begin{Bmatrix} FR_1 \\ FR_2 \\ \cdot \\ \cdot \\ FR_n \end{Bmatrix} = \begin{bmatrix} A_{11} & A_{12} & \cdot & \cdot & A_{1n} \\ A_{21} & A_{22} & \cdot & \cdot & A_{2n} \\ \cdot & \cdot & \cdot & \cdot & \cdot \\ \cdot & \cdot & \cdot & \cdot & \cdot \\ A_{n1} & A_{n2} & \cdot & \cdot & A_{nn} \end{bmatrix} \begin{Bmatrix} DP_1 \\ DP_2 \\ \cdot \\ \cdot \\ DP_n \end{Bmatrix} \tag{5.3}$$

In such a situation, the DPs cannot be adjusted to satisfy FRs independently. In such a case only a unique solution is available in the design space. Such a design violates the 1st Axiom and should be avoided.

5.6 THEOREMS

The characteristics of uncoupled, decoupled, and coupled designs lead to some more implications which can be summarized in the form of some theorems.

Theorem 1 (Coupling Due to Insufficient Number of DPs)
When the number of DPs is less than the number of FRs, either a coupled design results, or the FRs cannot be satisfied.

Theorem 2 (Decoupling of Coupled Design)
When a design is coupled due to the greater number of FRs than DPs it may be decoupled by the addition of new DPs so as to make the number of FRs and DPs equal to each other, if a subset of the design matrix constitutes a triangular matrix.

Theorem 3 (Redundant Design)
When there are more DPs than FRs, the design is either a redundant design or a coupled design.

Theorem 4 (Ideal Design)
In an ideal design, the number of DPs is equal to the number of FRs.

Theorem 5 (Need for New Design)
When a given set of FRs is changed by the addition of a new FR, or substitution of one of the FRs with a new one, or by selection of a completely different set of FRs, the design solution given by the original DPs cannot satisfy the new set of FRs. Consequently a new design solution must be sought.

Theorem 6 (Path Independence of Uncoupled Design)
The information content of an uncoupled design is independent of the sequence by which the DPs are changed to satisfy the given set of FRs.

Theorem 7 (Path Dependence of Coupled and Decoupled Designs)
The information contents of coupled and decoupled designs depend on the sequence by which the DPs are changed and on the specific paths of the changes of these DPs.

The detailed design of any manufacturing system should always be undertaken with a thorough analysis of the FRs, DPs, and PVs and their decomposition to a fine level of detail.

5.7 CONCLUSION

The general ideas associated with Axiomatic Design have been discussed in this chapter and the guidelines for good design have been outlined in the form of axioms, corollaries, and theorems. The actual application of these principles is carried out in Chapter 6 where they are utilized to design an actual wire coating extrusion process.

CHAPTER 6

APPLICATION OF AXIOMATIC DESIGN THEORY FOR THE EXTRUSION OF MICROCELLULAR WIRE COATING

6.1 INTRODUCTION

Chapter 5 discussed the general theory of Axiomatic Design and its application to design problems. The mapping process from the customer domain to the functional domain and then to the physical domain was discussed. For an actual manufacturing process a further step of mapping from the physical domain to the process variable domain is required. This chapter discusses the design of a microcellular wire extrusion system with the aid of Axiomatic Design principles.

6.2 CUSTOMER REQUIREMENTS

As in most sectors of the electronics industry, the wire and cable industry has seen an accelerating trend toward miniaturization. Each coaxial cable bundle is required to carry more and more of smaller size wires. The thickness and quality of the primary insulation on the wires is of critical importance. The needs of the manufacturer can be summarized as follows:*A wire of certain size and electrical characteristics.*

The wire size is important for assembling it into a bundle with many other wires while there are constraints on the final bundle size due to weight and flexibility issues.

6.3 MAPPING CUSTOMER REQUIREMENTS INTO FUNCTIONAL DOMAIN

As discussed in Chapter 5, the customer requirement need to be interpreted in actual engineering terms in the functional domain. The requirement stated in Section 6.3 can be met by the following functional requirement:

FR_1:Produce insulation of desired size and electrical performance

Since we have only one FR at this level we should be able to find a corresponding DP and a PV and satisfy the Independence Axiom at this level. The above FR can be decomposed into the following two FRs:

FR_{11}:Produce insulation of desired impedance.
FR_{12}:Produce insulation of desired thickness.

The insulation thickness will determine the final outside diameter (OD) of the wire

$$D = d + 2t \tag{6.1}$$

where, D=OD of coated wire
d=Diameter of conductor

t=Insulation thickness

The impedance affects the actual performance of the wire.

6.4 MAPPING INTO PHYSICAL DOMAIN

The actual physical parameters that correspond to the FRs defined in the functional domain are as follows:

DP_1:Microcellular wire coating extrusion process.

DP_{11}:Microstructure of final foamed insulation.
DP_{12}:Volume flow rate of foam relative to the wire.

The microstructure will determine how the insulation performs. The microstructure determines the final void fraction of the foam. The void fraction in turn will depend on the average cell size and the cell density. Using a linear relationship we can approximate the dielectric constant of the insulation as follows:

$$K \approx K_{pol}(1 - VF) + K_{gas}VF \tag{6.2}$$

The dielectric constant of the gas can be taken to be approximately equal to that of air. Thus,

$$K \approx K_{pol} - (K_{pol} - 1)VF \tag{6.3}$$

Thus, the effect of void fraction on final dielectric insulation is clearly understood.

The relation between the final void fraction and the cell size and cell density can also be summarized here as

$$VF = \frac{\frac{4}{3}\pi r_{av}^3 N}{1 + \frac{4}{3}\pi r_{av}^3 N} \tag{6.4}$$

where N_f is the cell density in the original material, i.e., the number of cells per cm^3 of the original unfoamed material and r_{av} is the average cell radius.

The volume flow rate of the foam will determine the final insulation thickness because of the following mass balance relationship:

$$\frac{\pi}{4}(D^2 - d^2)V = Q \tag{6.5}$$

where Q is the volume flow rate of the foam emerging from the extruder and V is the velocity of the wire being taken up. The final OD of the insulated wire is D while d represents the bare conductor diameter. Equation (6.5) assumes that the density of the foam remains constant after emerging from the extruder. The thickness of the insulation is given by Equation (6.1). Thus, it is evident why the volume flow rate of the foam relative to the wire speed is important.

6.5 MAPPING INTO PROCESS VARIABLE DOMAIN

The physical parameters that affect the FRs can now be mapped onto the process variable domain as follows:

PV_1:Wire coating extrusion variables.

PV_{11}:Foaming variables.
PV_{12}:Flow rate variables.

It should be noted that PV_1 and PV_2 have not been clearly identified yet. Although Chapter 4 discussed the foaming process in detail and outlined the effect of important extrusion parameters on the foaming process and the final microstructure, it is till not clear at this level what exact variables should be chosen for controlling the process. In order to identify the key variables that will result in a design that satisfies the Independence Axiom we need to decompose each of the domains (FR, DP, and PV) by means of zigzagging. Once the process variables have been clearly identified we can analyze the design by writing down design equations.

6.6 DECOMPOSITION OF DOMAINS

Figures 6.1, 6.2, and 6.3 show the decomposition of the FR, DP, and PV domains respectively.

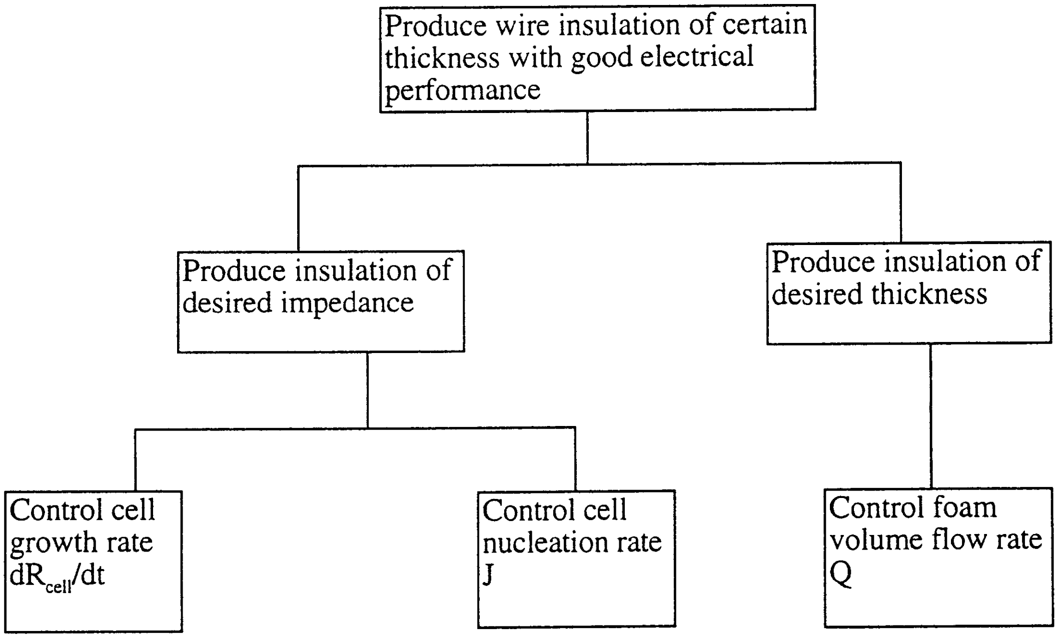

Figure 6.1 Decomposition of FRs.

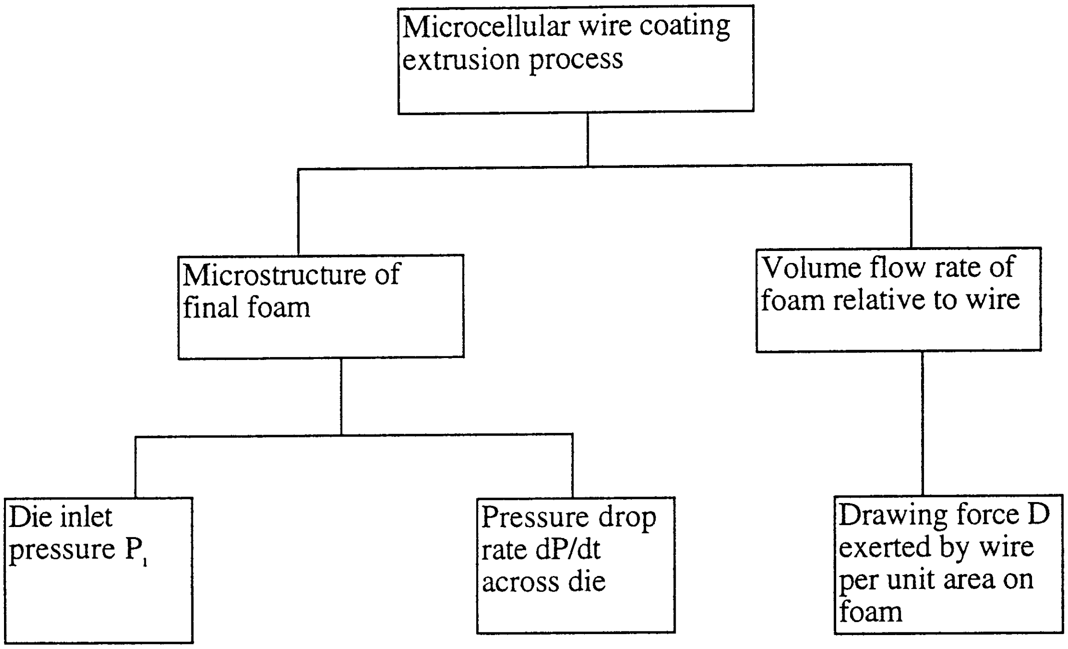

Figure 6.2 Decomposition of DPs

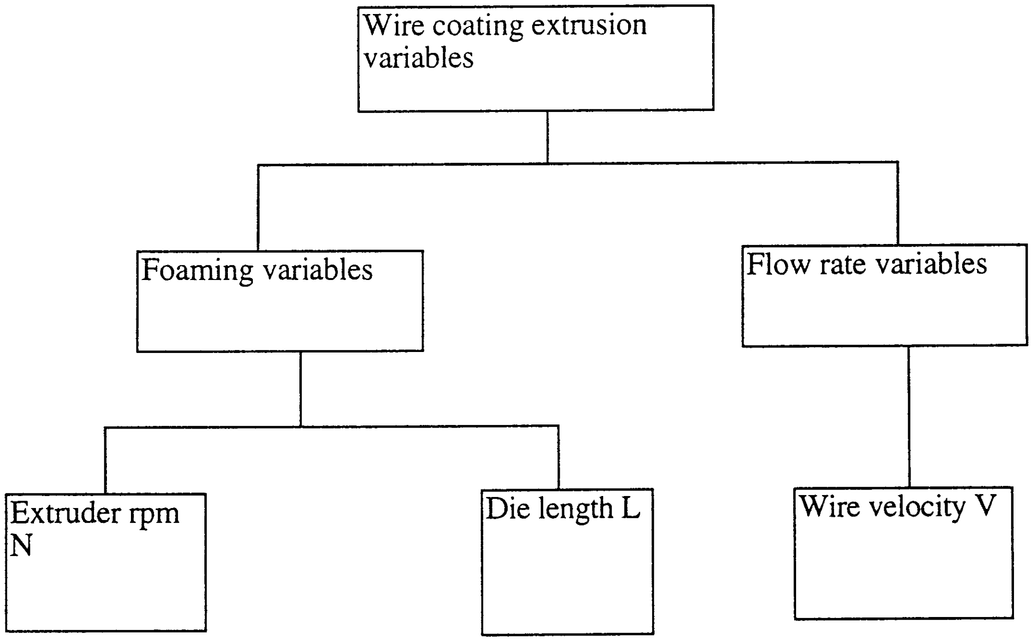

Figure 6.3 Decomposition of PVs.

Since the foaming process consists of cell nucleation and cell growth, it is the cell growth rate, cell nucleation rate, and how long these two mechanisms occur that will finally determine the final microstructure. Hence, FR_{111} and FR_{112} are identified as shown:

FR_{111}:Control cell growth rate dR_{cell}/dt
FR_{112}:Control cell nucleation rate J.

The higher the cell growth rate after a certain cell has been nucleated, the larger will be the final cell size provided all other parameters are held constant. The larger the cell nucleation rate, the higher will be the cell density if all other variables are kept fixed.

The cell growth rate is guided by the gas concentration in the bulk solution. The initial concentration is determined by gas dissolved, the upper limit of which depends on the die inlet pressure (Henry's Law). Furthermore, if the cells do not nucleate at the same time, there will be a large variation in cell size. The effect of die inlet pressure on the rate of cell growth can be seen from Figures 4.5 and 4.11. It is seen that when a cell is nucleated, the rate of cell growth depends strongly on the die inlet pressure. Thus, the die inlet pressure can be taken as the DP_{111} corresponding to FR_{111}.

The pressure drop rate dP/dt is the driving force for nucleation. The effect of changing dP/dt can be seen from Figures 4.5 and 4.8 where a shorter die length for same die inlet pressure (implying larger dP/dt) leads to a significant increase in nucleation rates. Thus, the pressure drop rate dP/dt through the die is taken as DP_{112}.

Thus, the DPs satisfying FR_{111} and FR_{112} are now summarized.

DP_{111}:Die inlet pressure P_i.
DP_{112}:Pressure drop rate dP/dt through the die.

As the discussion in Section (6.4) shows it is obvious why FR_{121} is to control the volume flow rate Q of the foam. In the type of wire coating dies known as pressure extrusion dies shown in Figure 6.4, the volume flow rate can be controlled by letting the wire exert a drawing force on the insulation inside the die. Thus the drawing force D (per unit area of contact) exerted by the wire on the flow is DP_{121} used to satisfy FR_{121}. As is evident from this discussion, D is numerically equal to the shear stress τ at the wire-foam interface inside the die.

The process variables chosen to control the DPs are summarized below.

PV_{111}:Extruder rpm N.
PV_{112}:Die length L.

PV_{121}:Wire velocity V.

6.7 MODELING OF THE PROCESS AND DESIGN EQUATIONS

Section 6.6 dealt with the decomposition of each of the domains with the aid of a qualitative understanding of the process. In order to write down the design equations, a more quantitative understanding of the process of foaming and coating onto wires is required. Chapter 4 dealt with a quantitative model of the foaming process. This section will thus use the results of Chapter 4 extensively to complete the modeling approach.

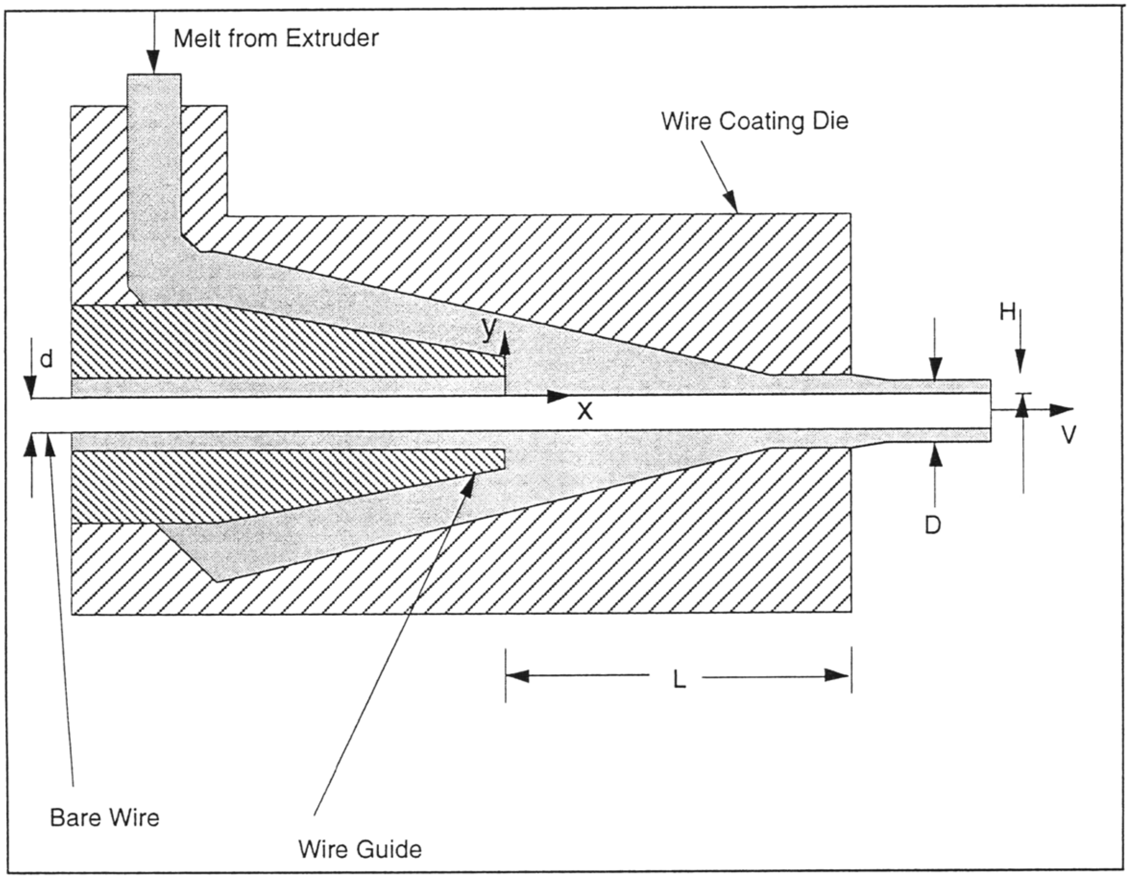

Figure 6.4 Pressure extrusion die.

6.7.1 Relation between FRs and DPs

As seen from Equation (4.37), the order of magnitude estimate of the mass flux of gas at the boundary of a cell when time t has elapsed since its nucleation can be taken to be

$$f \sim \frac{(\rho_{pol}/\overline{M}_{gas})K_s\,\Delta P}{\sqrt{\pi\,t/D}} \tag{6.6}$$

where ρ_{pol} is the density of the polymer in g/m^3, $\overline{M}_{gas}$ is the molecular weight of the gas, and K_s is Henry's constant. Assuming an ideal gas law, the order-of-magnitude estimate for the cell growth rate can then be approximated from Equations (4.38) and (4.41) as

$$\frac{dR_{cell}}{dt} \sim \left[\frac{3RT}{P_i + \frac{2\sigma}{r_{crit}}}\right]\frac{(\rho_{pol}/\overline{M}_{gas})K_s\,P_i}{\sqrt{\pi\,t/D}} \tag{6.7}$$

where r_{crit} is the critical radius of the cell. Thus, the dependence of cell growth rate on die pressure drop ΔP is easily illustrated by Equation (6.7).

The nucleation rate is given by Equation (4.26). From Equation (4.26) it is seen that the nucleation rate depends on the function U(P) given by Equation (4.81) and the molecule fraction of gas ξ in the polymer/gas solution. It is obvious that the degree of supersaturation in the polymer/gas solution depends on the pressure drop rate dP/dt which will determine the difference between the molecule fraction ξ and the equilibrium molecule fraction ξ_{eq}. The difference between ξ and ξ_{eq} is the driving force for nucleation. The faster the pressure drop rate the higher is the degree of supersaturation. In order to estimate how the nucleation rate is a function of dP/dt we review the equation for nucleation rate.

$$J = \Omega \exp\left[-\frac{16}{3kT}\pi\sigma^3 \left[\frac{RT}{P_g A * \left\{ zU(P)\,(1-2\xi) + kT\ln\left(\frac{\xi}{1-\xi}\right) + RT\ln(P_g/P) \right\}} \right]^2 \right] \tag{6.8}$$

The function U(P) is again reviewed here as

$$U(P) = -\frac{kT\ln[K_s P(t)\,\overline{M}_{mon}/\overline{M}_{gas}]}{z[\frac{1 - K_s P(t)\,\overline{M}_{mon}/\overline{M}_{gas}}{1 + K_s P(t)\,\overline{M}_{mon}/\overline{M}_{gas}}]} \tag{6.9}$$

In Equation (6.9) the pressure P is itself a linear function of time t given by

$$P(t)=P_i - (dP/dt)t \tag{6.10}$$

The order-of-magnitude of the pressure P_g is P_i while that for ξ is given by Equation (4.80) and can be estimated to an-order-of-magnitude as

$$\xi \sim \frac{(\overline{M}_{mon}/\overline{M}_{gas})K_s P_i}{1 + (\overline{M}_{mon}/\overline{M}_{gas})K_s P_i} \tag{6.11}$$

From Equations (6.8), (6.9), (6.10) and (6.11) the nucleation rate at any time t can be estimated to an order-of-magnitude as a function of die inlet pressure P_i and pressure drop rate dP/dt.

$$J \sim \Omega \exp\left[\alpha \left[\frac{\beta}{P_i \left\{ k\frac{1-\lambda P_i}{1+\lambda P_i}\frac{\ln[\lambda\{P_i - (dP/dt)t\}]}{\left[\frac{1-\lambda\{P_i - (dP/dt)t\}}{1+\lambda\{P_i - (dP/dt)t}\right]} + k\ln(\lambda) + \beta\ln[P_i/\{P_i - (dP/dt)t\}] \right\}} \right]^2 \right] \tag{6.12}$$

where,

$$\alpha = -\frac{16}{3kT}\pi\sigma^3 \tag{6.13}$$

$$\beta = R/A^* \tag{6.14}$$

$$\lambda = \left(\frac{\overline{M}_{mon}}{\overline{M}_{gas}}\right) K_s \tag{6.15}$$

Thus, it is clear that the pressure drop rate dP/dt as well as the die inlet pressure P_i affect the nucleation rate.

For the case of isothermal combined drag and pressure flow of an incompressible Newtonian fluid in a die whose annular thickness H is much smaller than the wire diameter d (Tadmor and Gogos, 1979), the volume flow rate of the flow during the wire coating process is expressed as

$$Q = Q_D + Q_P = \frac{VWH}{2} + \frac{WH^3\Delta P}{12\mu L} \tag{6.16}$$

where Q_D is the drag flow, Q_P is the flow due to pressure gradient, and W is the mean circumference of the annular space.

Since the pressure drop ΔP across the die is equal to the die inlet pressure P_i, therefore Equation (6.16) can be expressed as

$$Q = \frac{VWH}{2} + \frac{WH^3P_i}{12\mu L} \tag{6.17}$$

The velocity of the flow in the die as a function of y (Figure 6.4) is given by

$$v_z(y) = v_D + v_P = V\left(1 - \frac{y}{H}\right) + \frac{H^2\Delta P}{2\mu L}\left(\frac{y}{H}\right)\left[1 - \frac{y}{H}\right] = V\left(1 - \frac{y}{H}\right) + \frac{H^2P_i}{2\mu L}\left(\frac{y}{H}\right)\left[1 - \frac{y}{H}\right] \tag{6.18}$$

The drawing force per unit area exerted by the wire is given by

$$D = \mu \left.\frac{\partial v_D}{\partial y}\right|_{y=0} = \mu\frac{V}{H} \tag{6.19}$$

Thus, the flow rate can be expressed in terms of the drawing force as follows:

$$Q = \frac{DWH^2}{2\mu} + \frac{WH^3P_i}{12\mu L} \tag{6.20}$$

Thus, it is clear that the flow rate Q is a strong function of D and the die inlet pressure P_i.

We can now write down the design equation relating the FRs to the DPs:

$$\begin{bmatrix} \text{Control } dR_{cell}/dt \\ \text{Control } J \\ \text{Control } Q \end{bmatrix} = \begin{bmatrix} \phi & O & O \\ \gamma & \eta & O \\ \zeta & O & \varphi \end{bmatrix} \begin{bmatrix} P_i \\ dP/dt \\ D \end{bmatrix} \tag{6.21}$$

In Equation (6.21) the elements of the matrix are given by the functions as follows:

$$\phi = \frac{\partial (dR_{cell}/dt)}{\partial P_i} = \frac{6RT\rho_{pol}H\sigma}{\overline{M}_{gas}\, r_{crit} \left(P_i + \frac{2\sigma}{r_{crit}} \right)^2} \tag{6.22}$$

$$\gamma \sim \frac{\partial J}{\partial P_i} \tag{6.23}$$

$$\eta \sim \frac{\partial J}{\partial (dP/dt)} \tag{6.24}$$

$$\zeta = \frac{\partial Q}{\partial P_i} = \frac{WH^3}{12\mu L} \tag{6.25}$$

$$\varphi = \frac{\partial Q}{\partial D} = \frac{WH^2}{2\mu} \tag{6.26}$$

In Equations (6.23) and (6.24) the function J is given by Equation (6.12).

Thus, we see that we have a decoupled design when looking at the relationship between FRs and DPs. Whether the entire process is decoupled or not will become clear once the design equation relating DPs to PVs is written down.

6.7.2 Relation between DPs and PVs

The next step of the modeling process is the establishment of relationships between DPs and PVs. The die inlet pressure P_i, the pressure drop rate dP/dt, the residence time t_{res} and the flow rate Q need to be expressed in terms of the process variables H, N, L, and V.

Assuming the flow of an isothermal, incompressible Newtonian fluid in the metering section of the extruder screw shown in Figure 6.5, the flow rate can be expressed as (Tadmor and Gogos, 1979)

$$Q = \frac{\pi N D_b \cos\theta \, W^* H^*}{120} F_D - \frac{W^* H^{*3} \sin\theta}{12\mu} \frac{\Delta P}{L_s} F_P \qquad (6.27)$$

where L_s is the axial length of the screw and the rest of the variables are explained in Figure 6.5.

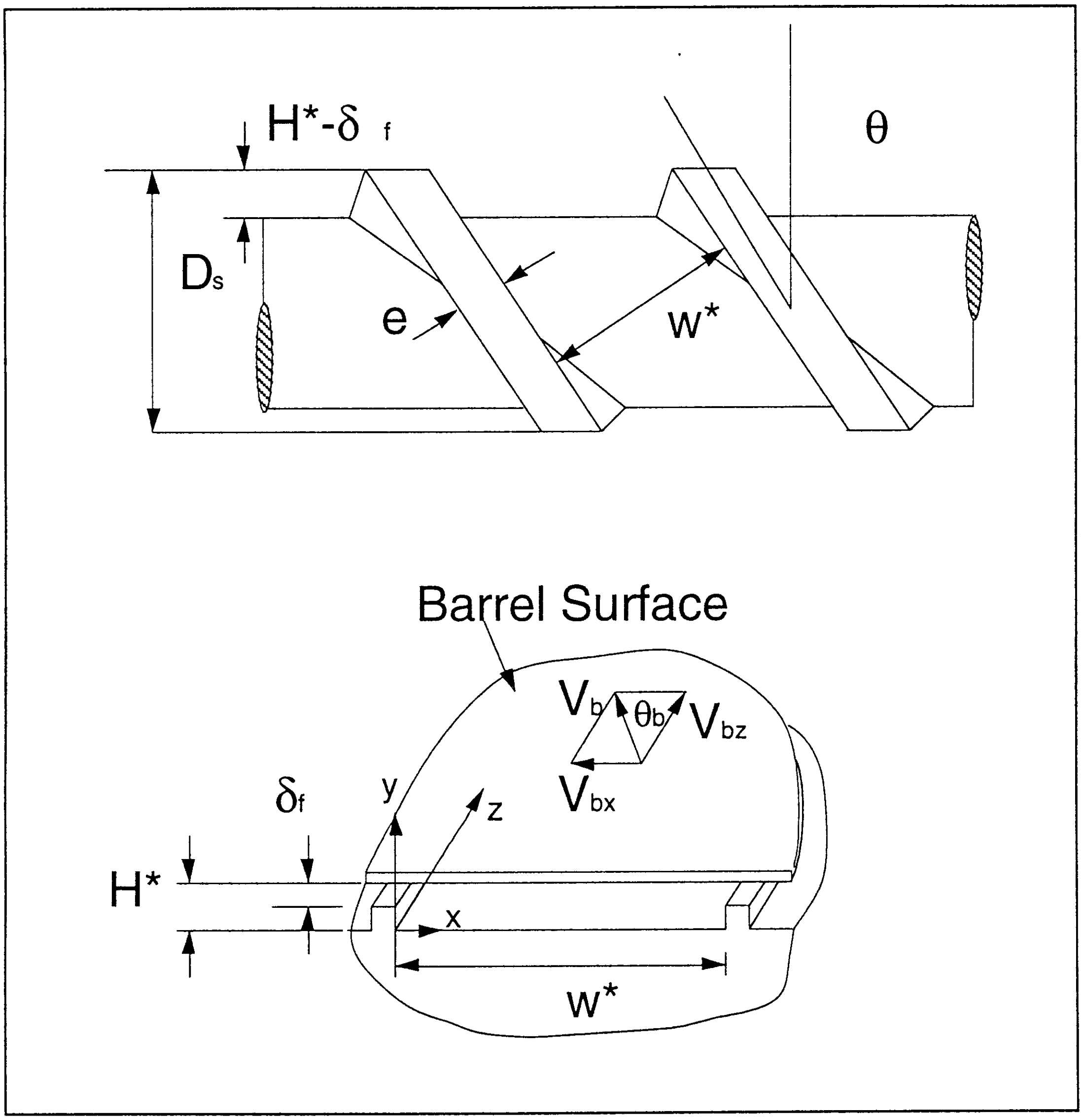

Figure 6.5 Screw geometry specifications and mechanism of flow in screw channel.

The drag and flow "shape factors" F_D and F_P are given respectively as

$$F_D = \frac{16W^*}{\pi^3 H^*} \sum_{i=1,3,5}^{\infty} \frac{1}{i^3} \tanh\left(\frac{i\pi H^*}{2W^*}\right) \qquad (6.28)$$

$$F_P = \frac{192H^*}{\pi^5 W^*} \sum_{i=1,3,5}^{\infty} \frac{1}{i^5} \tanh\left(\frac{i\pi W^*}{2H^*}\right) \qquad (6.29)$$

The shape factors represent the reducing effect of the flights of the screw on the flow rate and assume values that are smaller than 1. For reasons of simplifying the analysis, we assume for the time being that F_D and F_P are both approximately equal to 1. We also note that the pressure rise along the screw for a single screw extrusion process is equal to the die inlet pressure P_i. Although a tandem extrusion is finally developed for the wire coating process in this research, we assume that the pressure rise in the primary extruder is small and that the rise in pressure in the second extruder is equal to P_i. Thus, Equation (6.27) can be expressed as

$$Q = \frac{\pi N D_b \cos\theta \; W^* H^*}{120} - \frac{W^* H^{*3} \sin\theta}{12\mu} \frac{P_i}{L_s} \qquad (6.30)$$

From Equations (6.17) and (6.30) it is possible to derive an expression for pressure in terms of the process variables H, N, L, and V.

$$P_i = 12\mu \frac{\left[\dfrac{\pi N D_b W^* H^* \cos\theta}{120} - \dfrac{VWH}{2}\right]}{\left[\dfrac{WH^3}{L} + \dfrac{W^* H^{*3} \sin\theta}{L_s}\right]} \qquad (6.31)$$

It is clear from Equation (6.31) that the extruder rpm N, the die length L as well as the wire velocity V all determine P_i. In order to write down the design equation we need to determine the relative effects of changes in P_i that will be produced when each of the PVs is changed. This is discussed in later in this Section.

The pressure drop rate dP/dt is evaluated as follows:

$$\frac{dP}{dt} = \frac{P_i}{t_{res}} = \frac{P_i v_{av}}{L} = \frac{P_i Q}{LWH} = \frac{P_i}{LWH}\left[\frac{VWH}{2} + \frac{WH^3 P_i}{12\mu L}\right] \qquad (6.32)$$

where Equation (6.17) has been used for Q. Again, it is clear that since P_i is a function of four PVs, therefore dP/dt will be a function of all PVs also.

The die residence time t_{res} is given by

$$t_{res} = \frac{L}{v_{av}} = \frac{LWH}{Q} = \frac{LWH}{\left[\dfrac{VWH}{2} + \dfrac{WH^3 P_i}{12\mu L}\right]} \qquad (6.33)$$

The drawing force per unit area exerted by the wire on the flow is given by Equation (6.19) and is recounted here for convenience.

$$D = \mu \frac{V}{H} \tag{6.34}$$

From Equation (6.31) we get

$$\frac{\partial P_i}{\partial N} = 12\mu \frac{\left[\frac{\pi D_b W^* H^* \cos\theta}{120}\right]}{\left[\frac{WH^3}{L} + \frac{W^* H^{*3} \sin\theta}{L_s}\right]} \tag{6.35}$$

$$\frac{\partial P_i}{\partial L} = -12\mu\, WH^3 \frac{\left[\frac{\pi N D_b W^* H^* \cos\theta}{120} - \frac{VWH}{2}\right]}{\left[\frac{WH^3}{L} + \frac{W^* H^{*3} \sin\theta}{L_s}\right]^2} \tag{6.36}$$

$$\frac{\partial P_i}{\partial V} = -12\mu \frac{\left[\frac{WH}{2}\right]}{\left[\frac{WH^3}{L} + \frac{W^* H^{*3} \sin\theta}{L_s}\right]} \tag{6.37}$$

From Equation (6.32) we have

$$\frac{\partial(dP/dt)}{\partial N} = \left(\frac{P_i H^2}{6\mu L^2} + \frac{V}{2L}\right)\frac{\partial P_i}{\partial N} \tag{6.38}$$

$$\frac{\partial(dP/dt)}{\partial L} = \left(\frac{P_i H^2}{6\mu L^2} + \frac{V}{2L}\right)\frac{\partial P_i}{\partial L} - \left(\frac{P_i V}{2L^2} + \frac{P_i^2 H^2}{6\mu L^3}\right) \tag{6.39}$$

$$\frac{\partial(dP/dt)}{\partial V} = \left(\frac{P_i H^2}{6\mu L^2} + \frac{V}{2L}\right)\frac{\partial P_i}{\partial V} + \frac{P_i}{2L} \tag{6.40}$$

From Equation (6.34) we have

$$\frac{\partial D}{\partial N} = 0 \tag{6.41}$$

$$\frac{\partial D}{\partial L} = 0 \tag{6.42}$$

$$\frac{\partial D}{\partial V} = \mu \frac{1}{H} \tag{6.43}$$

In order to understand the relative effects of each of the PVs on each of the DPs we need to take some realistic values of the geometric parameters W, H, W*, H*, L, Ls, and D_b as well the operational parameters N and V and compute the effect that a change in each of the PVs has on the DPs.

We take the following values:

$H=0.030$ in
$W=0.160$ in
$L=0.5$ in
$D_b=1$ in
$H^*=0.150$ in
$W^*=1$ in
$L_s=30$ in
$\mu=600$ Pa-s
$N=25$ rpm
$V=50$ ft/min
$\theta=17°$

We also take some realistic changes in the values of some of the parameters that could be made during the running of an actual experiment. Thus, we assume the following:

$\Delta N=1$ rpm
$\Delta L=0.1$ in
$\Delta V=1$ ft/min

With the above realistic figures, the effects are computed, normalized, and summarized in Table 6.1. Each column is the effect of a particular PV on the DPs. For example the entry in row i and column j of the table is $\left(\frac{\partial DP_i}{\partial PV_j}\right)\Delta PV_j$.

		PVs		
		N	L	V
DPs	P_i	$\left(\frac{\partial P_i}{\partial N}\right)\Delta N = 0.99$	$\left(\frac{\partial P_i}{\partial L}\right)\Delta L = -0.04$	$\left(\frac{\partial P_i}{\partial V}\right)\Delta V = -0.13$
	dP/dt	$\left(\frac{\partial (dP/dt)}{\partial N}\right)\Delta N = 0.25$	$\left(\frac{\partial (dP/dt)}{\partial L}\right)\Delta L = -0.97$	$\left(\frac{\partial (dP/dt)}{\partial V}\right)\Delta V = -0.03$
	D	$\left(\frac{\partial D}{\partial N}\right)\Delta N = 0$	$\left(\frac{\partial D}{\partial L}\right)\Delta L = 0$	$\left(\frac{\partial D}{\partial V}\right)\Delta V = 1$

Table 6.1 Normalized table of effect of PVs on DPs.

It is easily seen from Table 6.1 that changing the die length L and the wire velocity V do not produce as great a change in the die inlet pressure as changing the extruder rpm N does. In fact the effect of changing the extruder rpm is an order-of-magnitude higher than the effect of the other two PVs on the die inlet pressure. It is also seen that changing the wire velocity V has insignificant effect on the pressure drop rate dP/dt when compared to the effect that changing N and L have on dP/dt. The design equation can thus be written down now as

$$\begin{bmatrix} P_i \\ dP/dt \\ D \end{bmatrix} = \begin{bmatrix} \varepsilon & O & O \\ \kappa & \nu & O \\ O & O & \upsilon \end{bmatrix} \begin{bmatrix} N \\ L \\ V \end{bmatrix} \tag{6.44}$$

The functions ε, κ, ν, and υ are given by

$$\varepsilon = \frac{\partial P_i}{\partial N} = 12\mu \frac{\left[\frac{\pi D_b W * H * \cos\theta}{120}\right]}{\left[\frac{WH^3}{L} + \frac{W * H *^3 \sin\theta}{L_s}\right]} \tag{6.45}$$

$$\kappa = \frac{\partial (dP/dt)}{\partial N} = \left(\frac{P_i H^2}{6\mu L^2} + \frac{V}{2L}\right)\frac{\partial P_i}{\partial N} \tag{6.46}$$

$$v = \frac{\partial (\mathrm{dP/dt})}{\partial \mathrm{L}} = \left(\frac{\mathrm{P_i H^2}}{6\mu \mathrm{L}^2} + \frac{\mathrm{V}}{2\mathrm{L}}\right)\frac{\partial \mathrm{P_i}}{\partial \mathrm{L}} - \left(\frac{\mathrm{P_i V}}{2\mathrm{L}^2} + \frac{\mathrm{P_i}^2 \mathrm{H}^2}{6\mu \mathrm{L}^3}\right) \tag{6.47}$$

$$\upsilon = \frac{\partial \mathrm{D}}{\partial \mathrm{V}} = \mu \frac{1}{\mathrm{H}} \tag{6.48}$$

Thus, it is seen that the design matrix relating DPs to PVs is also lower triangular. Thus we have an overall decoupled design. It should be mentioned here that the second design matrix is not a truly lower triangular matrix. In writing down the effect of L and V on P_i and of V on dP/dt we have considered order-of-magnitude changes and thus concluded that these three off-diagonal elements can be set to zero.

6.8 CHOICE OF OTHER PROCESS VARIABLES

In the above design the extruder rpm N, the die length L, and the wire velocity V were chosen as PVs. One can also pick the die annular opening H as a PV used to control either P_i or dP/dt. If such a choice is made, then the entire analysis needs to be carried out again to see if the design satisfies the Independence Axiom.

6.9 CONCLUSION

The process of coating a wire with microcellular foam has been analyzed from the perspective of Axiomatic Design. It is seen that the design is a decoupled one which will enable the actual adjustment of PVs to satisfy the FRs in the functional domain. Thus, we have a controllable design with which to perform experiments and characterize the process.

CHAPTER 7

DESIGN SPECIFICATIONS OF THE TANDEM EXTRUSION SYSTEM COMPONENTS

7.1 INTRODUCTION

After the completion of a detailed analysis of nucleation and cell growth mechanisms and a preliminary design and analysis of the proposed extrusion system with the aid of Axiomatic Design tools, the final fabrication of all the components and assembly is undertaken. This chapter discusses in detail the specifications for all the important components.

7.2 PRIMARY EXTRUDER SPECIFICATIONS

The primary extruder is a 1" diameter Wayne 'Yellow Jacket' table top extruder with 25:1 L/D ratio. The power input into the control cabinet is 230V 3-phase AC while the 3 HP DC motor provides a range of screw speeds between 0 and 100 rpm. Three 1400W heating zones with closed loop temperature controllers keep the nitrided barrel at the specified temperature. A pressure tap at 18.5D (18.5 times the diameter) from the feed zone could be used for gas injection into the polymer melt. A schematic of the primary extruder is shown in Figure 7.1.

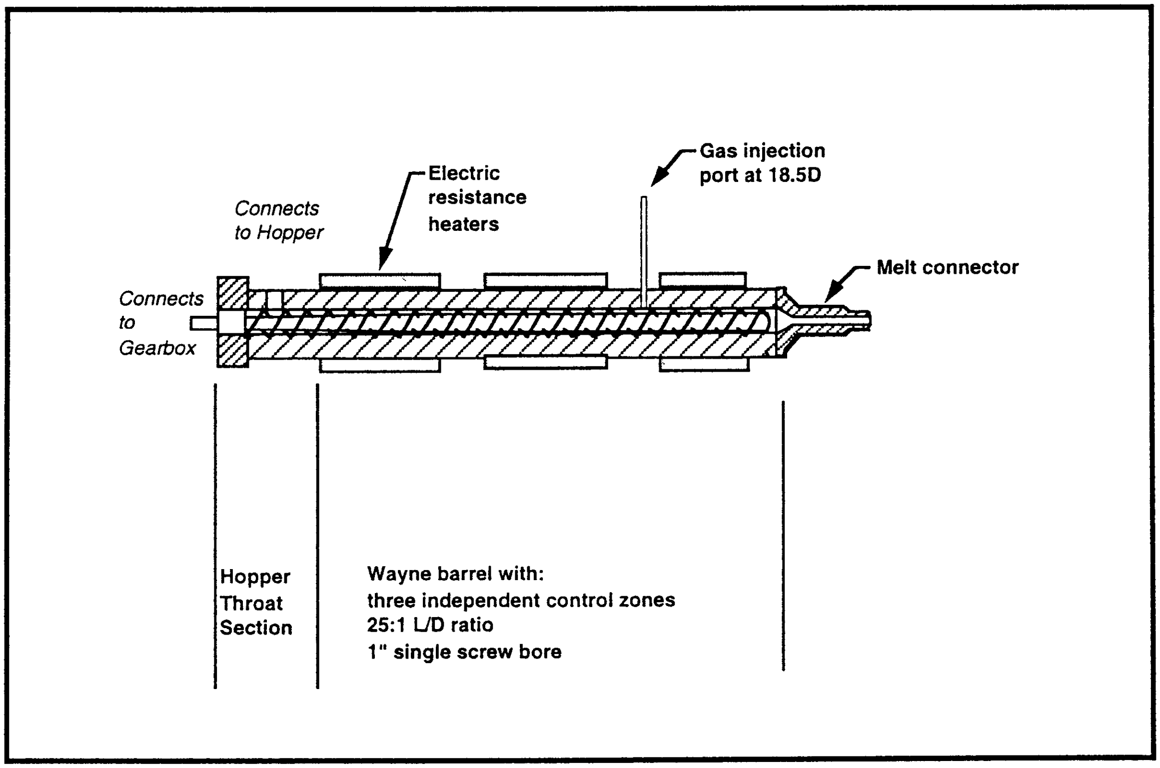

Figure 7.1 Primary extruder schematic.

7.3 PRIMARY SCREW DESIGN SPECIFICATIONS

The screw for the primary or first stage extruder is a 1" diameter, 25:1 L/D 4140 flame hardened, chrome plated screw from Wayne Machine and Die Company. The screw has standard feed and melting zone and two Maddox mixing sections each of 2D (two times the diameter) length. The first Maddox section is centered at 12.5 D while the second is centered at 22.5D. The root diameter of the screw at 18.5D is 0.625", which enables low pressure to be generated at this point. This low pressure at 18.5D is necessary for gas injection through the pressure port. The first Maddox section homogenizes the polymer melt and creates an adverse pressure gradient to prevent gas backflow. In the event that some gas flows back, this mixing section would insure that this gas is dispersed in the polymer melt and forced to flow forward with the polymer melt. After gas injection at 18.5D, melt repressurization occurs before reaching the second Maddox section which serves to disperse the gas uniformly throughout the polymer melt in the form of small bubbles. A schematic of the primary extruder is shown in Figure 7.2.

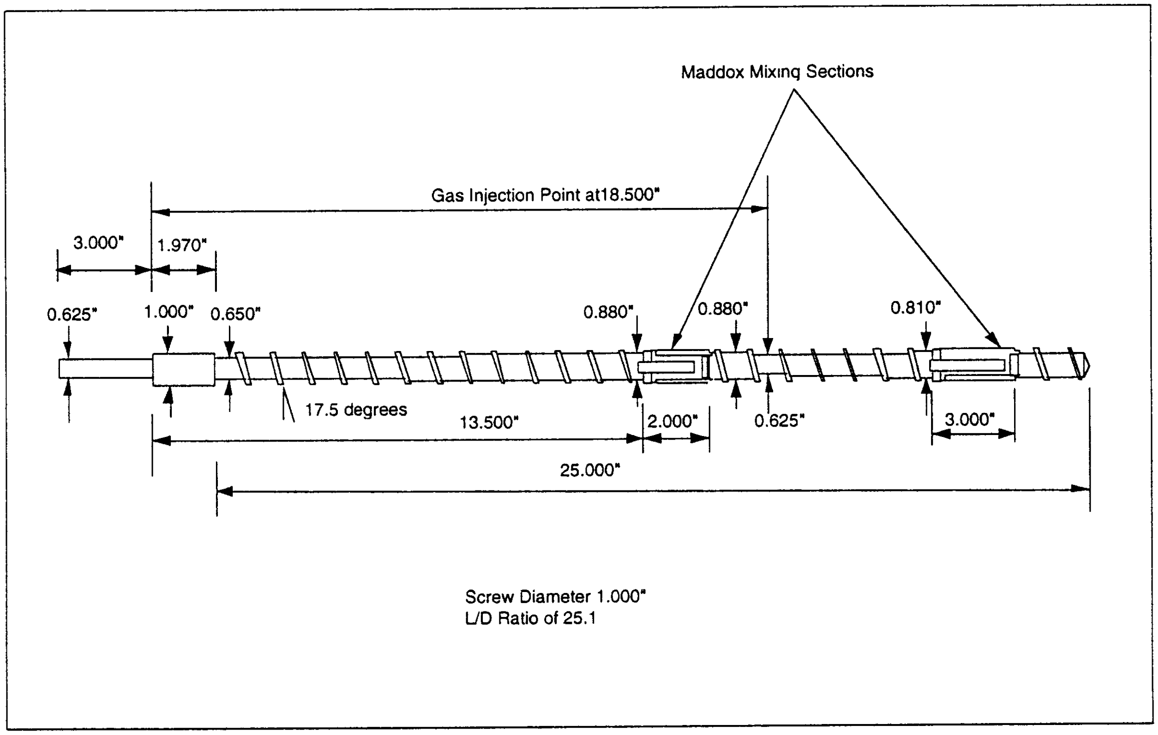

Figure 7.2 Primary extruder screw.

7.4 SECONDARY EXTRUDER SPECIFICATIONS

The secondary extruder is a 1" diameter, 30:1 L/D ratio Royle extruder with a Xaloy lined barrel which makes it possible to process corrosive resins such as Teflon. The barrel has five independently controlled heating zones where 1350W cast bronze electric resistance heaters supply heat. Additional active temperature control at these five zones is also provided by five independent air fans. Four additional heating zones are provided for use with extruder head assemblies. The barrel has a venting port at 16.5D from the gear box end which could be used as a gas injection port. However, since gas is injected in the primary extruder, this port is not used and is sealed using a stainless steel plug. Power to the screw is supplied by a 3 HP DC motor with a maximum limit on the armature current of 14.6 Amps. The power supply to the control is 480V, 3 Phase, 50 Amp source. Figure 7.3 shows a schematic of the secondary extruder.

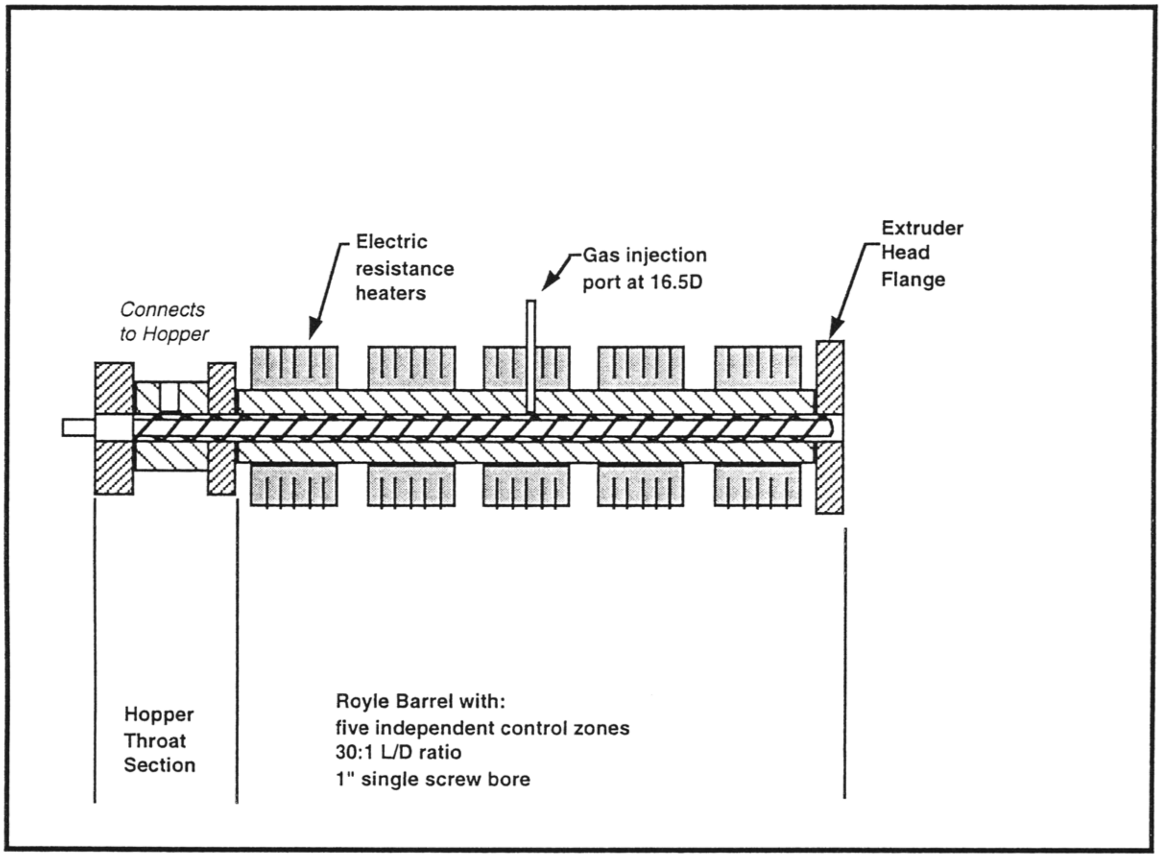

Figure 7.3 Secondary extruder schematic.

7.5 SECONDARY SCREW DESIGN SPECIFICATIONS

The secondary extruder screw is a 1" diameter, 30:1 chrome plated screw from Davis-Standard. It has a slight taper with an average channel depth of 0.150". The primary function of this screw is to allow sufficient residence time for complete diffusion of the gas bubbles into the polymer in order to form a single-phase homogeneous solution while pressurizing this solution simultaneously. Figure 7.4 shows the design specifications of the secondary extruder screw.

7.6 PRIMARY-SECONDARY ADAPTER SECTION AND DYNAMIC POLYMER SEAL

The two extruders are connected in series in a tandem arrangement which required the redesign and replacement of the hopper throat section of the Royle extruder. The adapter section provides a passage for the flow of pressurized polymer with dispersed gas bubbles from the Wayne extruder into the Royle extruder. Figure 7.5 shows the schematic of the entire tandem extrusion system while the specifications of this adapter are shown in Figure 7.6.

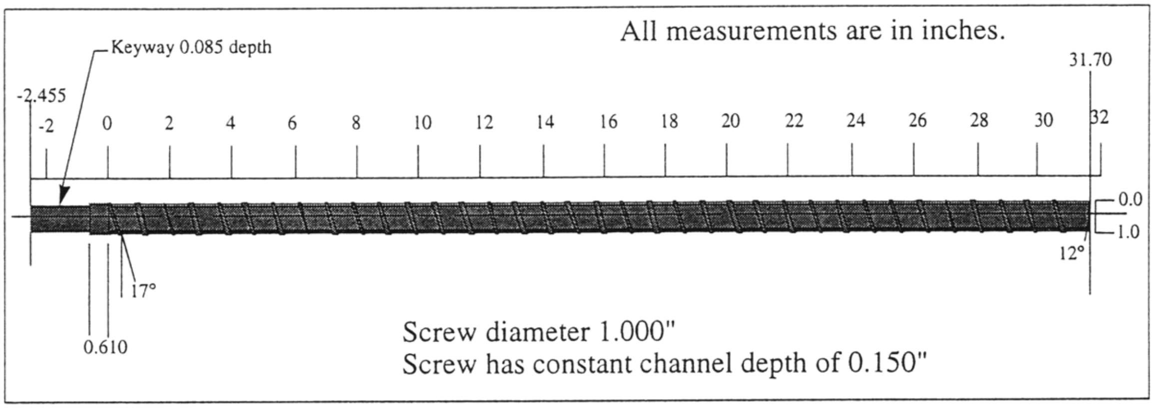

Figure 7.4 Secondary extruder screw.

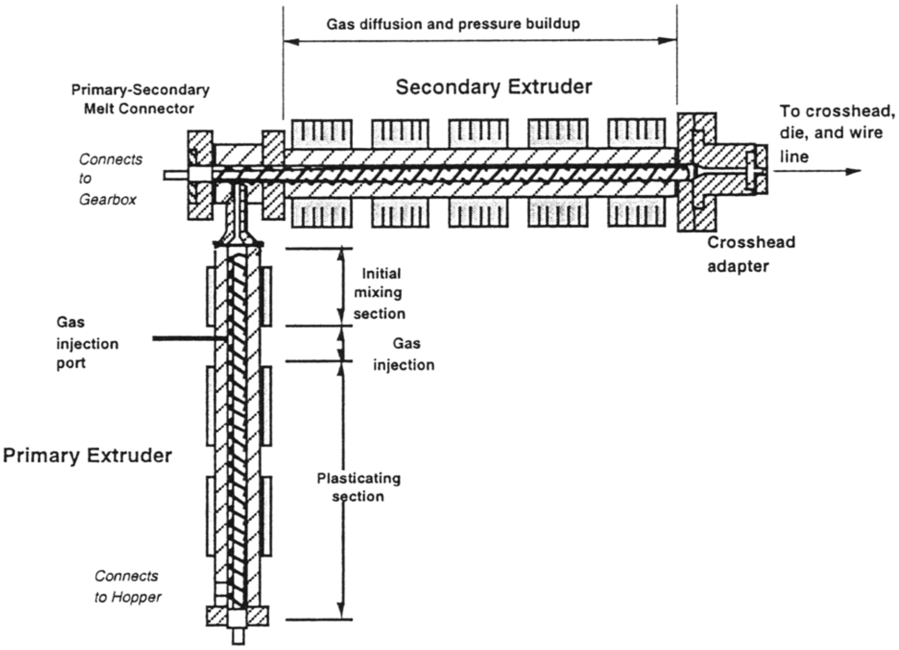

Figure 7.5 Tandem extrusion system schematic.

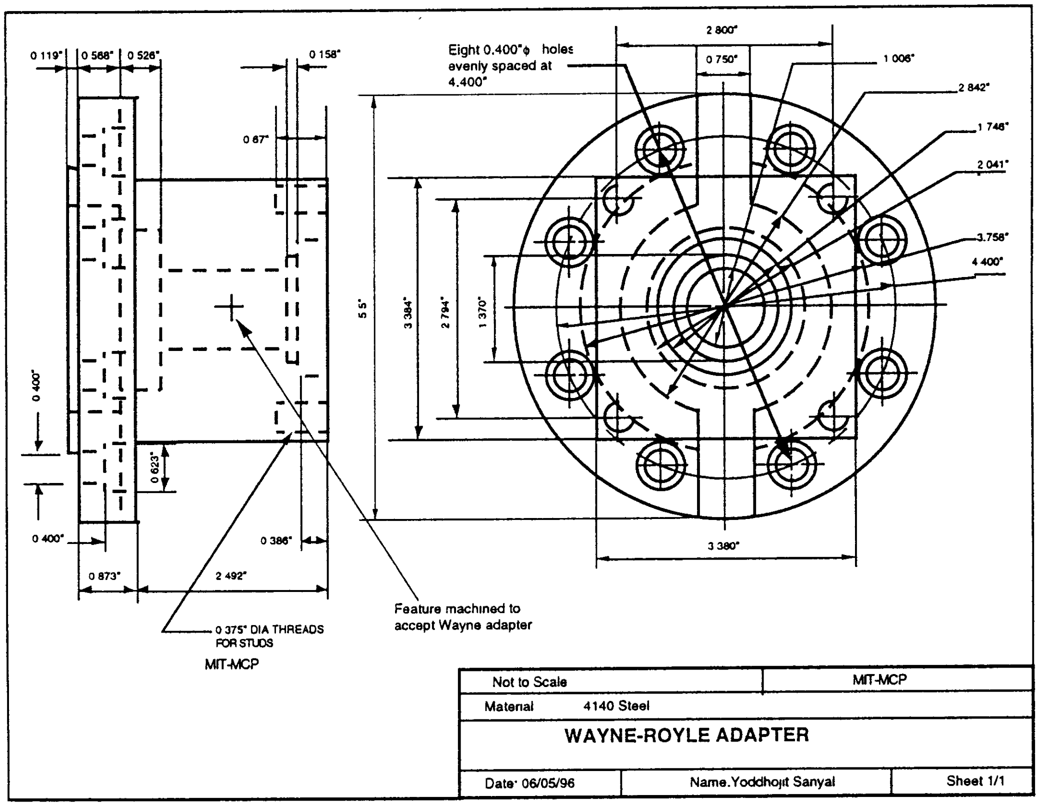

Figure 7.6 Wayne-Royle adapter.

The dynamic polymer seal is a seal of highly viscous polymer in between a bronze bearing and the rotating Royle extruder screw. The viscosity of this polymer seal is very important for preventing leakage of the high pressure polymer with dispersed gas bubbles in it. The viscosity is controlled by the temperature which can be varied by cooling the seal by means of circulating water in the cooling passages in the bronze bearing. Figure 7.7. The temperature of the adapter section and the dynamic polymer seal have to be controlled carefully and precisely in order to have the flow at a high enough temperature for feeding into the secondary extruder while at the same time ensuring that the viscosity of the seal high enough to prevent high pressure leakage.

7.7 GAS INJECTION SYSTEM

Carbon dioxide and nitrogen are both used for foam production. Grade 2.8 (99.8% pure), bone dry carbon dioxide at 850 psi is drawn from a cylinder into a liquefaction chamber. Liquid carbon dioxide is then injected into the barrel of the extruder by a positive displacement type metering pump. This gas injection system overview is shown in Figure 7.8.

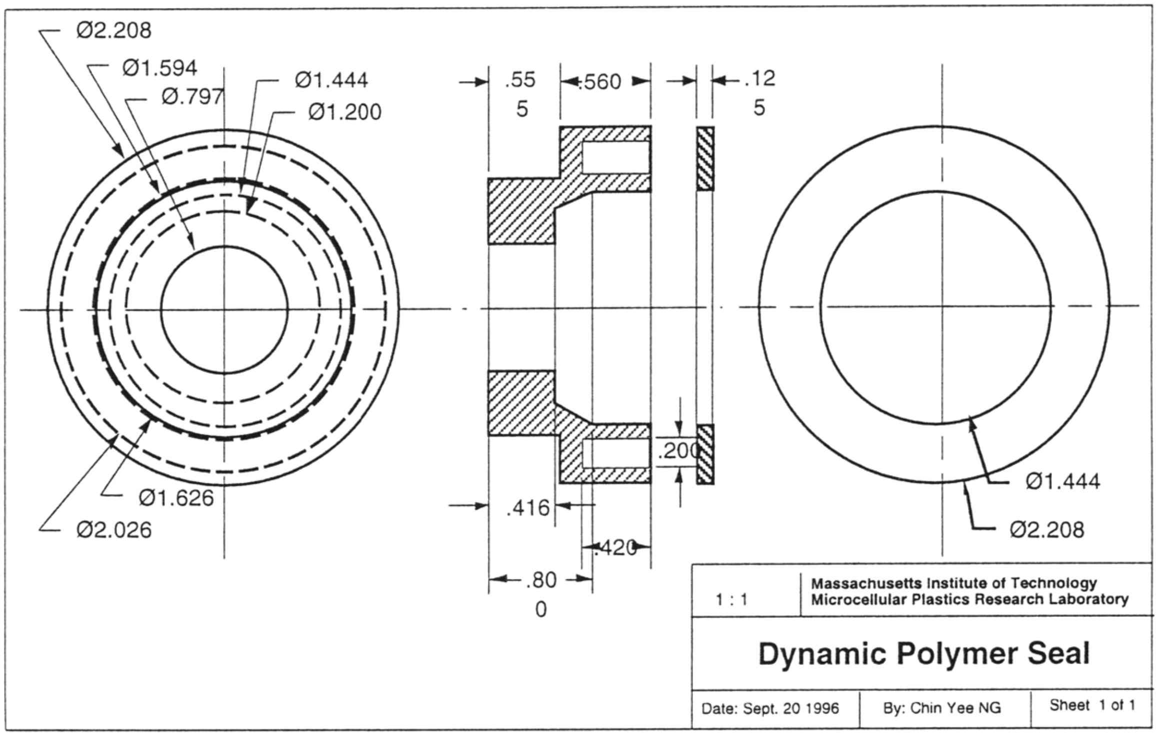

Figure 7.7 Main housing of the dynamic polymer seal.

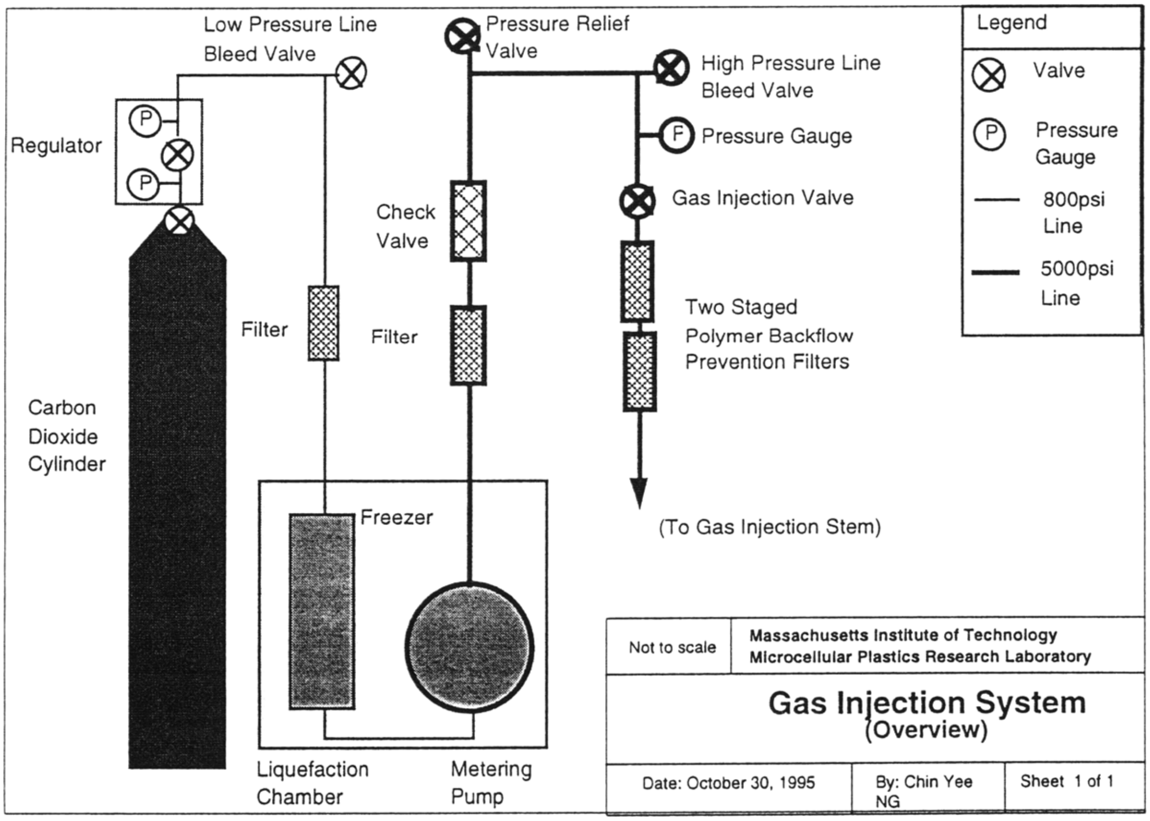

Figure 7.8 Gas injection system schematic.

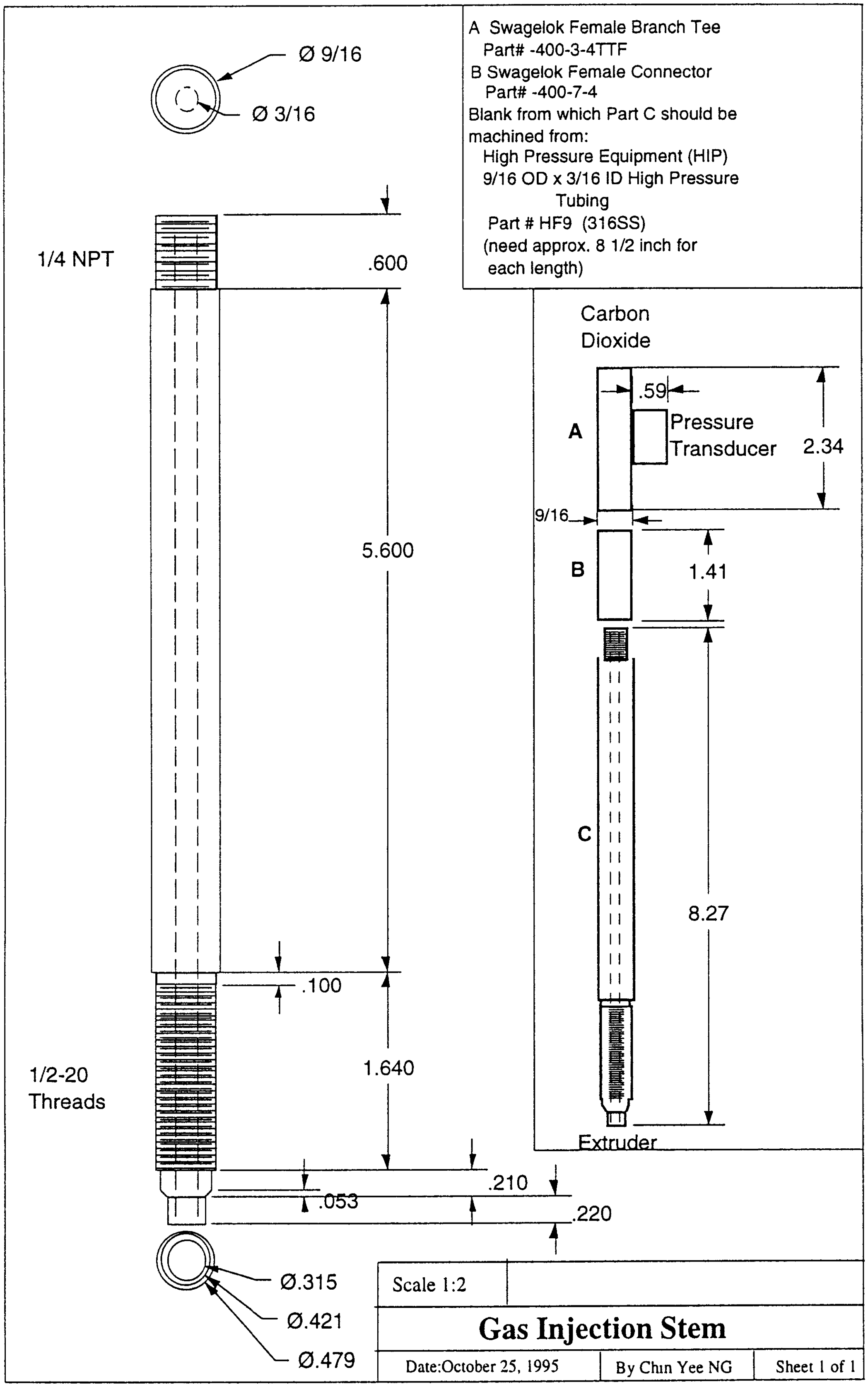

A Swagelok Female Branch Tee
Part# -400-3-4TTF
B Swagelok Female Connector
Part# -400-7-4
Blank from which Part C should be machined from:
High Pressure Equipment (HIP)
9/16 OD x 3/16 ID High Pressure Tubing
Part # HF9 (316SS)
(need approx. 8 1/2 inch for each length)

Scale 1:2

Gas Injection Stem

Date:October 25, 1995 | By Chin Yee NG | Sheet 1 of 1

Figure 7.9 Gas injection stem.

For nitrogen, the gas is drawn from a high pressure cylinder, throttled to the desired pressure and then injected into the barrel.

7.8 WIRE COATING CROSSHEAD DESIGN

The crosshead assembly is shown in Figure 7.10. The crosshead turns the flow emerging from the Royle extruder through 90 degrees. The crosshead houses the wire guide and the die that is used for coating the foamed insulation on the wire. The crosshead is attached to the extruder head flange through a crosshead adapter.

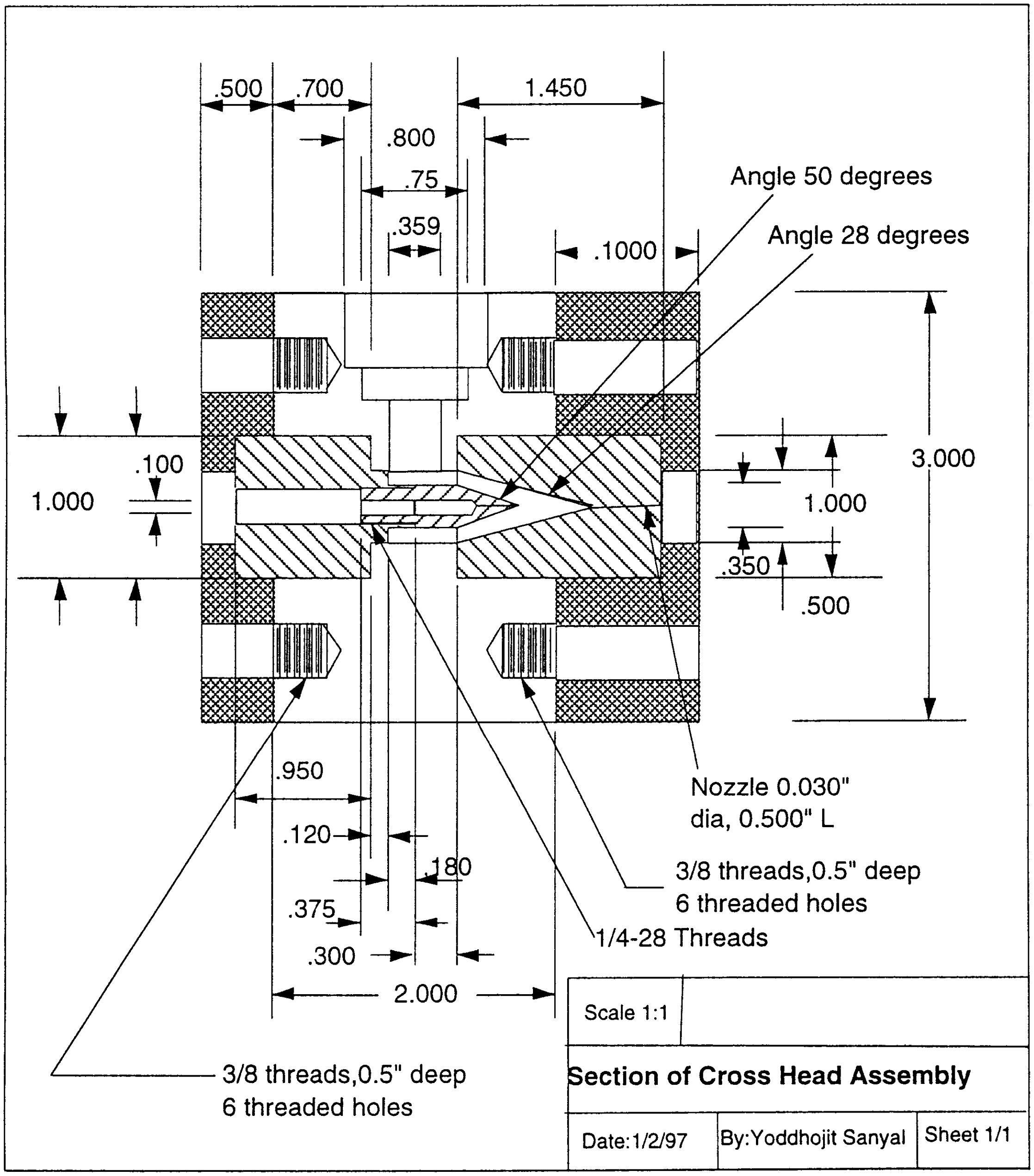

Figure 7.10 Cross head assembly section.

Figure 7.11 shows the wire guide, the guide attachment, and the wire coating die. The wire guide and die shown in Figure 7.11 is that used for a 30 AWG (0.030"ϕ) wire. The type of die used is a pressure extrusion die. It is seen that the polymer comes in contact with the conductor inside the die and is then extruded under high pressure. Figures 7.12 and 7.13 show the wire coating die holder flange and the wire guide attachment holder flange respectively.

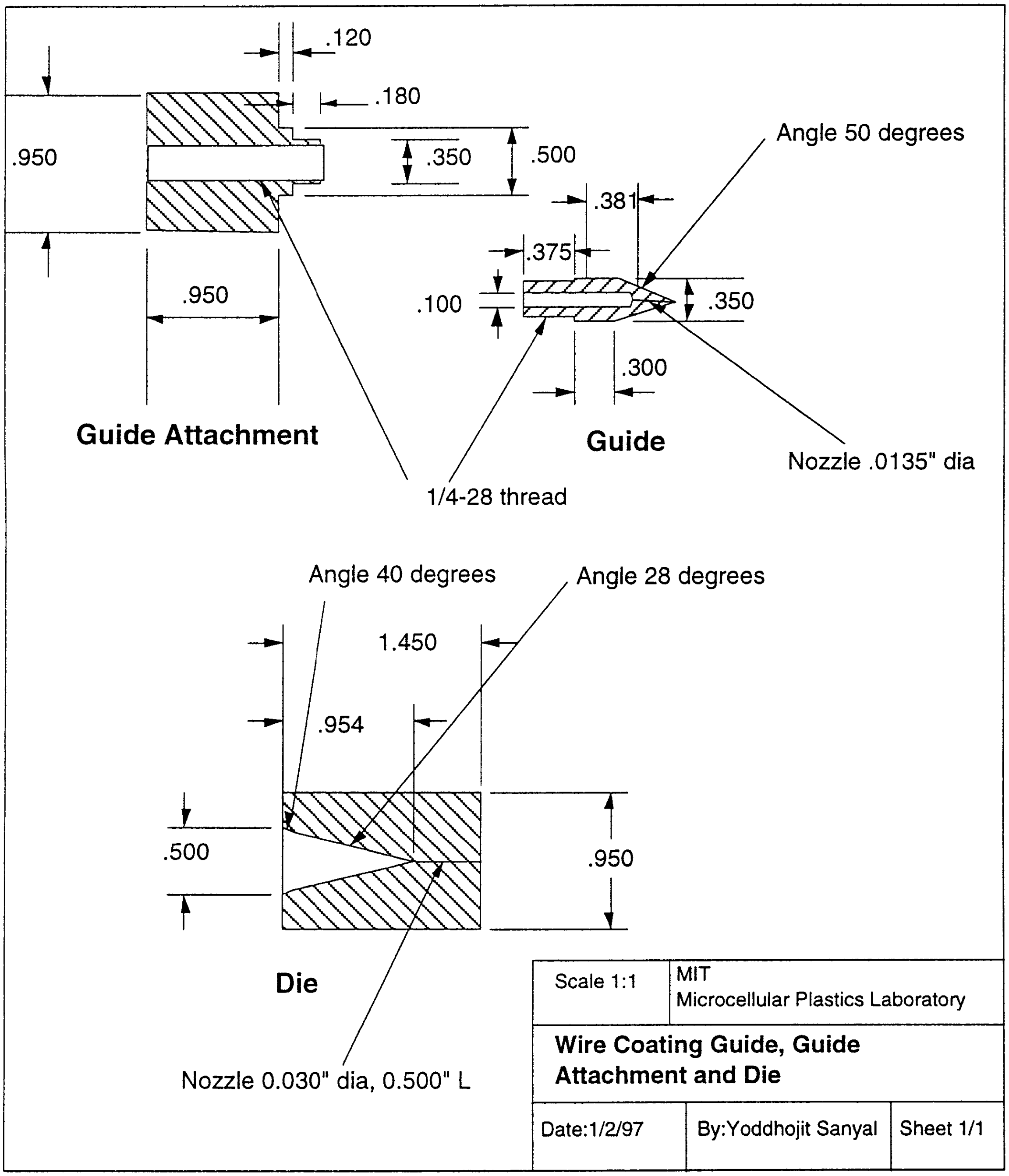

Figure 7.11 Wire coating guide, guide attachment, and die.

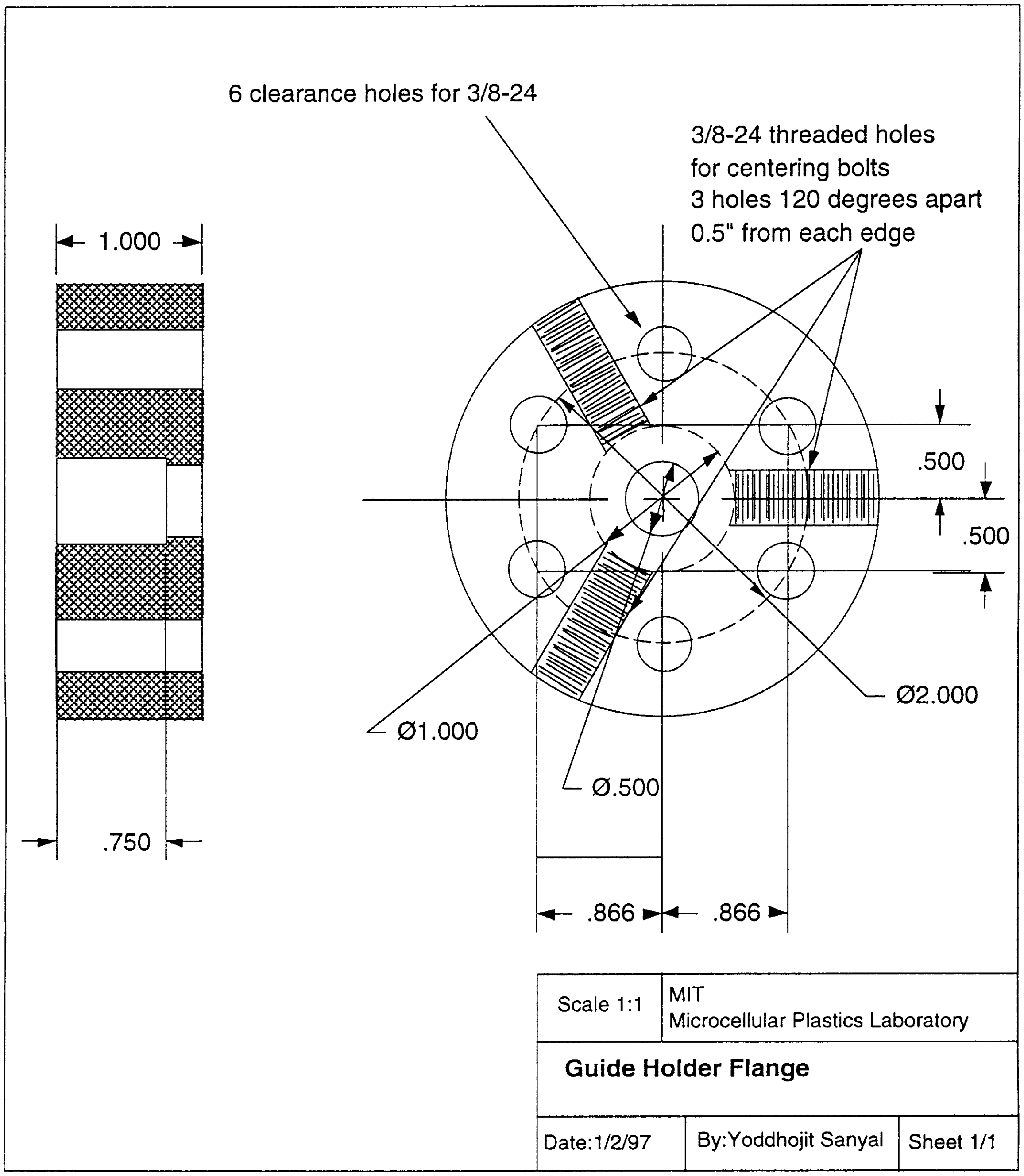

Figure 7.12 Die holder flange.

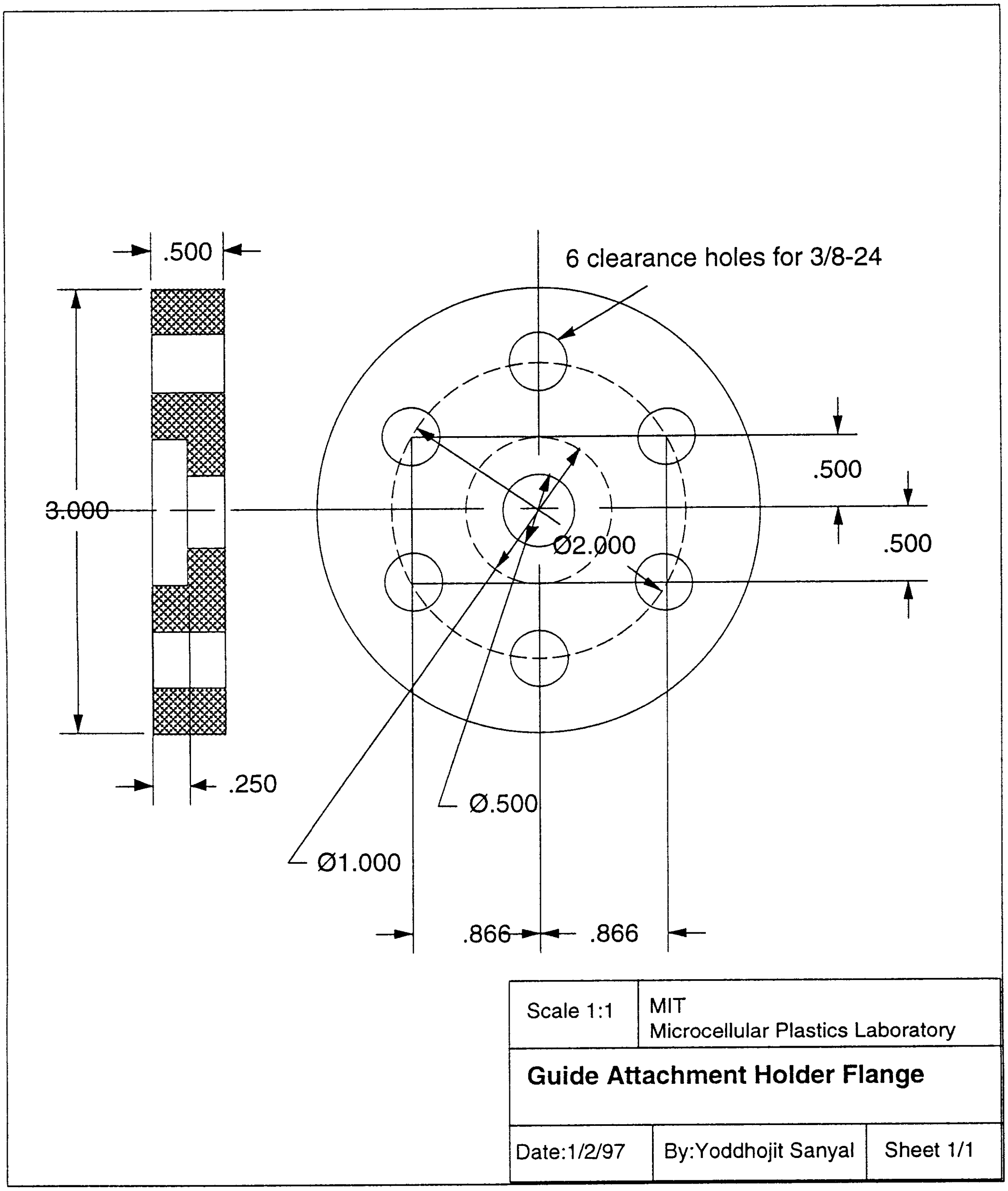

Figure 7.13 Guide attachment holder flange.

7.9 FILAMENT EXTRUSION DIE AND FLANGE DESIGN

In addition to designing the guide, die and accessories for extrusion of microcellular wire coating, fabrication of dies and flanges for extrusion of filaments is necessary at this point since the initial plan consisted of producing microcellular filaments first in order to evaluate and confirm important foaming parameters. These design specifications are shown in Figures 7.14, 7.15, 7.16, and 7.17.

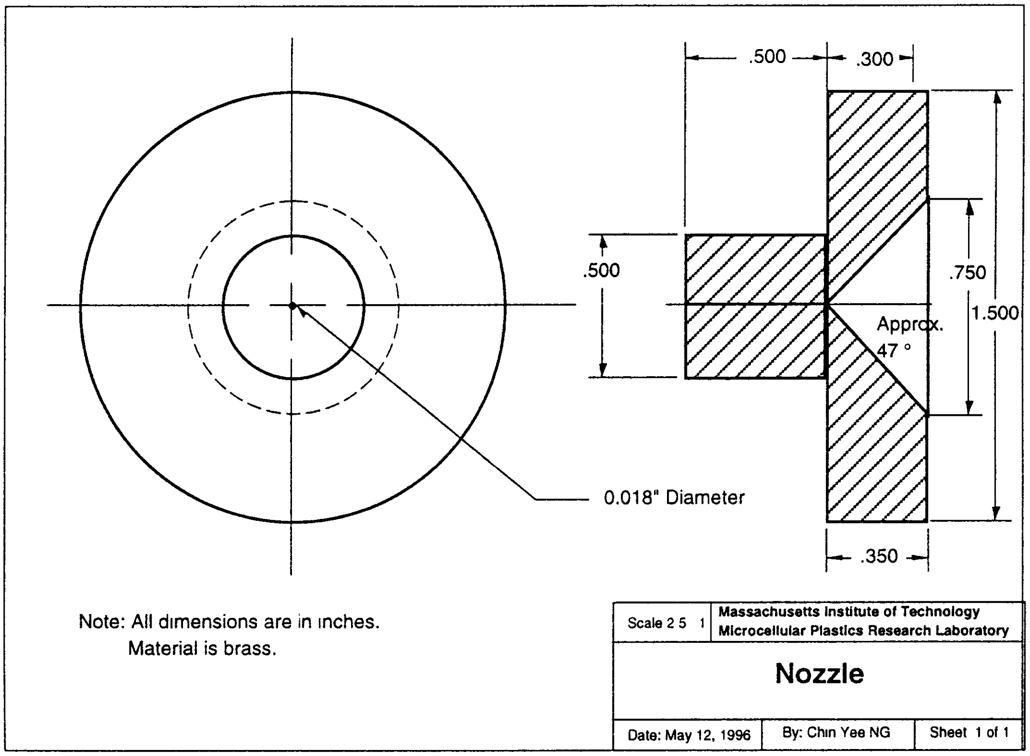

Note: All dimensions are in inches.
Material is brass.

Scale 2.5 : 1
Massachusetts Institute of Technology
Microcellular Plastics Research Laboratory

Nozzle

Date: May 12, 1996
By: Chin Yee NG
Sheet 1 of 1

Figure 7.14 Nozzle/die for filament extrusion.

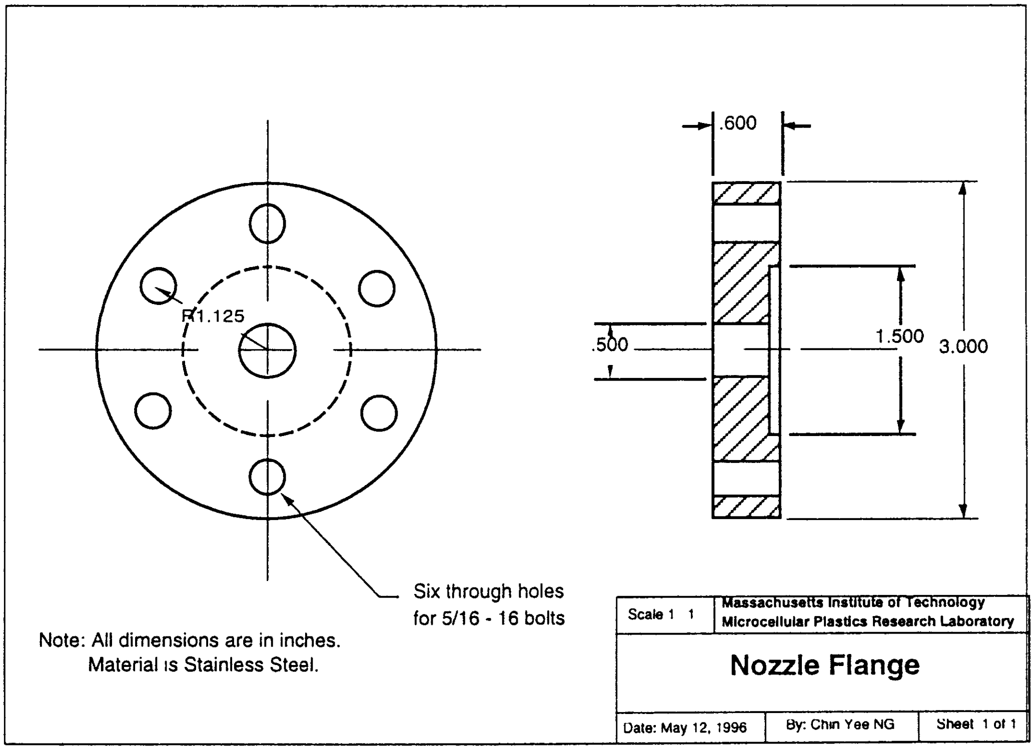

Six through holes
for 5/16 - 16 bolts

Note: All dimensions are in inches.
Material is Stainless Steel.

Scale 1 : 1
Massachusetts Institute of Technology
Microcellular Plastics Research Laboratory

Nozzle Flange

Date: May 12, 1996
By: Chin Yee NG
Sheet 1 of 1

Figure 7.15 Nozzle/die flange.

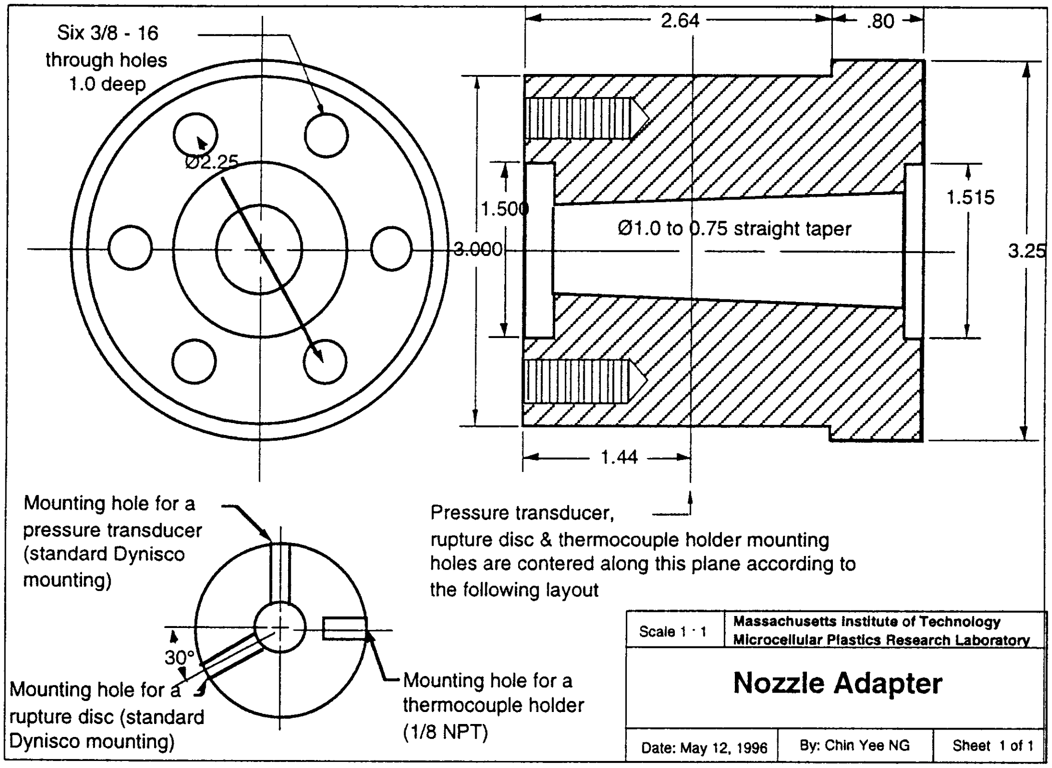

Figure 7.16 Nozzle adapter.

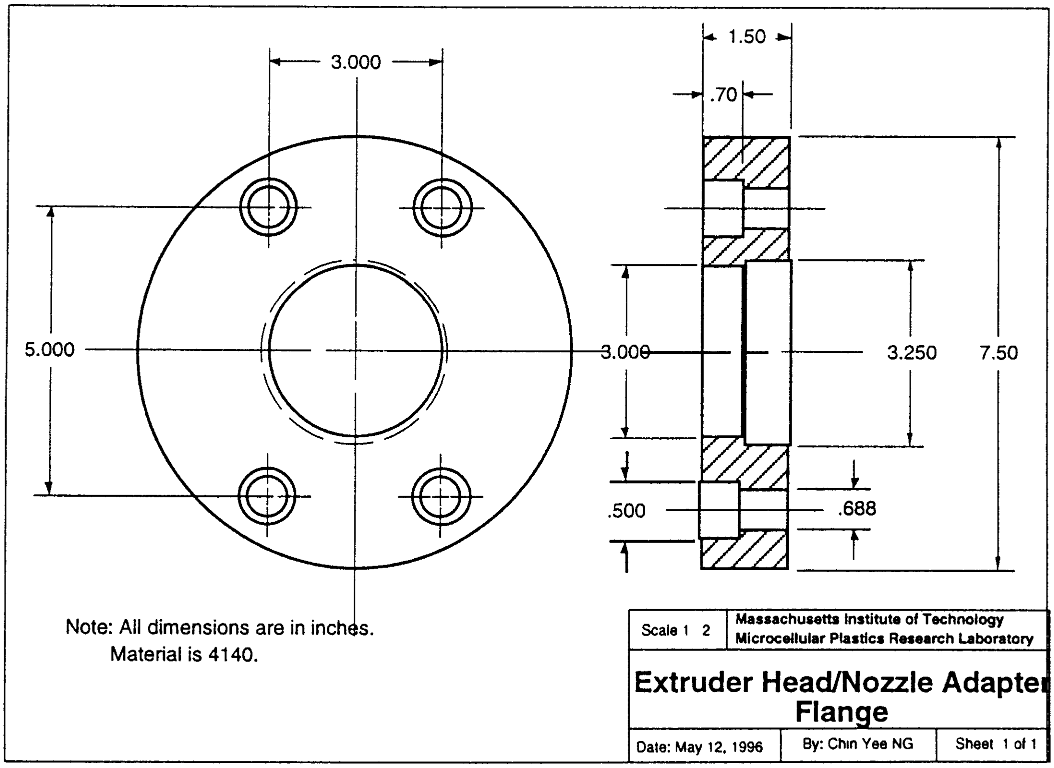

Figure 7.17 Extruder head/nozzle adapter flange.

7.10 CONCLUSION

The design of the various components and sub-components of the tandem extrusion system required considerations of performance during operation as well as important constraints such as adaptability and space. Efforts were made to install standard components and equipment wherever it was possible to do so. However, in numerous cases, items and components had to be custom-built in order to be attached and operate in synchronization with two single screw extruders which were connected in tandem. As a recommendation for future machines built for this purpose, it is strongly urged that designers consider the issue of adaptability of components between the two extruders.

CHAPTER 8

EXPERIMENTS WITH THE TANDEM EXTRUSION SYSTEM

8.1 INTRODUCTION

This chapter discusses the results of experiments with the tandem extrusion system and how these results compare with the predictions made with the nucleation and cell growth model developed in Chapter 4. The experiments involved the extrusion of both filaments and wire coatings. The resin used for most of the experiments was Quantum Chemical's Petrothene PP 1610-PF. Both nitrogen and carbon dioxide were injected into the molten resin at different gas injection pressures and differences between the quality of the foam were noted. Thus, the effects of saturation pressure, die geometry, die temperature, and type of gas used were evaluated experimentally and compared with analytical predictions.

8.2 FILAMENT EXTRUSION EXPERIMENTS

The first series of experiments were conducted using filament dies. Two sets of nozzles/dies were used for this purpose. Each set had ten nozzles varying in length from 0.050" to 0.500" in steps of 0.050". The diameter of the first set was 1/32"(0.03125") while that of the second set was 0.020". The L/D ratio of the two different sets of nozzles used is shown in Table 8.1.

Length, L [inch]	L/D ratio of 0.03125"ϕ dies	L/D ratio of 0.020"ϕ dies
0.050	1.6	2.5
0.100	3.2	5.0
0.150	4.8	7.5
0.200	6.4	10.0
0.250	8.0	12.5
0.300	9.6	15.0
0.350	11.2	17.5
0.400	12.8	20.0
0.450	14.4	22.5
0.500	16.0	25.0

Table 8.1 L/D ratios of 0.03125"ϕ and 0.020"ϕ dies.

8.2.1 Experiments with the 0.03125"ϕ die set with PP and N_2 injection

Effect of Die Geometry

Table 8.2 summarizes the experimental conditions and data for the extrusion of filaments using the die of 0.03125"ϕ. The Wayne extruder (primary) rpm is kept constant at 70 while the Royle (secondary) rpm is fixed at 25 for the entire set of nozzles. Each L/D ratio corresponds to a different pressure drop through the die (nozzle pressure). The adapter pressure also varies with change in the L/D ratio. The nozzle and adapter pressures are measured on-line. The gas injection pressure is varied in accordance with the adapter pressure to inject the desired amount of gas.

Samples are collected for specific intervals of time and the average mass flow rate is calculated based on several samples. The samples were weighed in air and then under water. The difference in these two readings was the volume of the sample since the specific gravity of water is 1. The density was calculated by taking the ratio of the mass of a sample to its volume. Figures 8.1, 8.2, 8.3, 8.4, and 8.5 represent the results graphically.

Figure 8.1 shows the relation between the volumetric flow rate and the L/D ratio. It is seen from Figure 8.1 that the volumetric flow rate is quite insensitive to the L/D ratio and is roughly 55cc/min throughout the entire L/D ratio range. Figure 8.2 shows that the nozzle pressure (or die inlet pressure) increases with die L/D which implies higher restriction to the flow. The adapter pressure and gas injection pressure also increase with L/D ratio but the effect is not as pronounced as that on the nozzle pressure.

0.03125"ϕ Dies

Resin	Quantum PP1610PF					
Gas	Nitrogen					
Extruder rpms	Wayne: 70					
	Royle: 25					
Temperature Settings						
	Wayne	Zone 1: 350°F	Royle	Zone 1: 375°F	Head Flange:	375°F
		Zone 2: 375°F		Zone 2: 375°F	Nozzle/Die:	375°F
		Zone 3: 375°F		Zone 3: 375°F		
		Zone 4: 375°F		Zone 4: 375°F		
		Adapter: 225°F		Zone 5: 375°F		

L [inch]	L/D	Gas Injection Pressure [psi]	Adapter Pressure [psi]	Nozzle Pressure [psi]	Average Density [g/cc]	Average Mass Flow Rate [g/cc]	Volume Flow Rate [cc/min]	$\Delta P/\Delta t$ [10^6 psi/s]
0.050	1.6	1200	1200	1250	0.72	40.9	56.7	1.880
0.100	3.2	1400	1300	1300	0.70	38.6	55.0	0.948
0.150	4.8	1400	1200	1475	0.71	39.0	55.3	0.721
0.200	6.4	1400	1300	1600	0.70	38.5	54.7	0.580
0.250	8.0	1600	1450	1800	0.69	38.2	55.3	0.528
0.300	9.6	1600	1500	1900	0.66	37.3	56.6	0.475
0.350	11.2	1700	1600	2000	0.64	36.7	57.2	0.433
0.400	12.8	1700	1600	2000	0.65	36.6	56.0	0.371
0.450	14.4	1700	1600	2350	0.66	35.3	53.4	0.370
0.500	16.0	1800	1750	2450	0.63	34.2	54.5	0.354

Table 8.2 Experimental conditions and data for the 0.03125"ϕ die set with nitrogen injection.

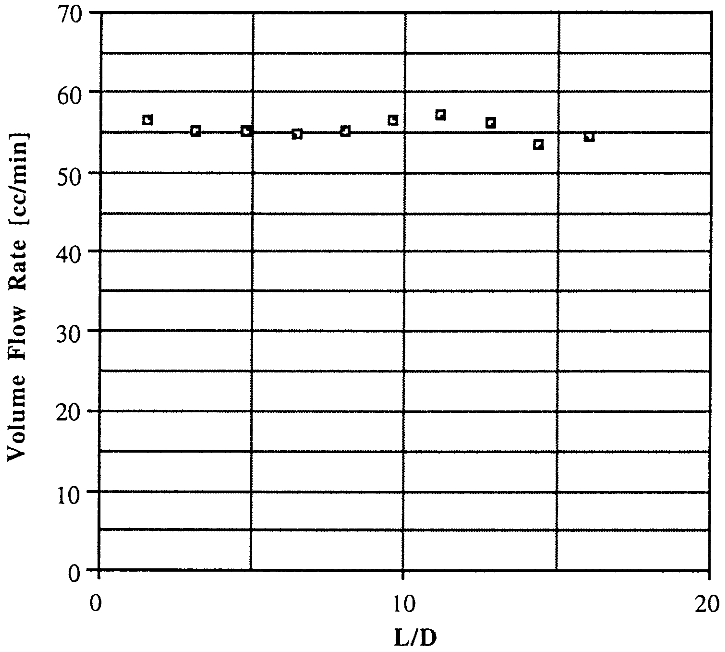

Figure 8.1 Plot of flow rate versus die L/D ratio for the 0.03125'"ϕ die set with PP and nitrogen injection.

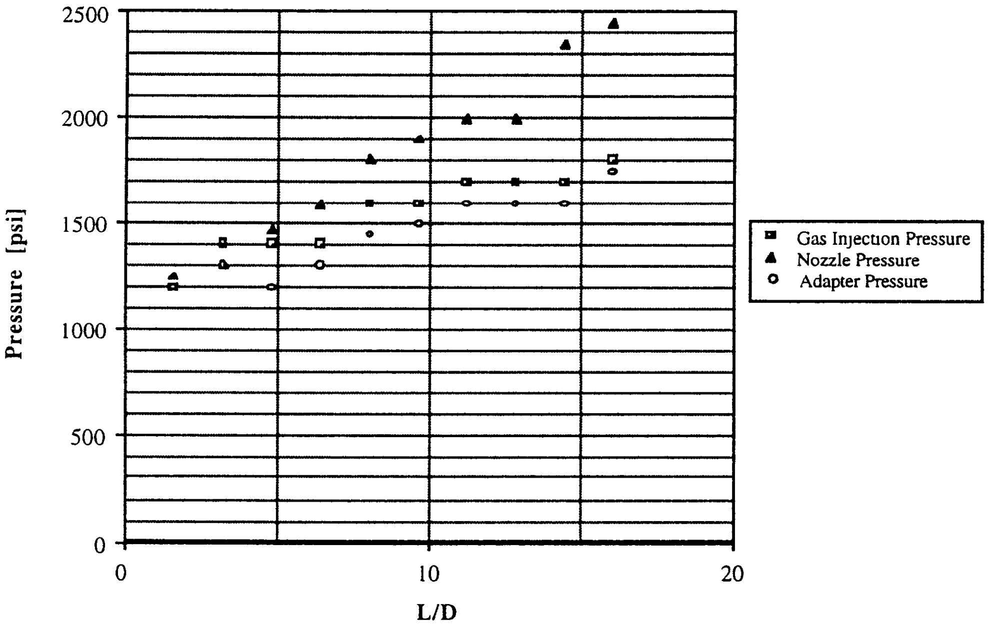

Figure 8.2 Plot of processing pressures versus die L/D ratio for the 0.03125"ϕ die set with PP and nitrogen injection.

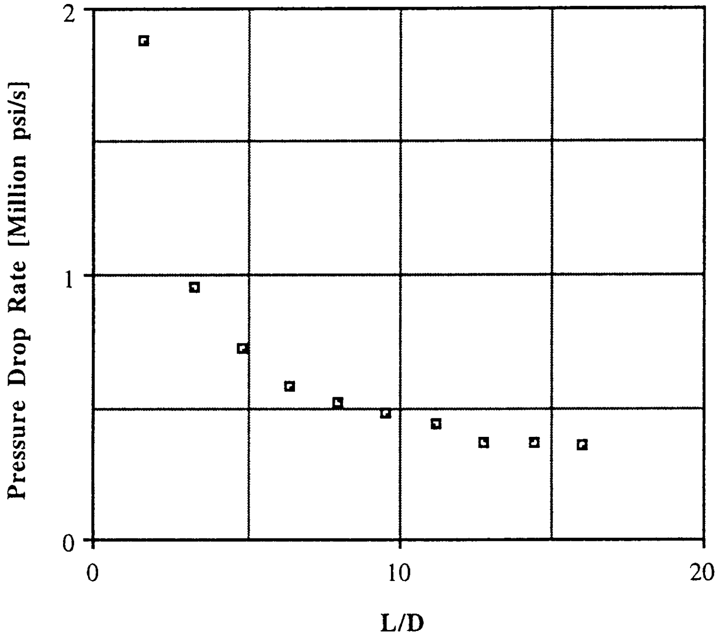

Figure 8.3 Plot of approximate pressure drop rate ($\Delta P/\Delta t$) versus die L/D ratio for the 0.03125"ϕ die set with PP and nitrogen injection.

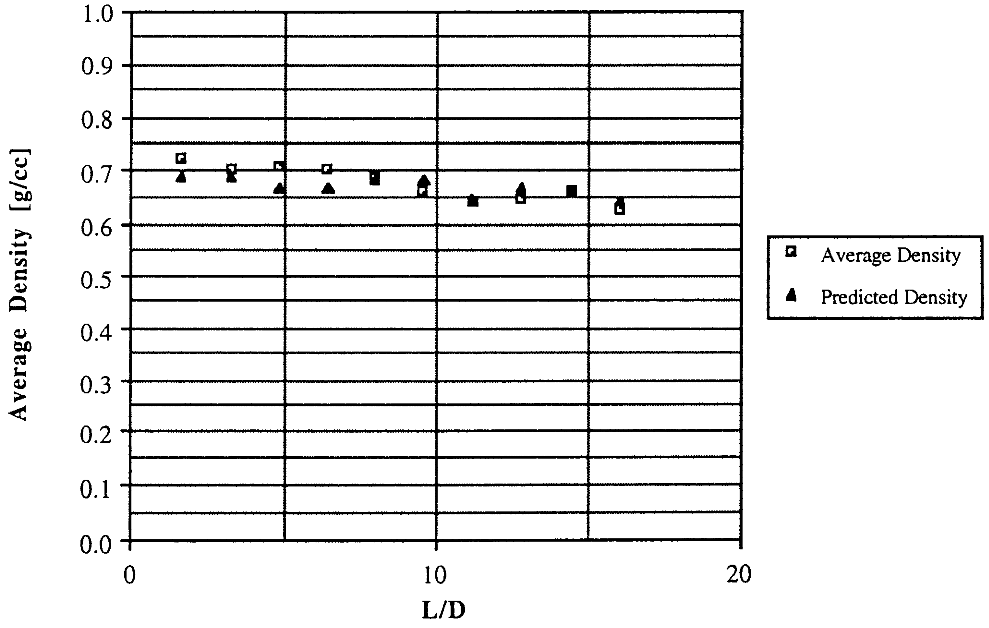

Figure 8.4 Plot of average foam density versus die L/D ratio for the 0.03125"ϕ die set with PP and nitrogen injection.

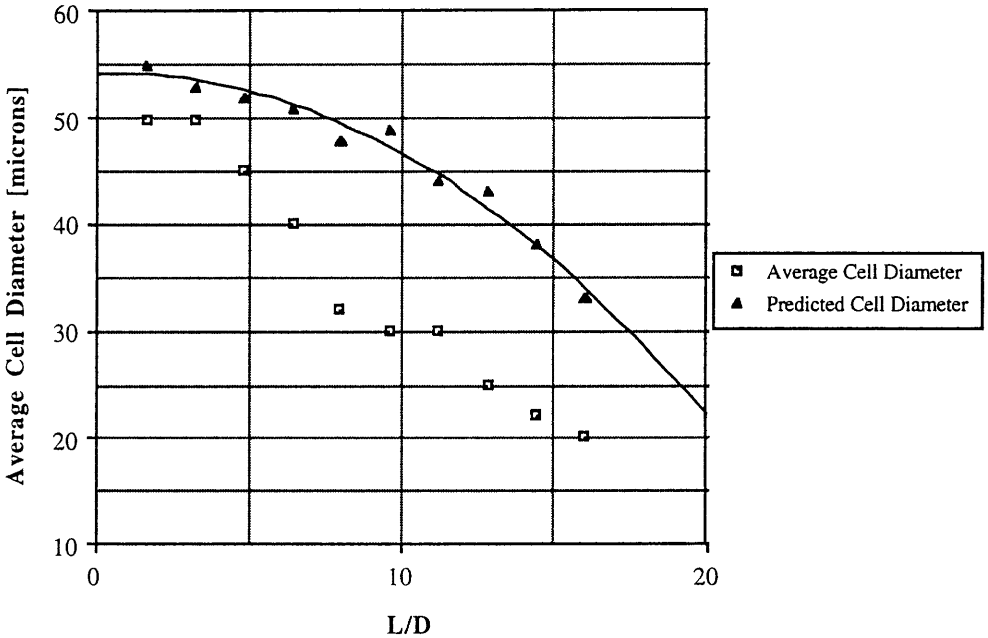

Figure 8.5 Plot of experimental and theoretically predicted average cell size for the 0.03125"ϕ die set with PP and nitrogen injection.

Figure 8.3 shows that the approximate pressure drop rate calculated for the experiments decreases as the die L/D ratio increases. The pressure drop rate is calculated by taking the ratio of pressure drop ΔP across the die to the residence time Δt of the flow in the die. The experimentally observed foam density is plotted in Figure 8.4 together with the theoretically predicted ones for the experimental conditions. Figure 8.5 shows the average cell size as a function of die L/D ratio. It is seen that the theoretical model developed in Chapter 4 over-estimates the cell size while the average foam density predictions are below those of the actual results. Figures 8.6 and 8.7 show some sample micrographs from this set of experiments.

It should be noted that the assumption of unrestricted cell growth inside the die by assuming expansion in the free volume space of the polymer would lead us to expect that the predicted cell size would be larger than the actual cell size. Thus, the experimental results and predictions shown in Figure 8.5 can be used to confirm that this assumption of unrestricted diffusion-driven growth of the cells needs to be modified in future work involving the analytical prediction model. However, as die length decreases (decreasing L/D ratio), the error in cell size prediction decreases because for shorter dies (say 0.100" length) most of the cell growth process takes place outside the die. The short residence time of the flow inside the die insures that the diffusion of gas from the bulk solution to the nucleated clusters does not proceed to any significant extent by the time the flow exits the die. Thus, the bulk solution is still rich in dissolved gas when the flow emerges from the die and most of the cell growth process occurs outside the die where the assumption of free growth/expansion of the cell walls is probably valid. The cell densities (number of cells per unit volume of the final foamed material) are of the order of about 10^7 to 10^8 cells per cm^3.

The results show that the analytical method developed in Chapter 4 to quantitatively treat the phenomenon of simultaneous nucleation and cell growth process during extrusion is successful from a qualitative standpoint. The cell size predictions can vary from the actual results by as much as 40% while the prediction of final foam density is about 10% below those of the actual ones.

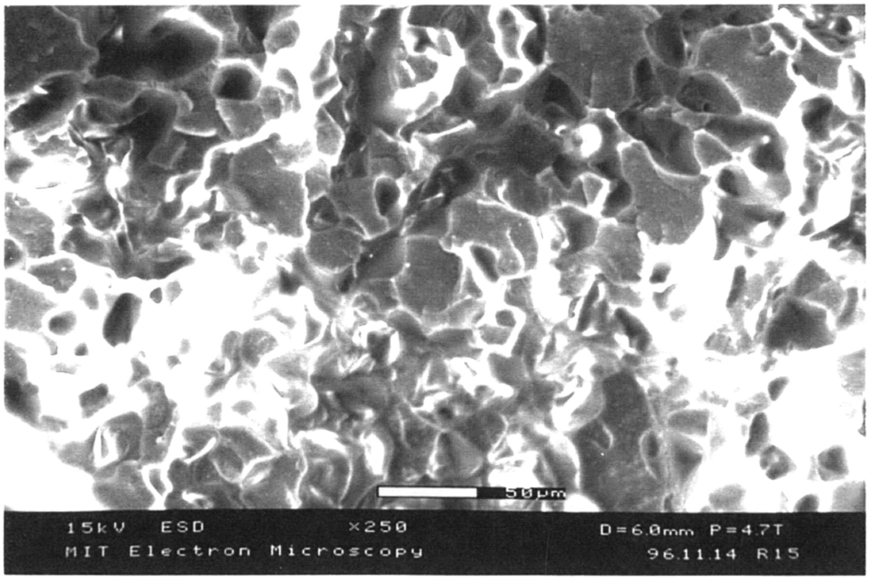

Figure 8.6 SEM micrograph of PP filament extruded through 0.03125"ϕ, 0.300"L die with nitrogen injection.

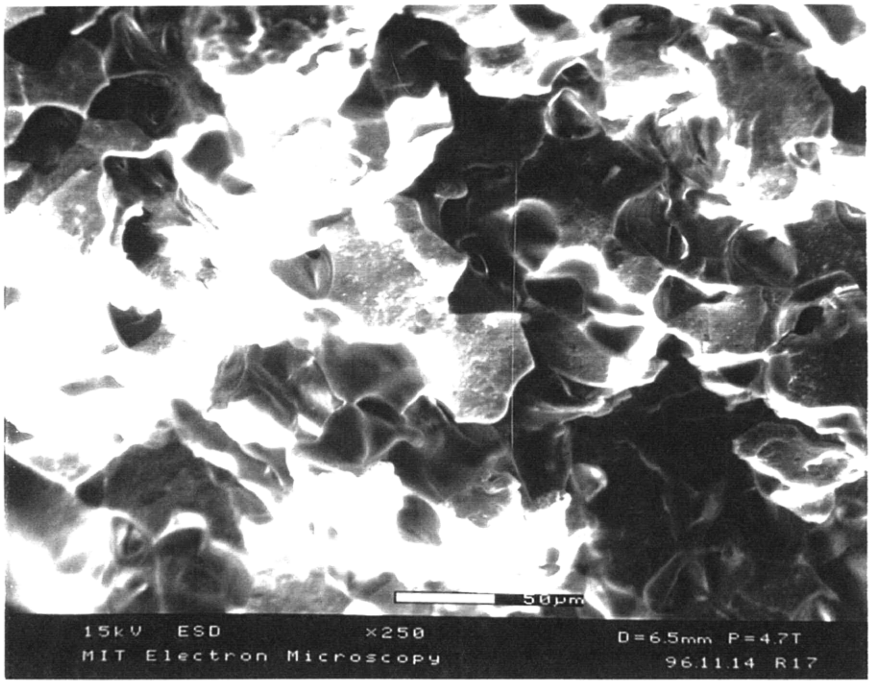

Figure 8.7 SEM micrograph of PP filament extruded through 0.03125"ϕ, 0.400"L die with nitrogen injection.

Effect of Die Temperature

After the effect of die geometry has been studied for the 0.03125”φ die set one can now study the effects of die temperature on the extrusion conditions and foam density. Table 8.3 records the experimental conditions and results of varying the die temperature from 375°F down to 310°F. Figure 8.8 shows the variation in volumetric flow rate with change in die temperature. Figure 8.9 shows that the nozzle pressure increases appreciably with reduction in die temperature while the adapter pressure and gas injection pressure are not as strongly affected. Pressure drop rate through the die shows a gradual rise with decrease in die temperature in Figure 8.10 while average density reaches a minimum at 335°F in Figure 8.11. The theoretical prediction again seems to qualitatively follow the experimental results. Figure 8.12 compares the actual and predicted effects of die temperature change on cell size.

Figures 8.13, 8.14, and 8.15 show some micrographs for this set of experiments.

0.03125”φ, 0.500”L Die

Resin	Quantum PP1610PF				
Gas	Nitrogen				
Extruder rpms	Wayne: 70				
	Royle: 25				
Temperature Settings					
	Wayne	Zone 1: 350°F	Royle	Zone 1: 375°F	Head Flange: 375°F
		Zone 2: 375°F		Zone 2: 375°F	Nozzle/Die: As noted
		Zone 3: 375°F		Zone 3: 375°F	
		Zone 4: 375°F		Zone 4: 375°F	
		Adapter: 225°F		Zone 5: 375°F	

Nozzle Temp. [°F]	Gas Injection Pressure [psi]	Adapter Pressure [psi]	Nozzle Pressure [psi]	Average Density [g/cc]	Average Mass Flow Rate [g/cc]	Volume Flow Rate [cc/min]	ΔP/Δt [10^6 psi/s]
375	1800	1750	2450	0.63	34.2	54.5	0.354
350	1900	1900	2650	0.59	34.5	58.6	0.412
335	2000	2000	2950	0.56	35.2	62.8	0.491
320	2100	2000	3050	0.61	32.8	53.5	0.433
310	2100	2300	3450	0.61	32.5	53.5	0.490

Table 8.3 Experimental conditions and data for the 0.03125”φ, 0.500"L die with nitrogen injection.

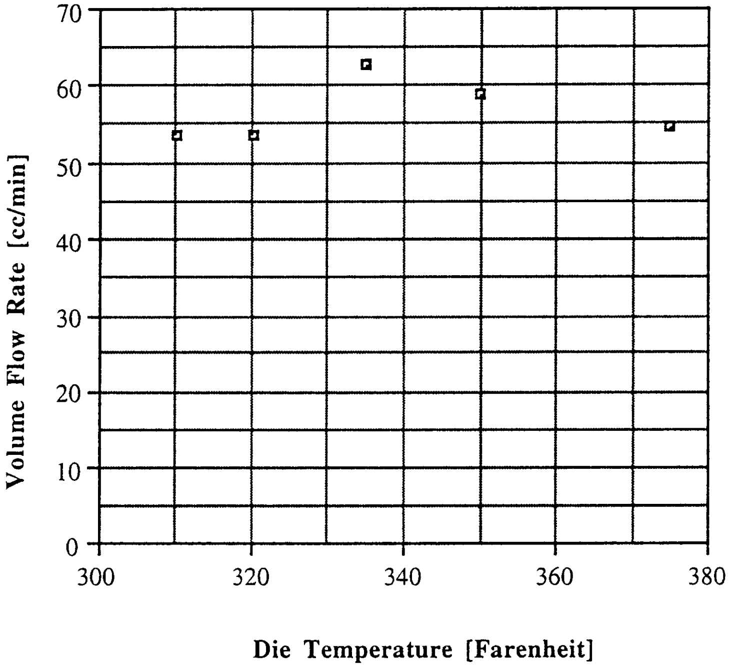

Figure 8.8 Plot of flow rate versus die temperature for the 0.03125"ϕ, 0.500"L die with PP and nitrogen injection.

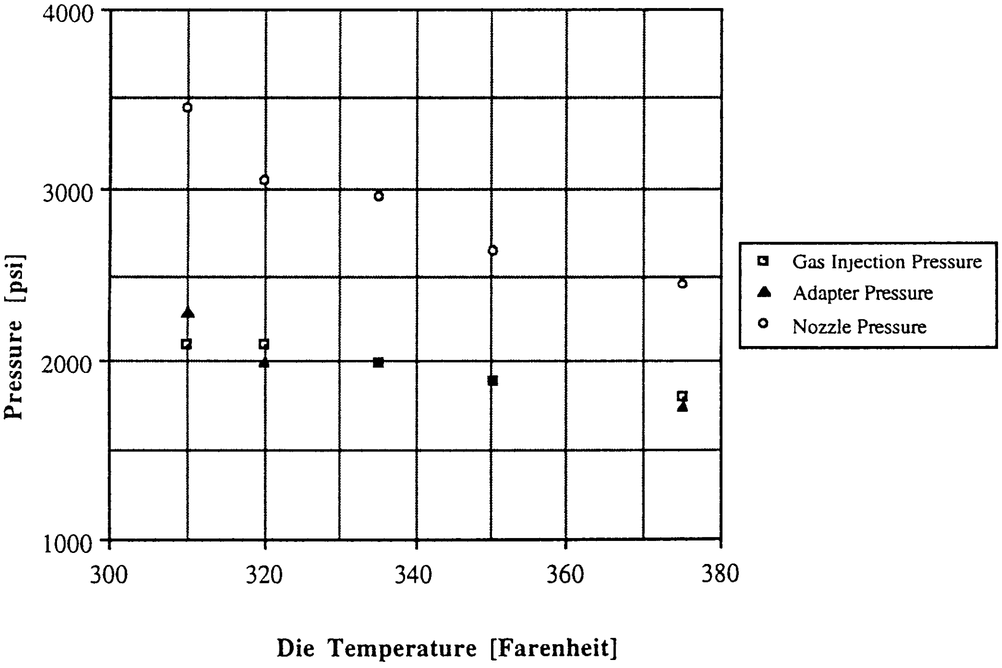

Figure 8.9 Plot of processing pressures versus die temperature for the 0.03125"ϕ, 0.500"L die with PP and nitrogen injection.

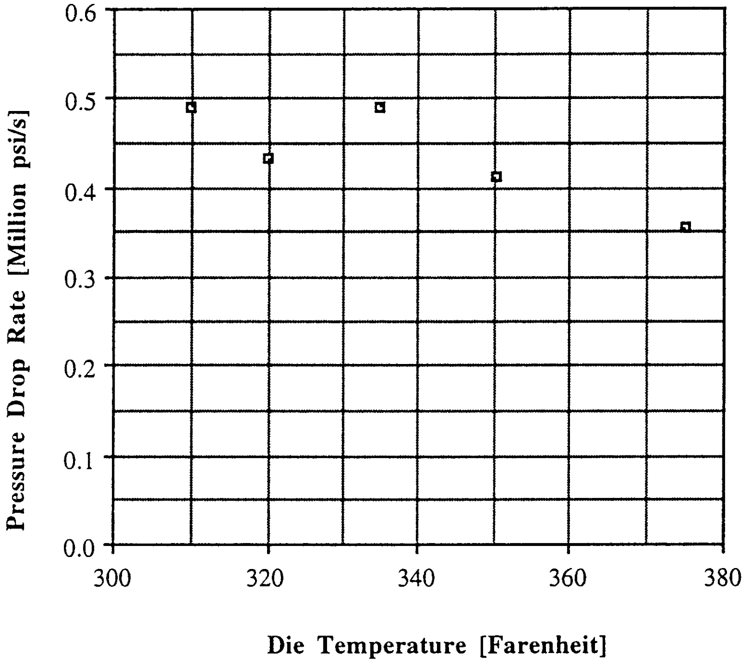

Figure 8.10 Plot of approximate pressure drop rate ($\Delta P/\Delta t$) versus die temperature for the 0.03125"ϕ, 0.500"L die with PP and nitrogen injection.

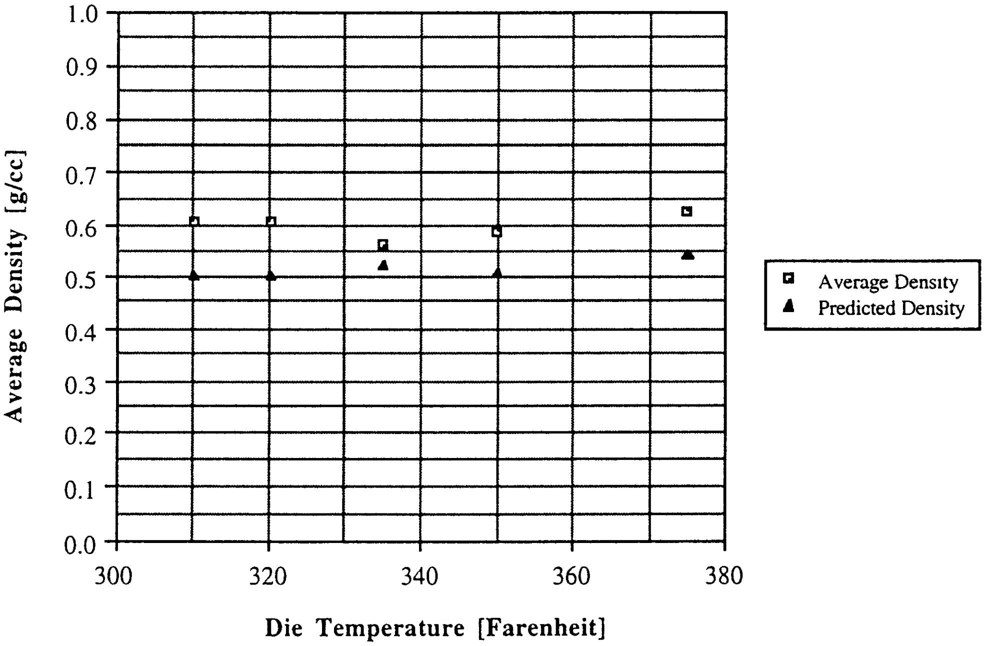

Figure 8.11 Plot of average foam density versus die temperature for the 0.03125"ϕ, 0.500"L die with nitrogen injection.

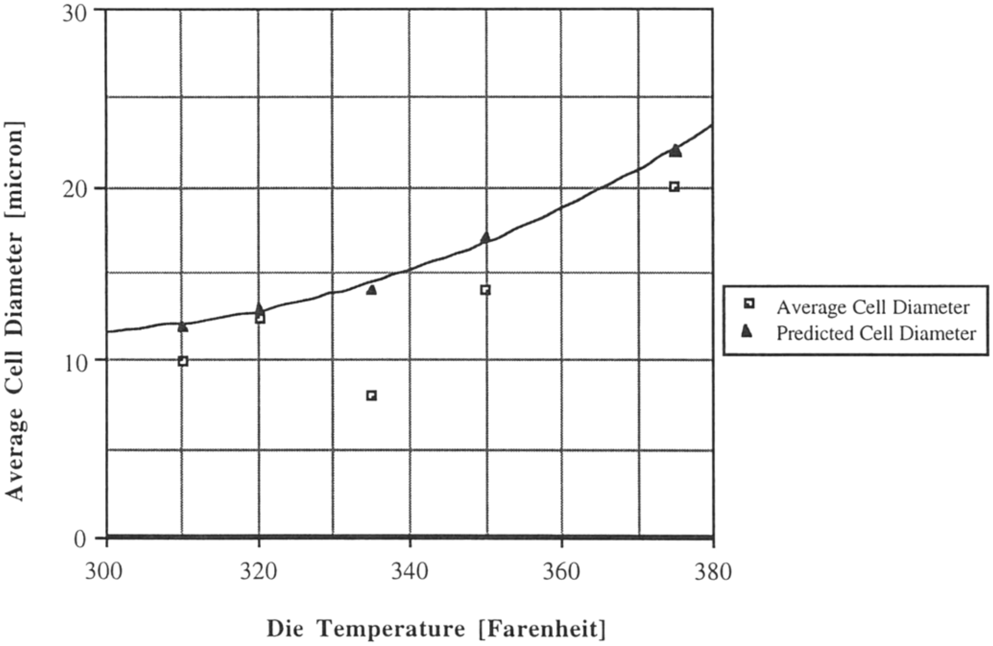

Figure 8.12 Plot of experimental and theoretically predicted average cell size versus die temperature for the 0.03125"ϕ, 0.500"L die with PP and nitrogen injection.

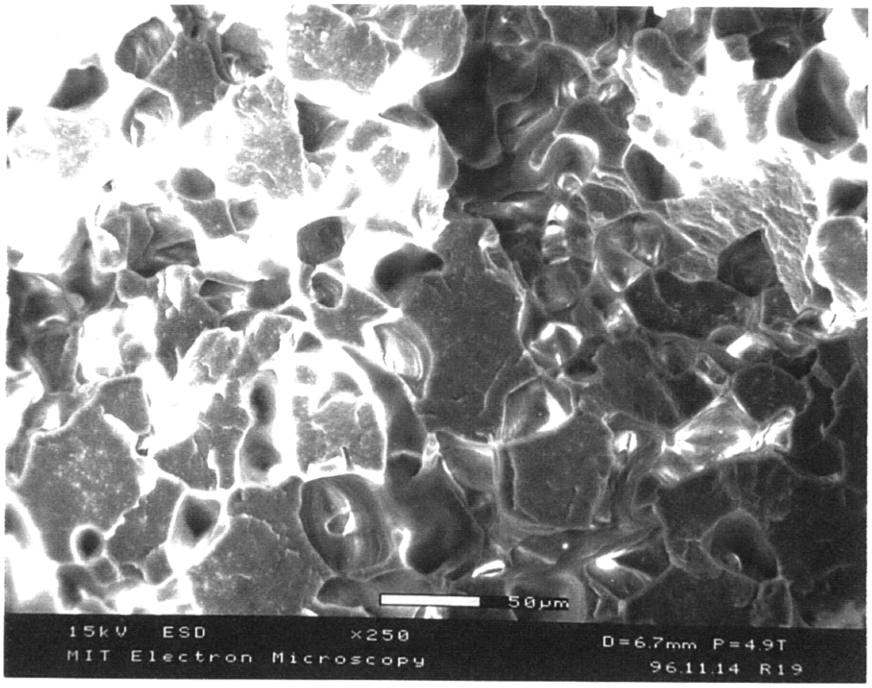

Figure 8.13 SEM micrograph of PP filament extruded though 0.03125"ϕ, 0.500"L with T_{die}=350°F and nitrogen injection.

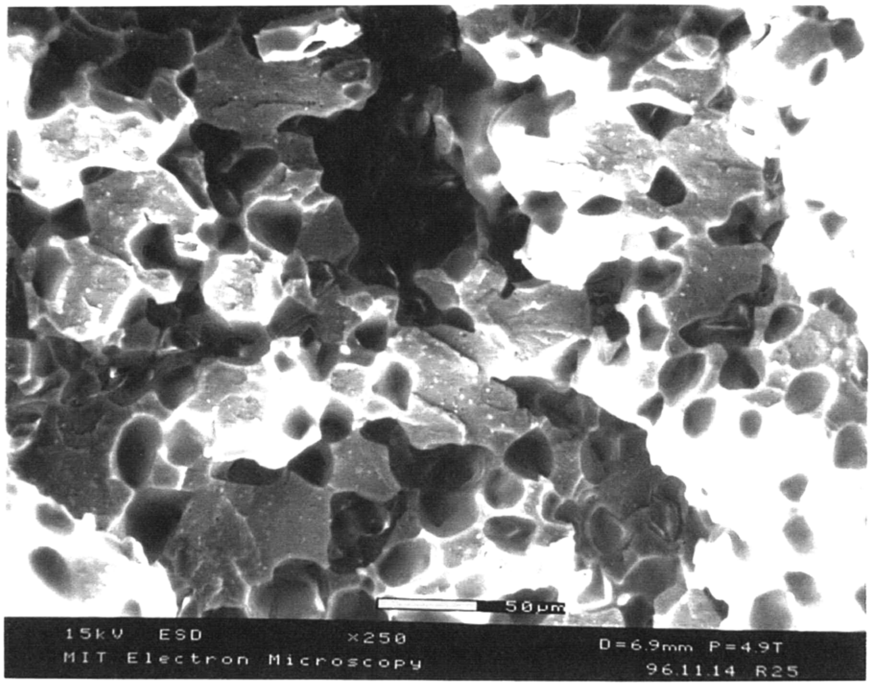

Figure 8.14 SEM micrograph of PP filament extruded though 0.03125" ϕ, 0.500" L with T_{die}=335°F and nitrogen injection.

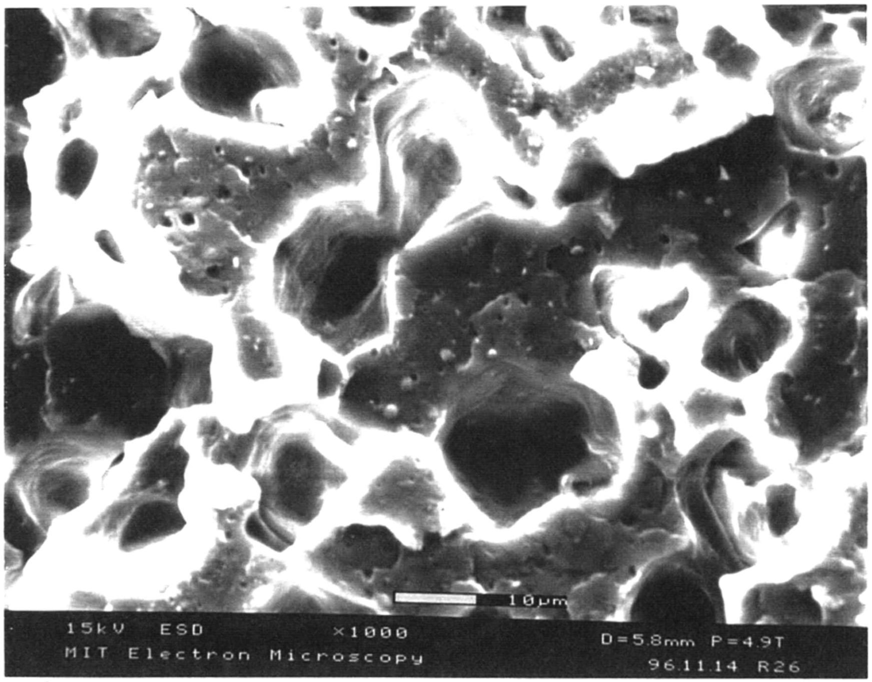

Figure 8.15 SEM micrograph of PP filament extruded though 0.03125" ϕ, 0.500" L with T_{die}=310°F and nitrogen injection.

8.2.2 Experiments with the 0.020"ϕ die set with PP and N_2 injection

Effect of Die Geometry

The third set of experiments was conducted with the set of dies having a diameter of 0.020". Experimental conditions and results are noted in Table 8.4 while Figures 8.15, 8.16, 8.17, 8.18, and 8.19 represent these results graphically. As in the case of the 1/32"ϕ die, the extruder rpms were set at fixed values and the nozzle/die pressure and adapter pressure were measured on line. Gas injection pressure was adjusted to get desired mass flow rates of nitrogen. Density and flow rates were measured as described in Section 8.11.

It is seen from Figure 8.15 that unlike in the case of the 0.03125"ϕ die, the flow rate decreases significantly. A decrease of about 15cc/min was noticed over the entire L/D range. Figure 8.16 indicates the upward trend the nozzle pressure follows with increase in L/D ratio. The pressure drop rate, as seen in Figure 8.17, is also much higher than the former case although the pressure drop rate decreases much more rapidly with increase in L/D ratio. Figure 8.18 shows that the average foam density does not change appreciably and is around 0.7 g/cc. Figure 8.19 shows the actual and predicted cell size variation with L/D ratio. Figures 8.21,8.22, and 8.23 show micrographs of some samples from this set.

0.020"ϕ Dies

Resin: Quantum PP1610PF
Gas: Nitrogen
Extruder rpms: Wayne: 70
Royle: 25

Temperature Settings

Wayne	Zone 1: 350°F	Royle	Zone 1: 375°F	Head Flange: 375°F
	Zone 2: 375°F		Zone 2: 375°F	Nozzle/Die: 375°F
	Zone 3: 375°F		Zone 3: 375°F	
	Zone 4: 375°F		Zone 4: 375°F	
	Adapter: 225°F		Zone 5: 375°F	

L. [inch]	L/D	Gas Injection Pressure [psi]	Adapter Pressure [psi]	Nozzle Pressure [psi]	Average Density [g/cc]	Average Mass Flow Rate [g/cc]	Volume Flow Rate [cc/min]	ΔP/Δt [10^6 psi/s]
0.050	2.5	1700	1900	2575	0.70	35.6	50.9	8.48
0.100	5.0	1900	1800	2875	0.70	35.1	50.2	4.67
0.150	7.5	2000	2000	3000	0.70	33.3	48.0	3.11
0.200	10.0	2200	2100	3350	0.69	32.8	47.7	2.59
0.250	12.5	2300	2200	3650	0.70	32.0	46.0	2.17
0.300	15.0	2300	2200	3550	0.70	31.9	45.4	1.74
0.350	17.5	2400	2300	3750	0.68	29.4	43.2	1.50
0.400	20.0	2500	2400	3700	0.70	30.4	43.3	1.30
0.450	22.5	2500	2500	4000	0.70	29.6	42.1	1.21
0.500	25.0	3000	2950	4550	0.69	26.4	38.4	1.13

Table 8.4 Experimental conditions and data for the 0.020"ϕ die set with nitrogen injection.

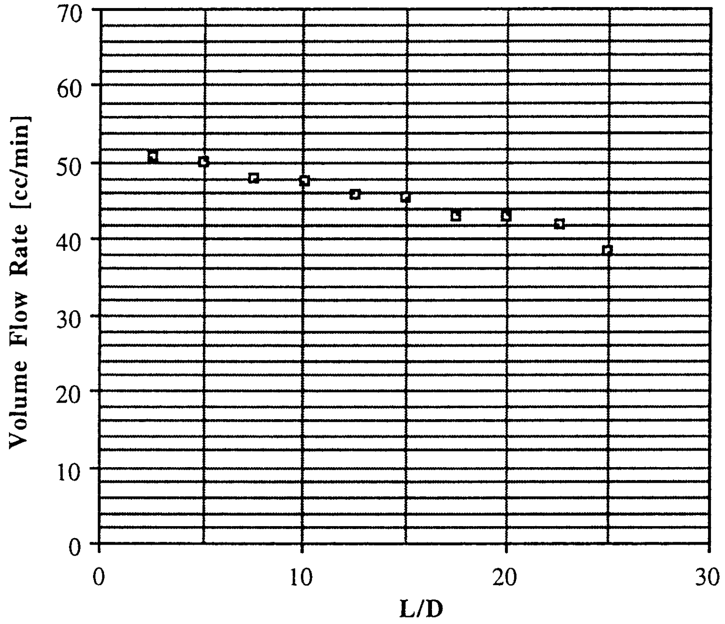

Figure 8.16 Plot of flow rate versus die L/D ratio for the 0.020" ϕ die set with PP and nitrogen injection.

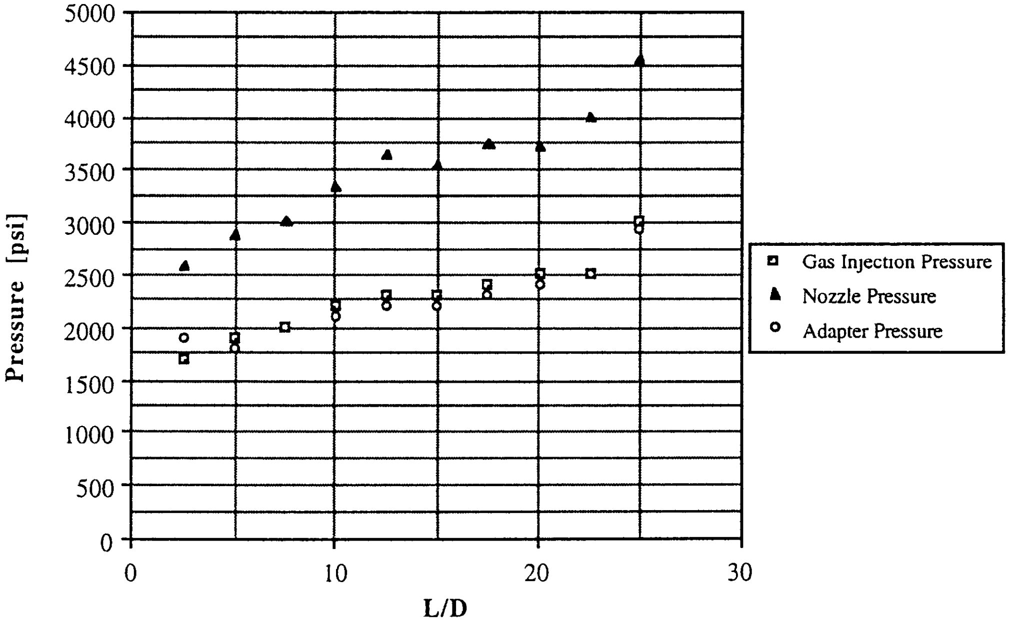

Figure 8.17 Plot of processing pressures versus die L/D ratio for the 0.020" ϕ die set with PP and nitrogen injection.

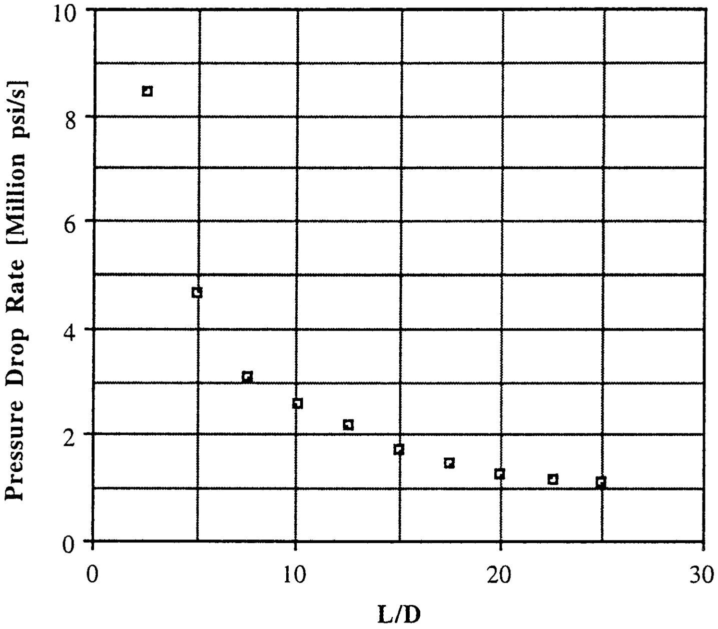

Figure 8.18 Plot of approximate pressure drop rate ($\Delta P/\Delta t$) versus die L/D ratio for the 0.020"ϕ die set with PP and nitrogen injection.

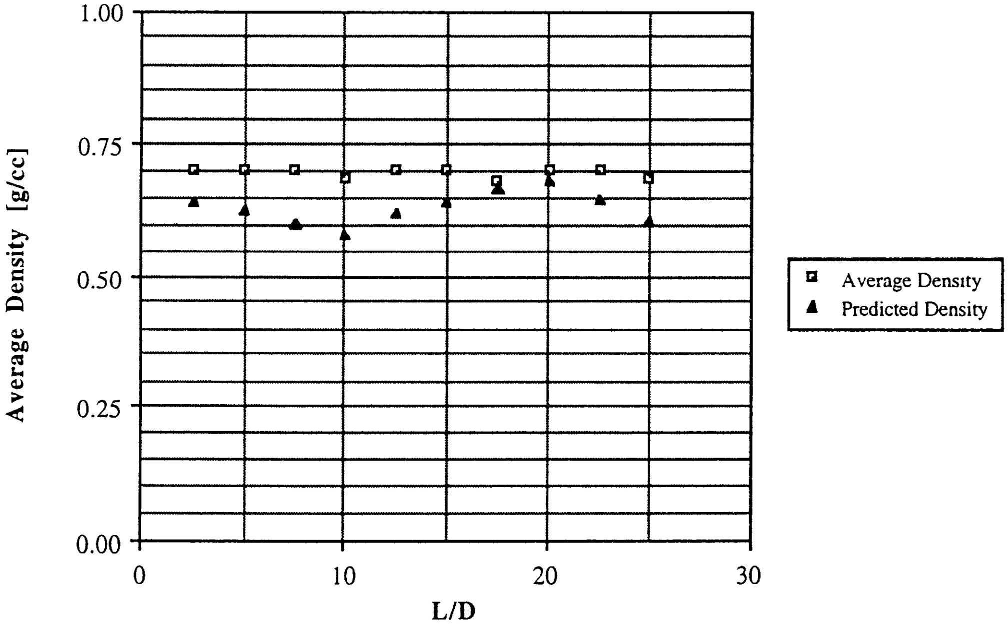

Figure 8.19 Plot of average foam density versus die L/D ratio for the 0.020"ϕ die set with PP and nitrogen injection.

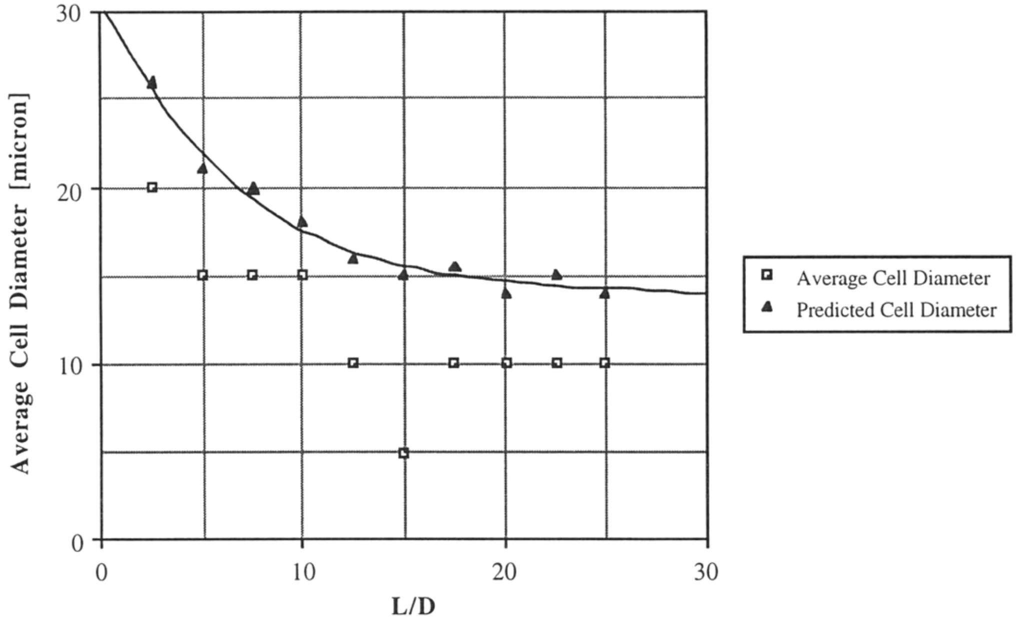

Figure 8.20 Plot of experimental and theoretically predicted average cell size versus L/D ratio for the 0.020"ϕ die set with PP and nitrogen injection.

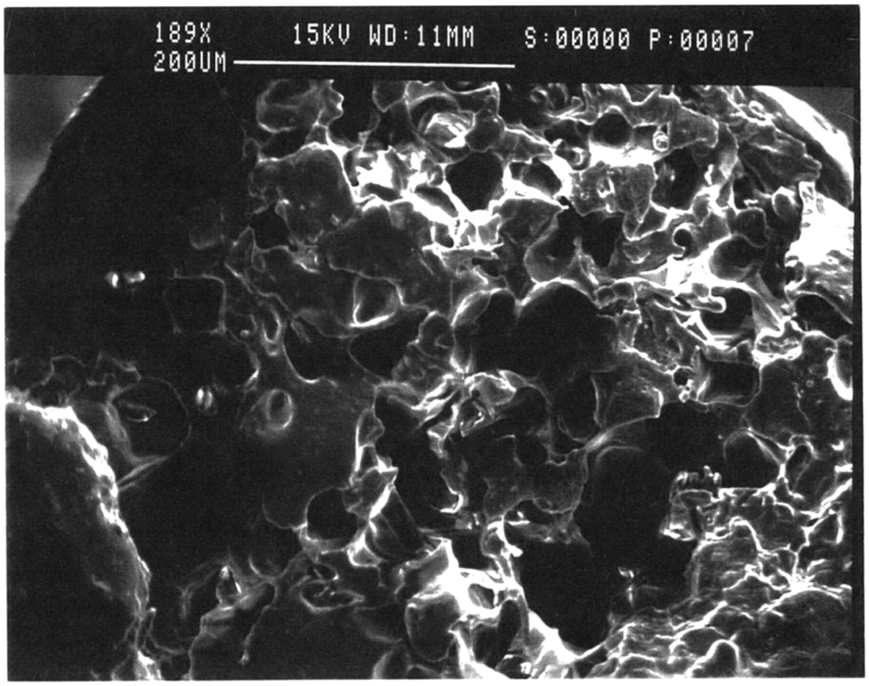

Figure 8.21 SEM micrograph of PP filament extruded through 0.020"ϕ, 0.100"L die with nitrogen injection.

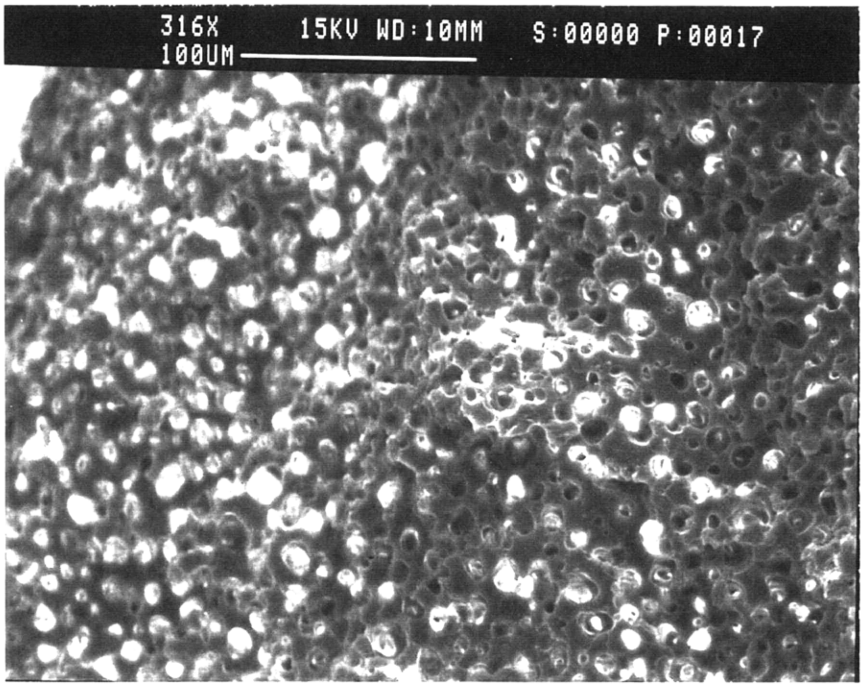

Figure 8.22 SEM micrograph of PP filament extruded through 0.020"ϕ, 0.500"L die with nitrogen injection.

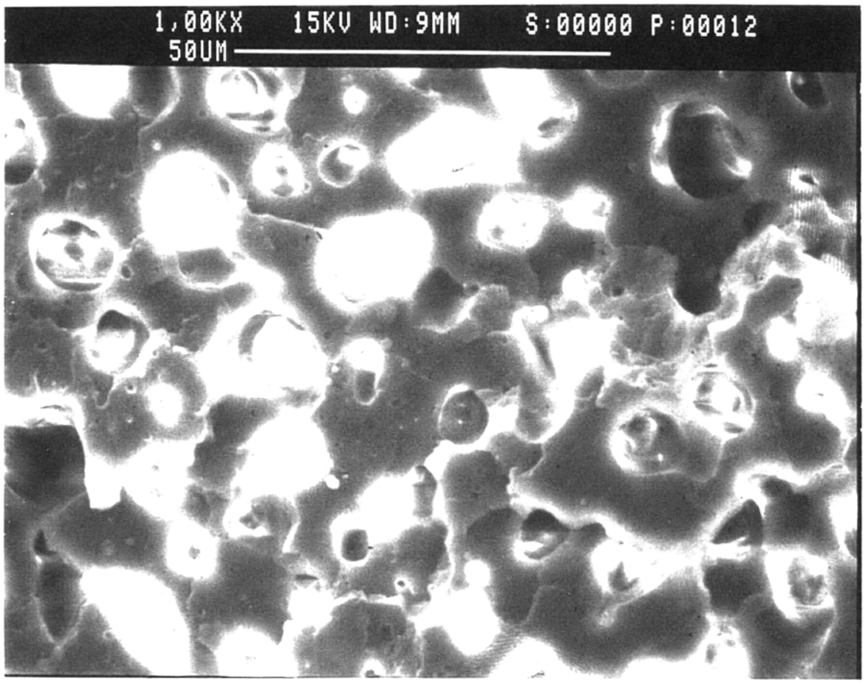

Figure 8.23 SEM micrograph of PP filament extruded through 0.020"ϕ, 0.300"L die with nitrogen injection.

Effect of Die Temperature

Table 8.5 shows the experimental conditions and results for the set of experiments performed to ascertain the effect of die temperature for the case of the 0.020"ϕ, 500" length die.

0.020"ϕ, 0.500"L Die

Resin	Quantum PP1610PF
Gas	Nitrogen
Extruder rpms	Wayne: 70 Royle: 25

Temperature Settings						
	Wayne	Zone 1: 350°F	Royle	Zone 1: 375°F	Head Flange:	375°F
		Zone 2: 375°F		Zone 2: 375°F	Nozzle/Die:	As noted
		Zone 3: 375°F		Zone 3: 375°F		
		Zone 4: 375°F		Zone 4: 375°F		
		Adapter: 225°F		Zone 5: 375°F		

Nozzle Temp. [°F]	Gas Injection Pressure [psi]	Adapter Pressure [psi]	Nozzle Pressure [psi]	Average Density [g/cc]	Average Mass Flow Rate [g/cc]	Volume Flow Rate [cc/min]	$\Delta P/\Delta t$ [10^6 psi/s]
375	3000	2950	4550	0.69	26.4	38.4	1.13
350	3000	2975	4650	0.68	26.9	39.7	1.20
335	3200	3200	4950	0.64	25.5	39.8	1.28

Table 8.5 Experimental conditions and data for the 0.020"ϕ, 0.500"L die with nitrogen injection.

Figures 8.24, 8.25, 8.26, 8.27, and 8.28 represent the results graphically. Figures 8.28 and 8.29 show some micrographs from this set of experiments which clearly show the effect of die temperature on cell microstructure. From Figure 8.24 it is seen that lowering the die temperature from 375°F to 335°F has very little effect on the volume flow rate. Figure 8.25 shows that the nozzle/die pressure also seems to be insensitive to die temperature effects although a significant pressure difference of about 2000psi is observed between the nozzle pressure and adapter pressure throughout the entire range of die temperature. The pressure drop rate does show some sensitivity to change in die temperature as an increase is observed with decrease in die temperature.

The foam microstructure is seen to depend on die temperature as is evident from Figures 8.27 and 8.28. The foam density decreases slightly when the die temperature is reduced while the average (experimentally obtained) cell diameter drops from 10 microns to about 8 microns. As seen previously, the analytical prediction of the die temperature effects on microstructure follow the experimental results qualitatively although the foam density estimates are lower than the experimental values while the cell size predictions are consistently larger than the experimentally obtained ones.

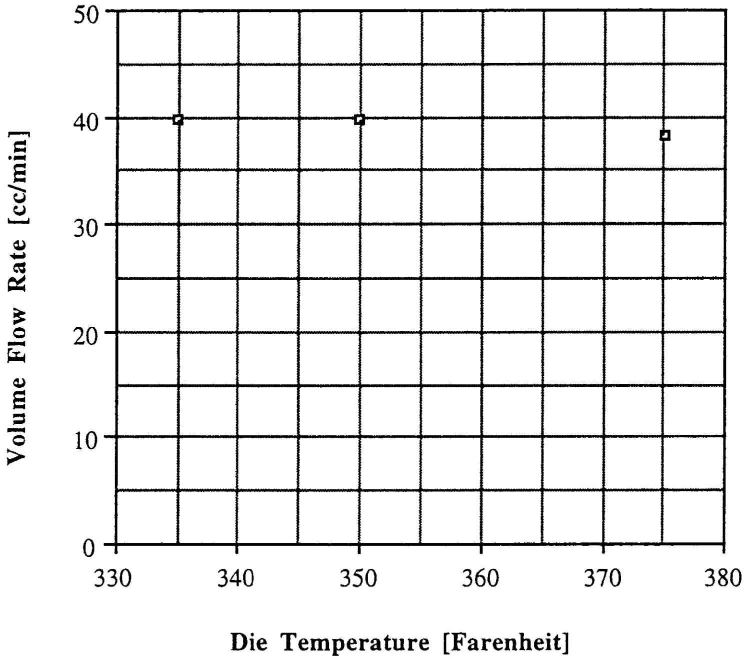

Figure 8.24 Plot of flow rate versus die temperature for the 0.020"ϕ, 0.500"L die with PP and nitrogen injection.

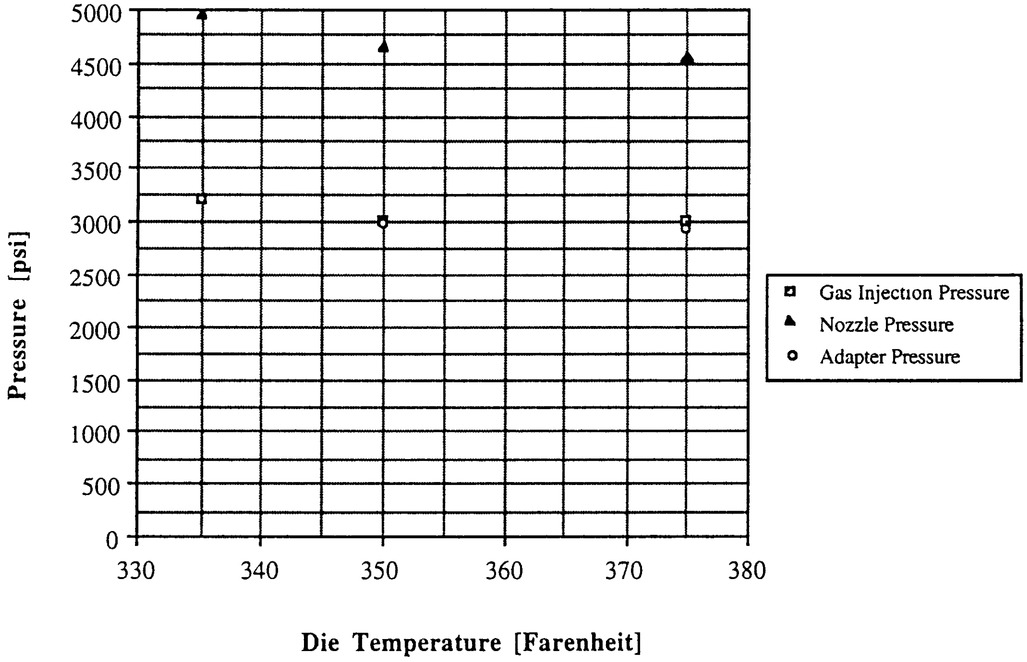

Figure 8.25 Plot of processing pressures versus die temperature for the 0.020"ϕ, 0.500"L die with PP and nitrogen injection.

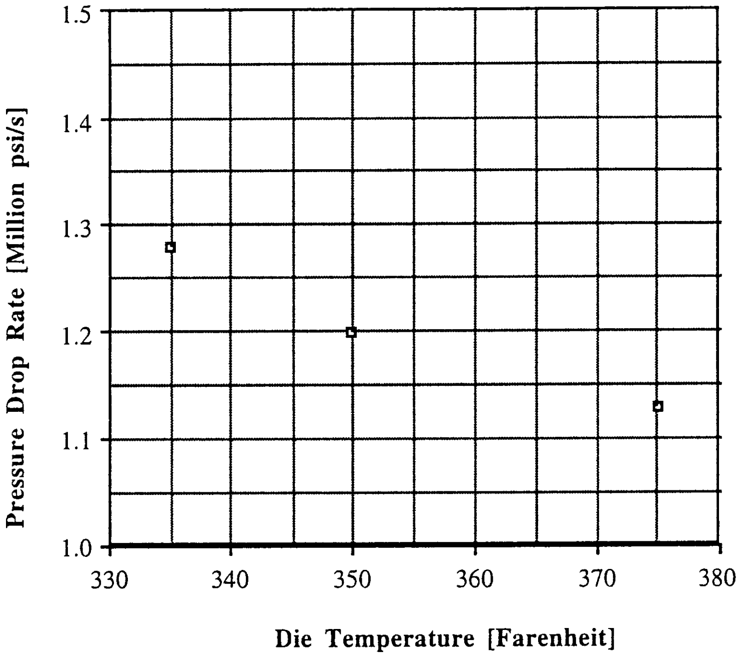

Figure 8.26 Plot of approximate pressure drop rate ($\Delta P/\Delta t$) versus die temperature for the 0.020"ϕ, 0.500"L die with PP and nitrogen injection.

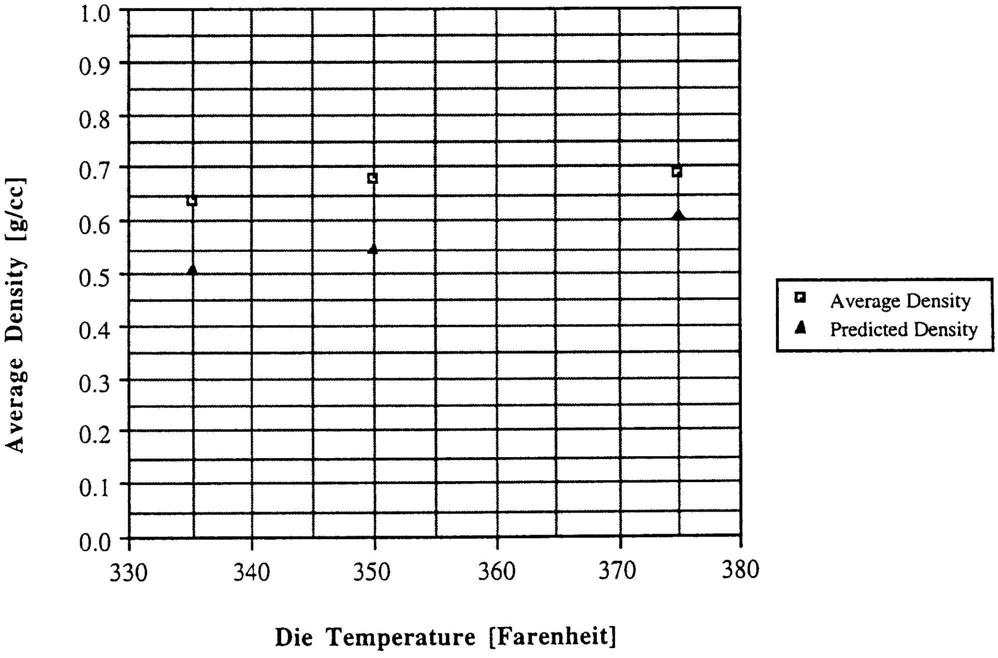

Figure 8.27 Plot of average foam density versus die temperature for the 0.020"ϕ, 0.500"L die with PP and nitrogen injection.

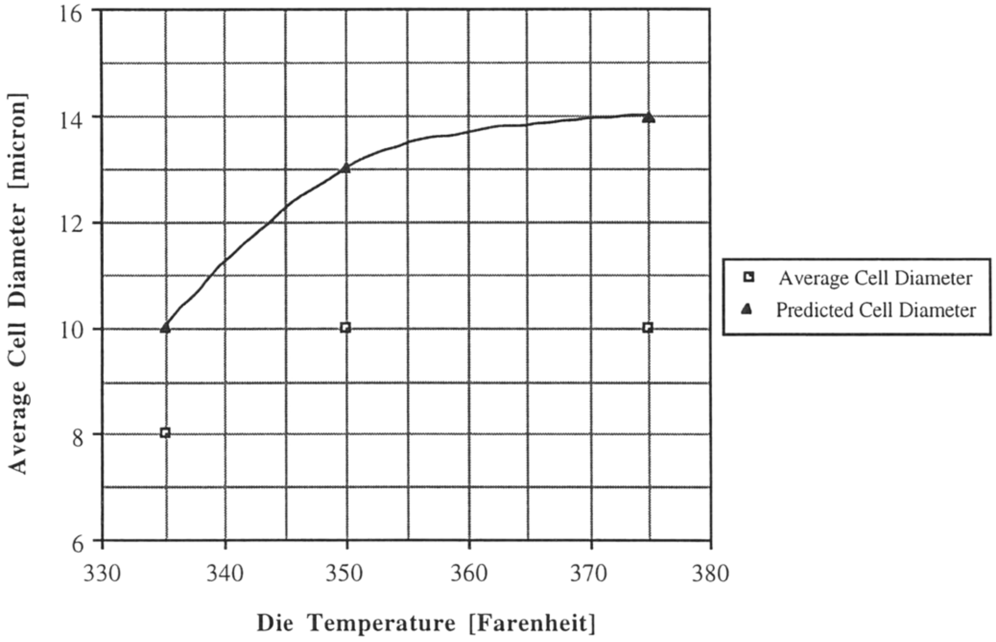

Figure 8.28 Plot of experimental and theoretically predicted average cell size versus die temperature for the 0.020"ϕ, 0.500"L die with PP and nitrogen injection.

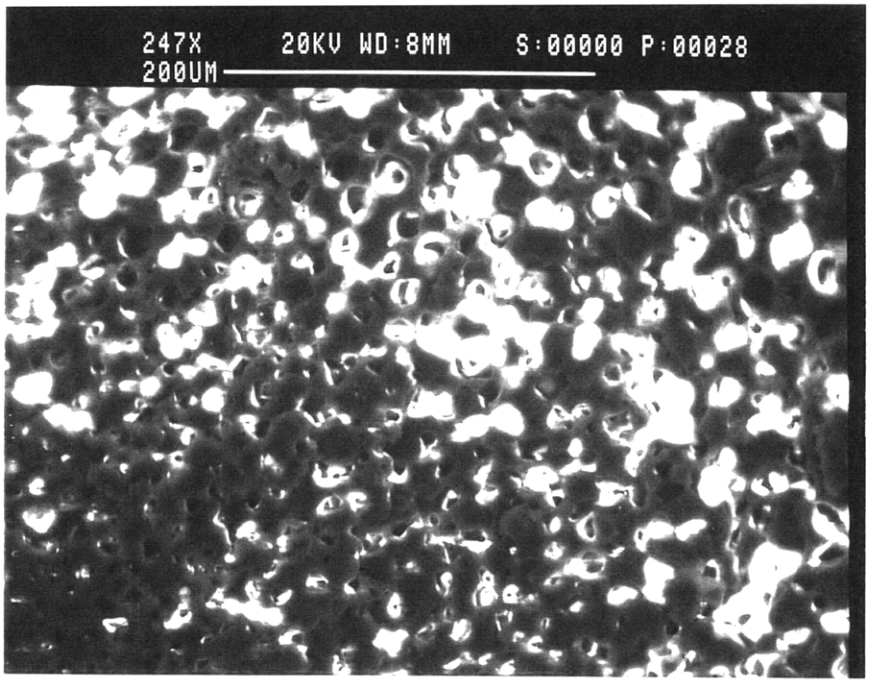

Figure 8.29 SEM micrograph of PP filament extruded through 0.020"ϕ, 0.500"L die with T_{die}=320°F and nitrogen injection.

8.2.3 Experiments with the 0.03125”ϕ die set with PP and CO_2 injection

After completion of the experiments using nitrogen the next step was the injection of carbon dioxide using the same set of nozzles. Such a set of experiments would be extremely useful in understanding the effect that different types of gas would have on the foaming process and how the final microstructure would be affected. The set of dies of 0.03125” diameter was used for experiments to study the effects of carbon dioxide injection into the melt . Table 8.6 lists the conditions and results of the experiments. Figures 8.30, 8.31, 8.32, 8.33, and 8.34 depict the results graphically.

As seen from Figure 8.30 an increase in L/D ratio of the die results in an increase in a gentle increase in the flow rate. This probably indicates that due to the increased nozzle pressure (which is assumed to be the saturation pressure), higher quantities of gas are dissolved in the polymer resulting in lower viscosity. Thus, although the die restriction increases with higher L/D ratio, the effect of significant viscosity reduction causes the flow rate to increase slightly. This scenario is different from the case where nitrogen was used where the flow rate was almost insensitive to die L/D change.

Figure 8.31 shows that all the processing pressures increase with increase in L/D ratio. One very important observation is that unlike the case of nitrogen injection, the nozzle/die pressure is seen to be lower than the adapter and gas injection pressures. This can again be attributed to the drastic reduction in viscosity that follows carbon dioxide injection into the polymer melt. Figure 8.32 indicates that the pressure drop rate shows a gradual decreasing

0.03125”ϕ Dies

Resin	Quantum PP1610PF
Gas	Carbon Dioxide
Extruder rpms	Wayne: 70
	Royle: 25

Temperature Settings

Wayne	Zone 1: 350°F	Royle	Zone 1: 375°F	Head Flange:	375°F
	Zone 2: 375°F		Zone 2: 375°F	Nozzle/Die:	375°F
	Zone 3: 375°F		Zone 3: 375°F		
	Zone 4: 375°F		Zone 4: 375°F		
	Adapter: 225°F		Zone 5: 375°F		

L [inch]	L/D	Gas Injection Pressure [psi]	Adapter Pressure [psi]	Nozzle Pressure [psi]	Average Density [g/cc]	Average Mass Flow Rate [g/cc]	Volume Flow Rate [cc/min]	ΔP/Δt [10^6 psi/s]
0.100	3.2	1400	1300	1000	0.73	40.7	55.5	0.368
0.200	6.4	1500	1400	1150	0.71	39.7	56.3	0.430
0.300	9.6	1700	1600	1300	0.54	38.8	72.0	0.414
0.400	12.8	1700	1550	1375	0.62	37.4	60.6	0.276
0.500	16.0	1700	1575	1500	0.65	39.7	61.3	0.244

Table 8.6 Experimental conditions and data for the 0.03125”ϕ die set with carbon dioxide injection.

trend with increase in L/D ratio increase.

Figures 8.32 and 8.33 show the effects of die geometry on foam microstructure. It is seen from Figure 8.32 that the minimum foam density is obtained at an L/D ratio of 9.6 (die length of 0.3"). The theoretical prediction of the foam density again seems to be substantially lower than the experimental values although there is certainly the indication of a minimum density point. The variation in average cell size with change in die L/D ratio is evident from Figure 8.33. The average cell diameter in the case of carbon dioxide injection is smaller than that in the case of nitrogen injection, especially for the shorter dies of 0.200" and 0.100" length.

From an observation of the micrographs shown in Figures 8.34, 8.35 and 8.36 it is evident that the cell density for foams produced using injection of carbon dioxide is much higher than those produced by injection of nitrogen (for the same set of 0.03125"ϕ dies). This can be attributed to the higher solubility of carbon dioxide in polymers compared to nitrogen. The higher solubility leads to a higher initial mole fraction of carbon dioxide in the polymer/gas solution. This leads to a higher nucleation driving force and more nucleation sites.

The final size of the cells is slightly smaller in the case of carbon dioxide. However, the difference in cell size is not very pronounced. This because although the number of nucleation sites in the case of carbon dioxide is greater, the higher concentration (of gas) gradient at the beginning of the process between the bulk solution and the interface (of a critical cluster and the bulk solution) will lead to very high diffusion flux rates. This in turn will cause the cells to experience rapid growth. Thus, although the cell density is higher in the case of carbon dioxide, the final cell size is about the same for both gases. The theoretical model developed in Chapter 4 also shows similar predictions.

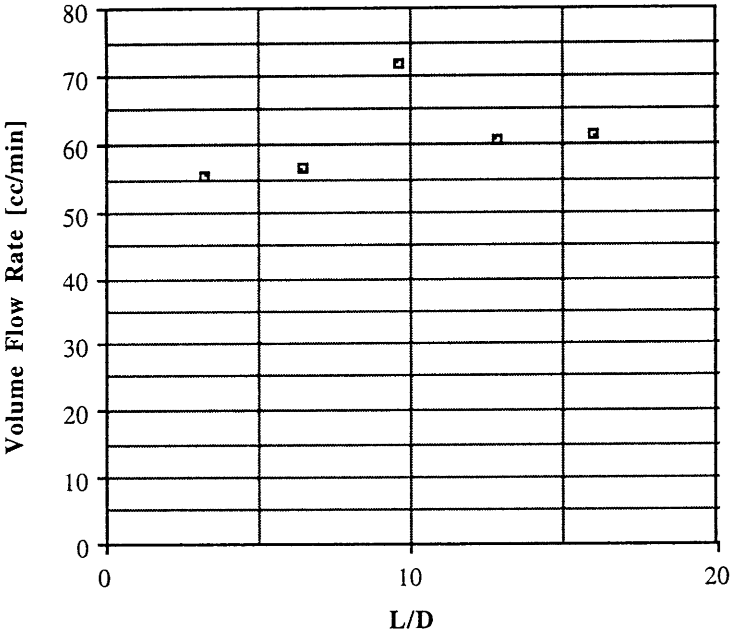

Figure 8.30 Plot of flow rate versus die L/D ratio for the 0.03125''"ϕ die set with PP and carbon dioxide injection.

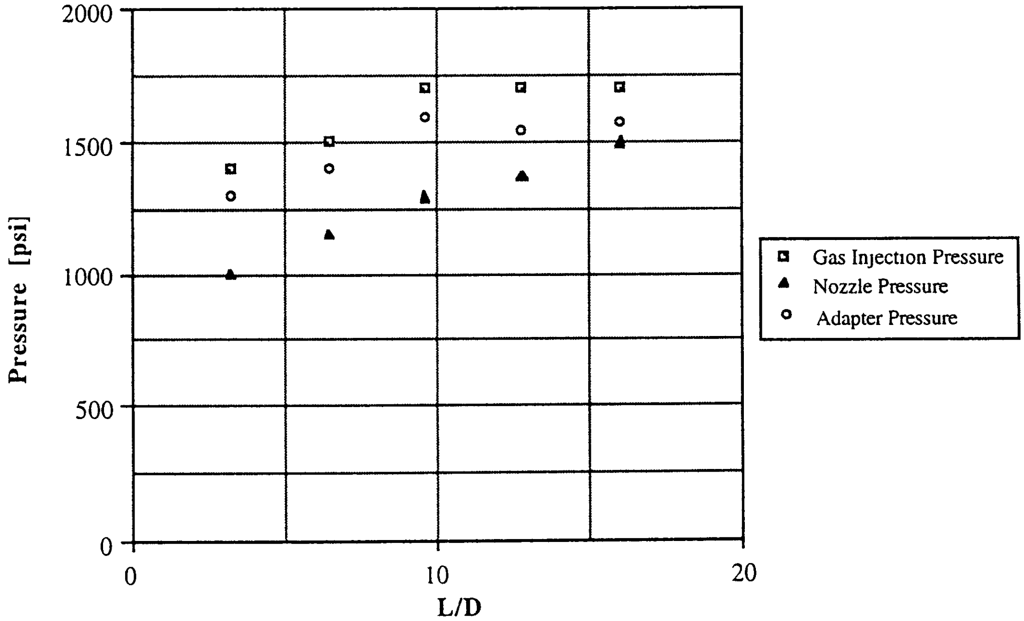

Figure 8.31 Plot of processing pressures versus die L/D ratio for the 0.03125"ϕ die set with PP and carbon dioxide injection.

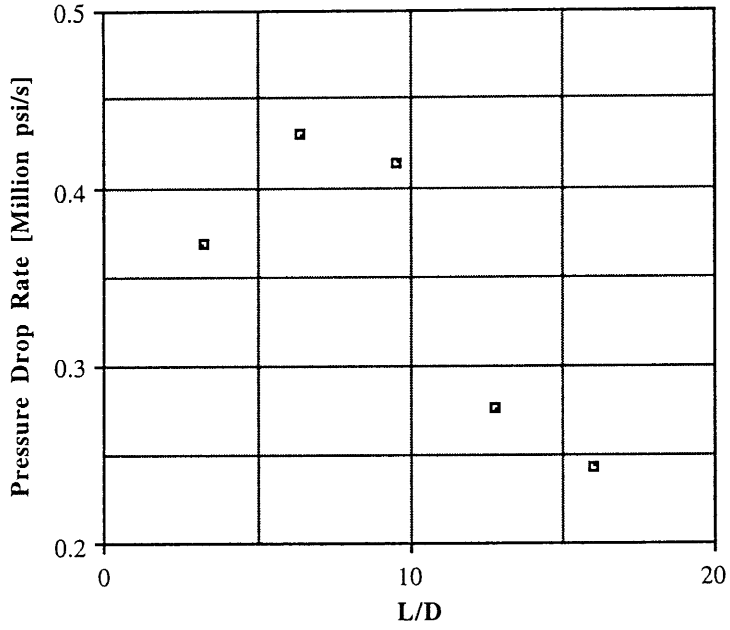

Figure 8.32 Plot of approximate pressure drop rate ($\Delta P/\Delta t$) versus die L/D ratio for the 0.03125"ϕ die set with PP and carbon dioxide injection.

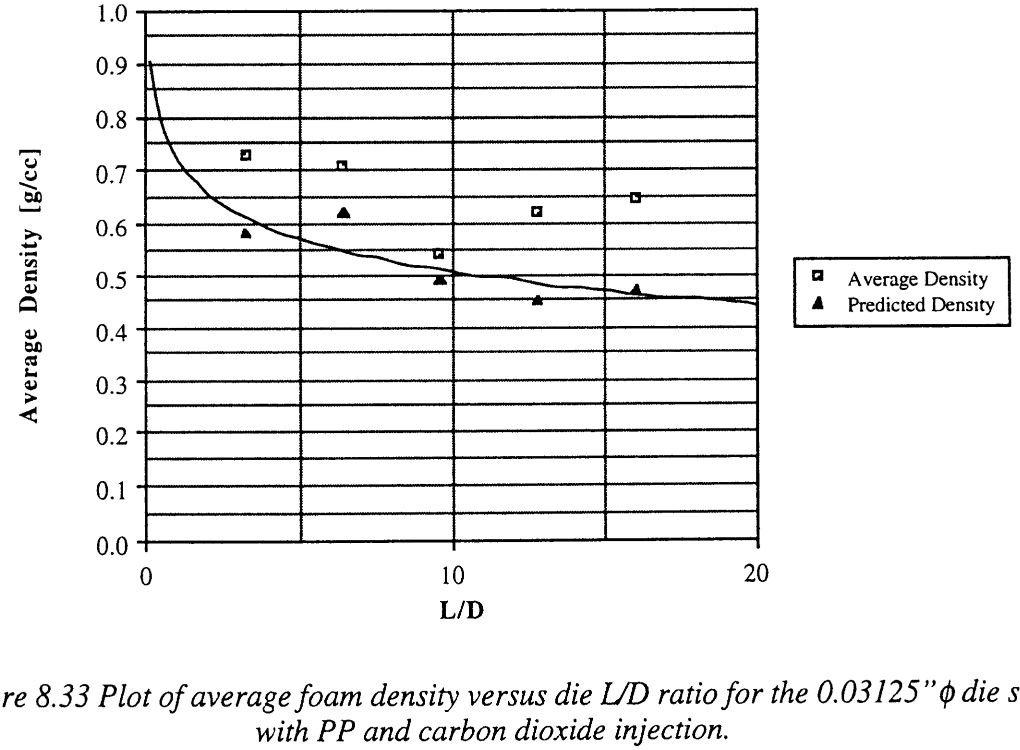

Figure 8.33 Plot of average foam density versus die L/D ratio for the 0.03125"ϕ die set with PP and carbon dioxide injection.

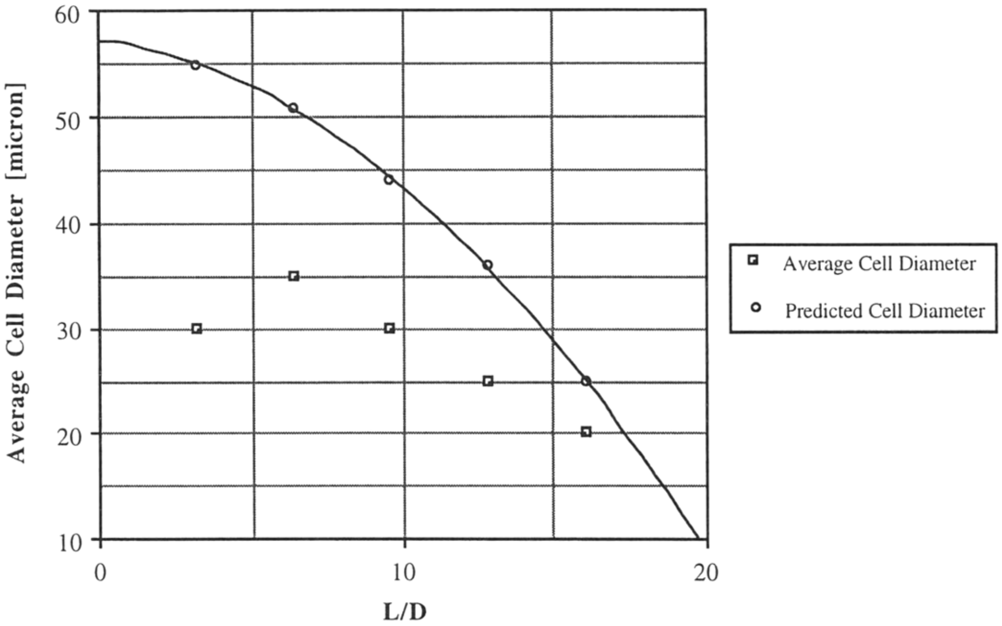

Figure 8.34 Plot of experimental and theoretically predicted average cell size for the 0.03125"ϕ die set with PP and carbon dioxide injection.

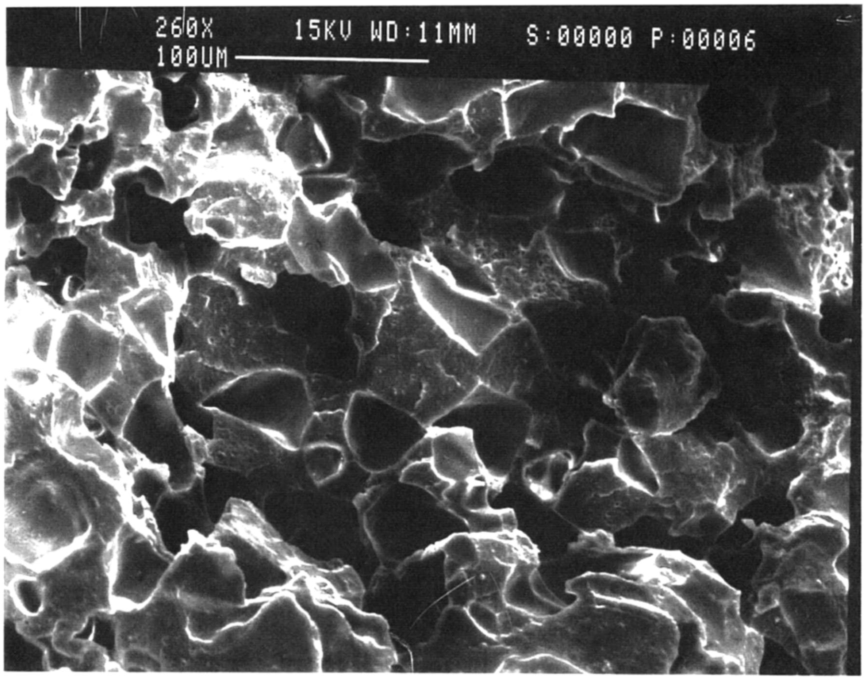

Figure 8.35 SEM micrograph of PP filament extruded through 0.03125"ϕ, 0.100"L die with carbon dioxide injection.

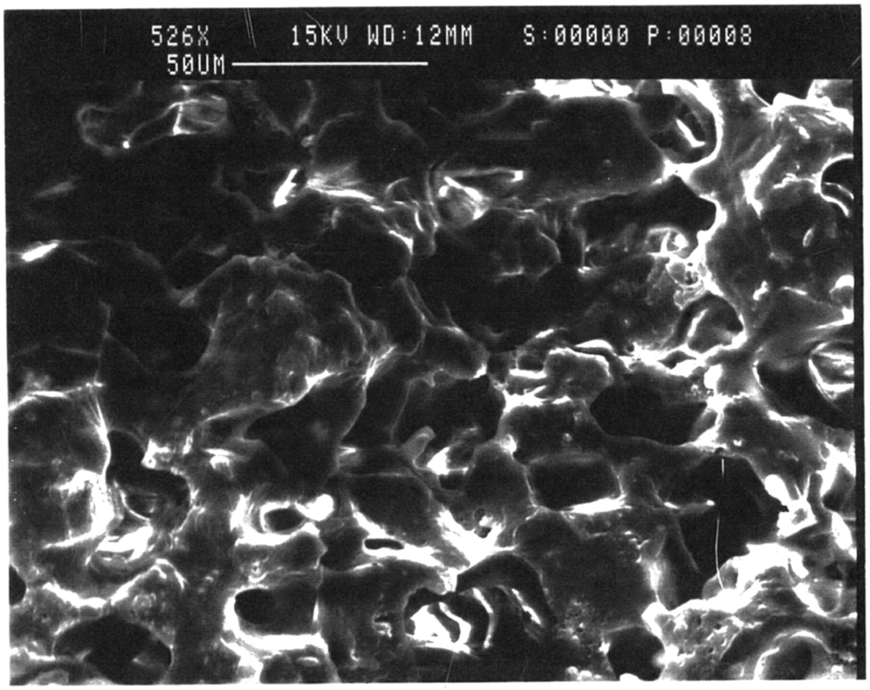

Figure 8.36 SEM micrograph of PP filament extruded through 0.03125"ϕ, 0.300"L die with carbon dioxide injection.

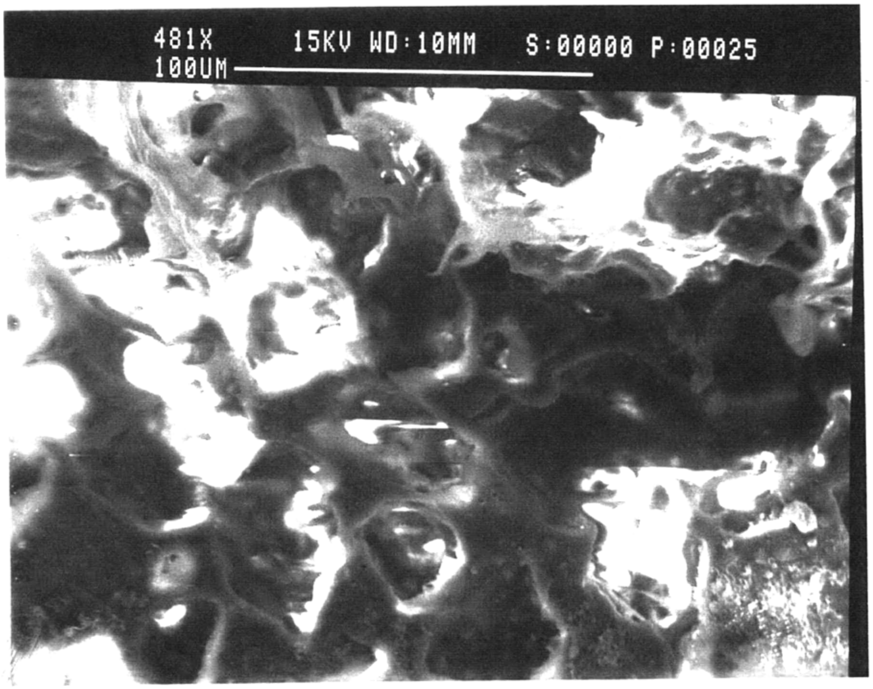

Figure 8.37 SEM micrograph of PP filament extruded through 0.03125"ϕ, 0.500"L die with carbon dioxide injection.

Effect of Die Temperature

After the effects of die geometry on extrusion of PP with carbon dioxide have been studied, it is essential to study the effects of die temperature change on extrusion. The die chosen for this set of experiments was the one with a diameter of 0.03125" and a length of 0.500". The die temperature was varied from 375°F to 335°F and its effects were noted. Table 8.6 shows the experimental conditions and results from varying die temperature when carbon dioxide is injected.

Figure 8.38 shows the relationship between volume flow rate and die temperature. The effect of lowering die temperature on flow rate is very pronounced with the flow rate doubling when the die temperature drops from 375°F to 335°F. This strong effect is not observed in the case of nitrogen injection.

In Figure 8.39, the various processing pressures are plotted versus the die temperature. The nozzle/die pressure rises with lowering of die temperature. Very little difference is observed between the adapter, gas injection and nozzle/die pressures. This is also in stark contrast to the case of nitrogen. Figure 8.40 shows that the pressure drop rate increases with decreasing die temperature.

In Figure 8.41, the effect of die temperature change on foam density is observed. The foam density drops dramatically with decrease in die temperature. The observed decrease is almost 50% for a temperature range of 40°F. As seen from Figure 8.42, there is no change in cell diameter with die temperature decrease although the prediction was for an increasing trend.

0.03125"ϕ, 0.500"L Die

Resin	Quantum PP1610PF
Gas	Carbon Dioxide
Extruder rpms	Wayne: 70
	Royle: 25

Temperature Settings

Wayne	Zone 1: 350°F	Royle	Zone 1: 375°F	Head Flange:	375°F
	Zone 2: 375°F		Zone 2: 375°F	Nozzle/Die:	As noted
	Zone 3: 375°F		Zone 3: 375°F		
	Zone 4: 375°F		Zone 4: 375°F		
	Adapter: 225°F		Zone 5: 375°F		

Nozzle Temp. [°F]	Gas Injection Pressure [psi]	Adapter Pressure [psi]	Nozzle Pressure [psi]	Average Density [g/cc]	Average Mass Flow Rate [g/cc]	Volume Flow Rate [cc/min]	$\Delta P/\Delta t$ [10^6 psi/s]
375	3000	2950	4550	0.69	26.4	38.4	1.13
350	3000	2975	4650	0.68	26.9	39.7	1.20
335	3200	3200	4950	0.64	25.5	39.8	1.28

Table 8.7 Experimental conditions and data for the 0.03125"ϕ, 0.500"L die with carbon dioxide injection.

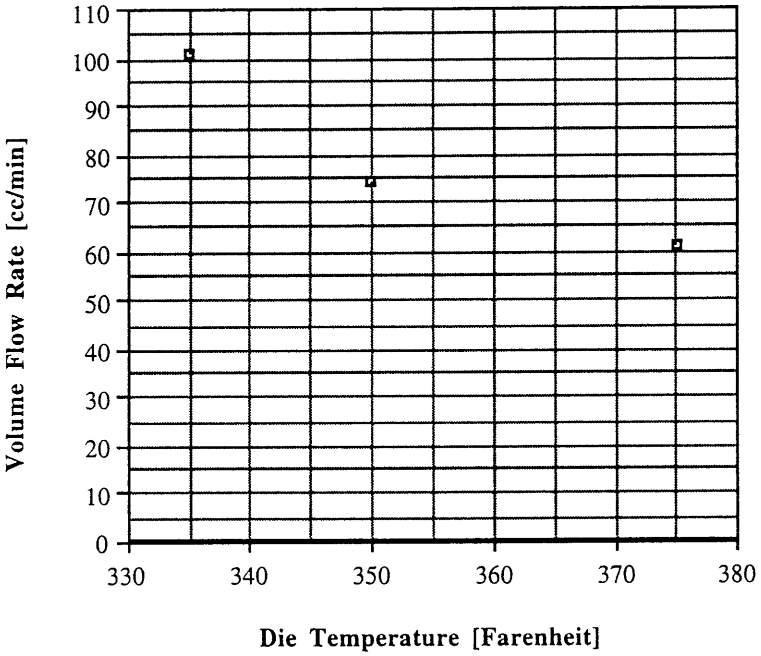

Figure 8.38 Plot of flow rate versus die temperature for the 0.03125"ϕ, 0.500"L die with PP and carbon dioxide injection.

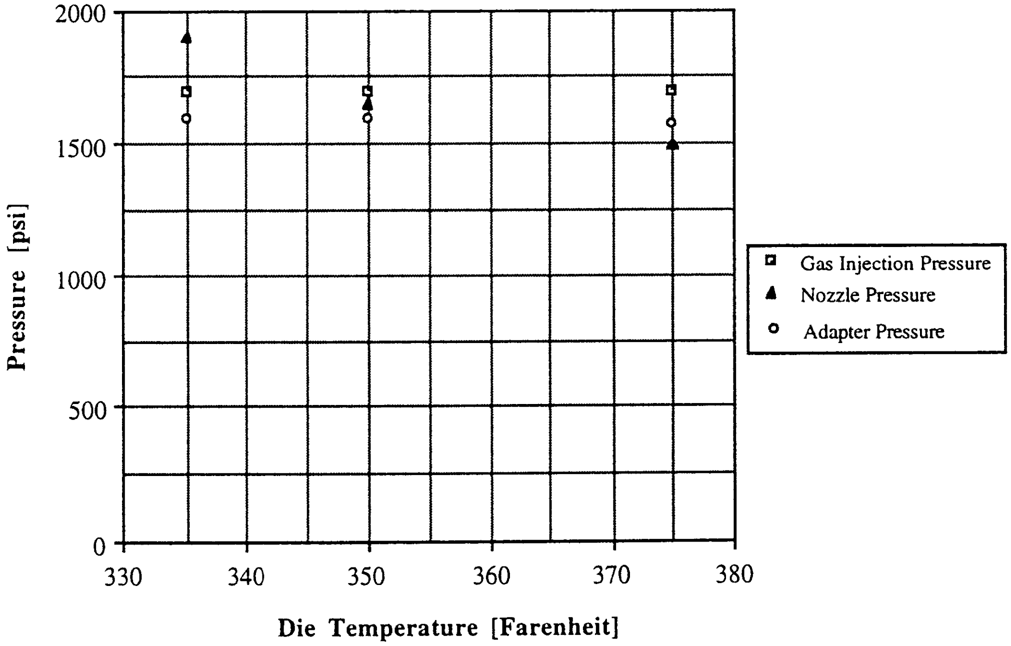

Figure 8.39 Plot of processing pressures versus die temperature for the 0.03125"ϕ, 0.500"L die with PP and carbon dioxide injection.

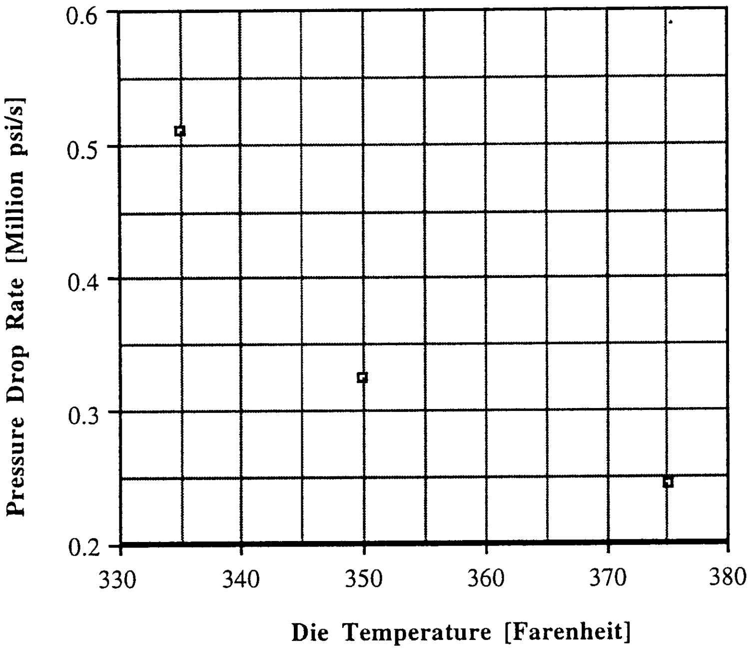

Figure 8.40 Plot of approximate pressure drop rate (ΔP/Δt) versus die temperature for the 0.03125"ϕ, 0.500"L die with PP and carbon dioxide injection.

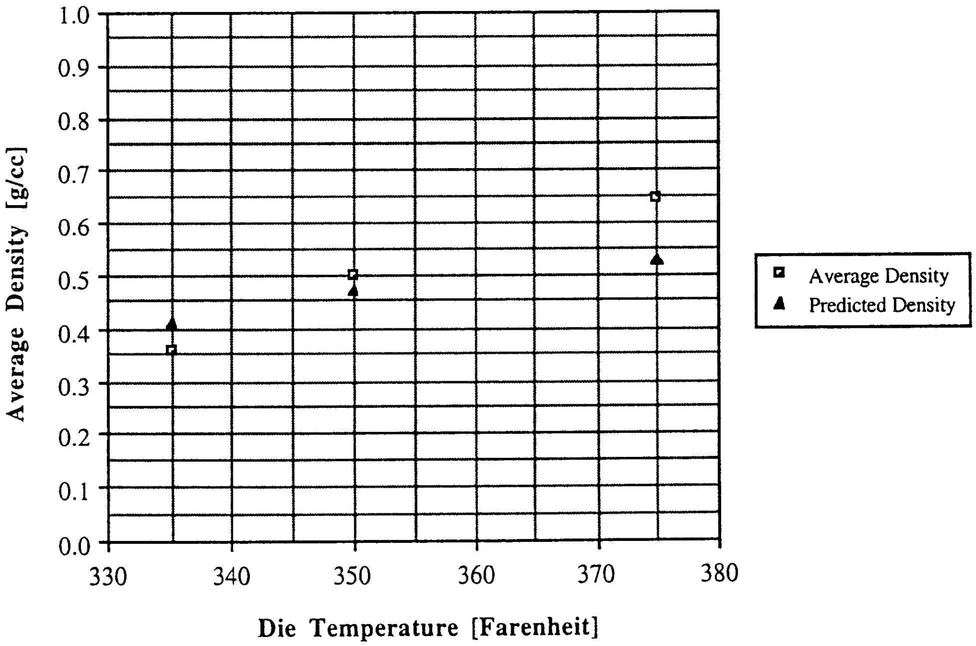

Figure 8.41 Plot of average foam density versus die temperature for the 0.03125"ϕ, 0.500"L die with PP and carbon dioxide injection.

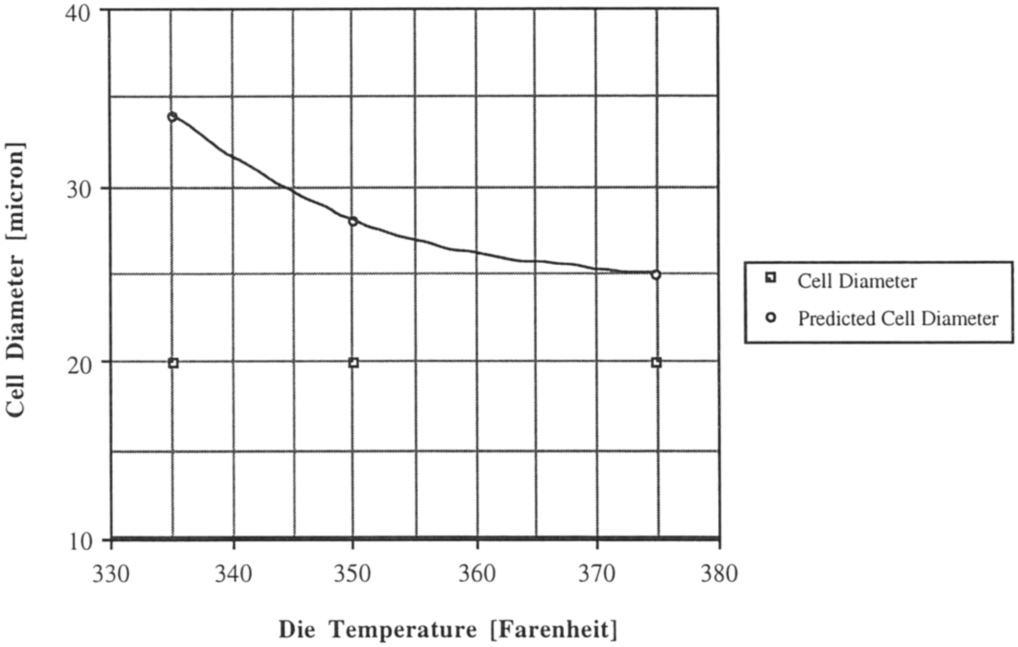

Figure 8.42 Plot of experimental and theoretically predicted average cell size versus die temperature for the 0.03125"ϕ, 0.500"L die with PP and carbon dioxide injection.

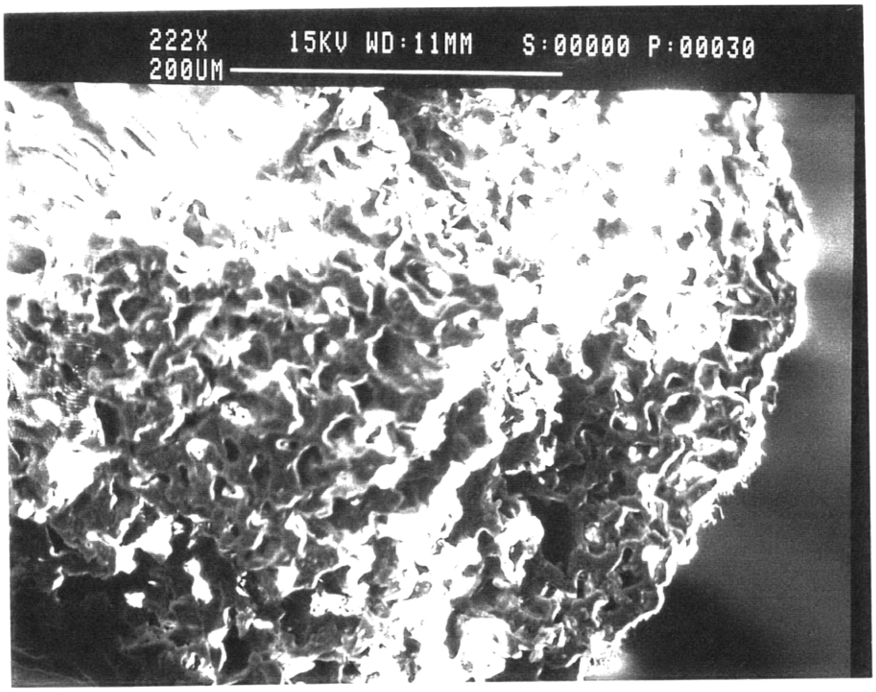

Figure 8.43 SEM micrograph of PP filament extruded through 0.03125"ϕ, 0.500"L with T_{die}=335°F and carbon dioxide injection.

8.3 EXPERIMENTS WITH WIRE COATING DIES

Section 8.2 described the experiments that were performed with the tandem extrusion system and filament extrusion dies. The next series of experiments were performed with wire coating dies. Two kinds of wire were used for experimentation. The first wire type was a 24 AWG (0.020" diameter) while the second was a 30 AWG (0.010" diameter). In both cases the effect of die geometry, die temperature, and wire speed on final insulation diameter and capacitance were studied. Moreover, the effects of both types of gas (nitrogen and carbon dioxide) were taken into account. It must be noted, however, that the number of experiments that could be performed with wires was limited since the pay-off and take-up equipment that were utilized for running experiments failed to provide adequate wire centering and tension adjustment.

The two important characteristics of a wire are its final outside diameter (OD) and its capacitance (C). The capacitance itself is a function of the final OD and the dielectric K of the insulating material. This relationship is discussed in Chapter 1 and is mentioned here again (Patil, 1995):

$$C = \frac{7.354}{\log_{10}\left(\frac{D}{d}\right)} K \tag{8.1}$$

where,

D=Core OD
d=Conductor OD
K=Dielectric constant of insulation.

Thus, it is obvious that controlling the dielectric constant of the insulation is of primary importance. The lower the dielectric constant for a given core OD the lower the capacitance and the more desirable the wire properties. The dielectric constant is also important for its effect on signal transmission speeds through the wire given by the following relation:

$$VP = \frac{100}{\sqrt{K}} \tag{8.2}$$

In the above relation the velocity of propagation VP is expressed as a percentage of the velocity of light.

The microstructure of the foamed insulation directly affects its dielectric constant. The dielectric constant is a function of the void fraction of the final foamed insulation. Using a linear relationship based on the rule of mixture we can approximate the dielectric constant as follows:

$$K \approx K_{pol}\,(1 - VF) + K_{gas} VF \tag{8.3}$$

The dielectric constant of the gas can be taken to be approximately equal to that of air. Thus,

$$K \approx K_{pol} - (K_{pol} - 1)VF \tag{8.4}$$

Thus, experiments are performed to understand the relationship between different extrusion and parameters and the final insulation OD and its dielectric constant. Since the dielectric constant along with the insulation OD determines the capacitance, it is the variation in the capacitance that is studied during the experiments. Another reason for recording the capacitance is that unlike the void fraction or the dielectric constant, it can be measured on-line.

8.3.1 Experiments with 24 AWG wire

Effect of Pressure Drop and Wire Velocity

Table 8.7 documents the experimental conditions and results for the set of experiments run in order to ascertain the effect of pressure drop across the die. The die used for all experiments in this set is a 0.080" diameter, 0.500" long pressure extrusion die.

0.080"ϕ, 0.500"L Die

Resin	Quantum PP1610PF
Gas	Nitrogen
Extruder rpms	Wayne: Varied Royle: Varied
Wire Speed	As noted

Temperature Settings

Wayne	Zone 1: 350°F	Royle	Zone 1: 375°F	Head Flange: 375°F
	Zone 2: 375°F		Zone 2: 375°F	X-head and Die: 375°F
	Zone 3: 375°F		Zone 3: 375°F	
	Zone 4: 375°F		Zone 4: 375°F	
	Adapter: 225°F		Zone 5: 375°F	

Wire Velocity [ft/min]	Die Pressure Drop [psi]	Coating Thickness [1/1000 in]	Capacitance [pF]
40	2040	28	23.8
	2480	31	21.5
	3100	34	20.0
50	2060	25	25.9
	2520	28	23.7
	2990	30	20.7
60	2010	24	27.8
	2540	26	23.2
	2950	28	22.5

Table 8.8 Experimental conditions and data for the 0.080"ϕ, 0.500"L die with nitrogen injection.

The results are depicted graphically in Figures 8.44 and 8.45. Figure 8.44 shows the variation in coating thickness with pressure drop across the die and the wire velocity. Figure 8.45 shows how the capacitance varies with change in die pressure drop.

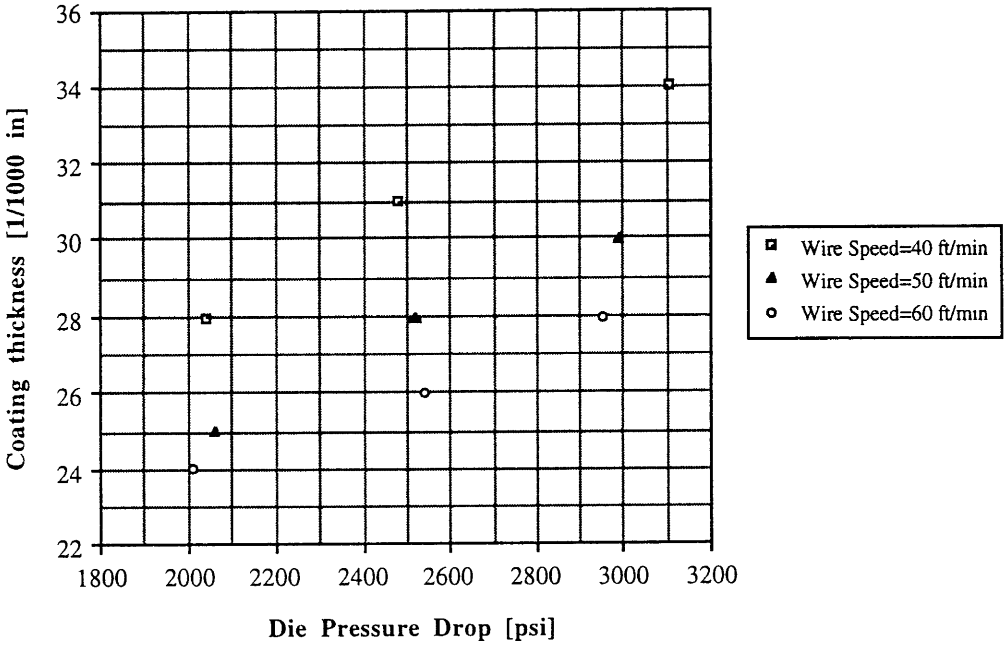

Figure 8.44 Plot of wire coating thickness versus pressure drop across die for various wire speeds with PP and nitrogen injection.

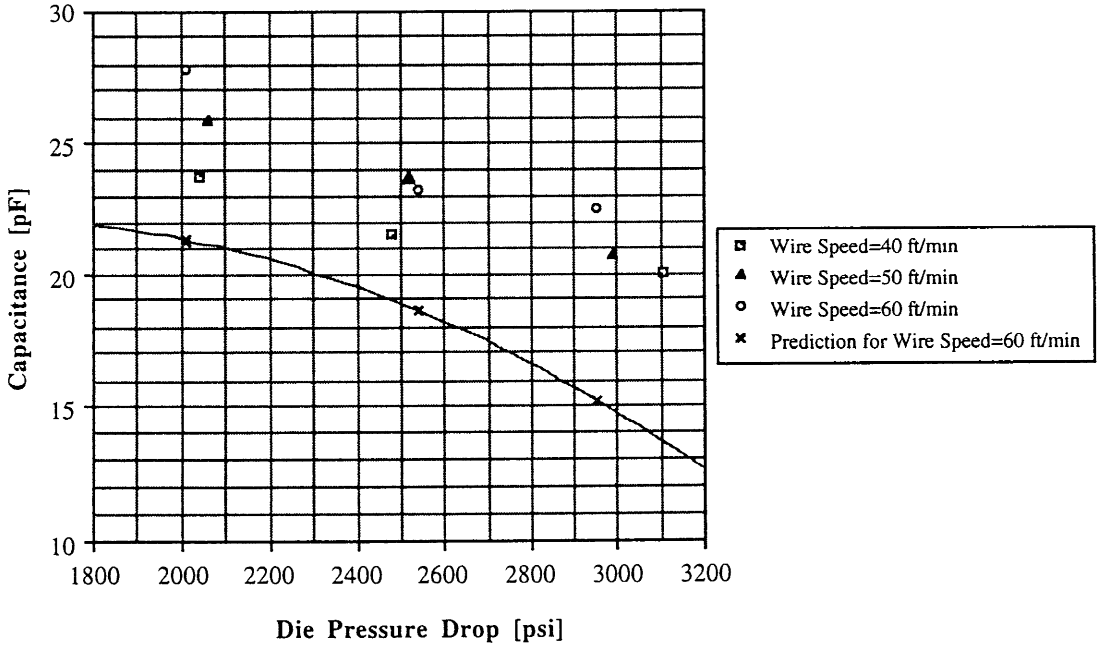

Figure 8.45 Plot of wire capacitance versus pressure drop across die for different wire speeds with PP and nitrogen injection.

It can be seen that as the pressure drop across the die increases, the diameter of the insulation increases. This can be explained by the increase in the flow rate of the foam that accompanies the increase in pressure. In fact, the relation between insulation OD and the extrusion parameters for Newtonian isothermal flow with lubrication approximation in pressure extrusion is given as follows (Tadmor and Gogos, 1979):

$$t = 0.5\left[\frac{\Delta P\{(D_{die} - D_{conductor})/2\}^3}{6\mu LV} + 0.5(D_{die} - D_{conductor})\right] \qquad (8.5)$$

where, ΔP=Die pressure drop
D_{die}=Die diameter
$D_{conductor}$=Conductor diameter=Insulation ID
μ=Polymer/gas solution viscosity
L=Die length
V=Wire speed

Thus, it can easily be explained why the coating thickness increases with increase in pressure drop across the die. This increase in insulation OD has a direct effect on the capacitance (as seen in Equation 8.1). However, the void fraction also varies with increase in pressure drop which implies that the dielectric constant K in Equation 8.1 also changes. This also affects the capacitance.

Figures 8.46, 8.47, and 8.48 show some micrographs from to illustrate the effect of pressure drop variation.

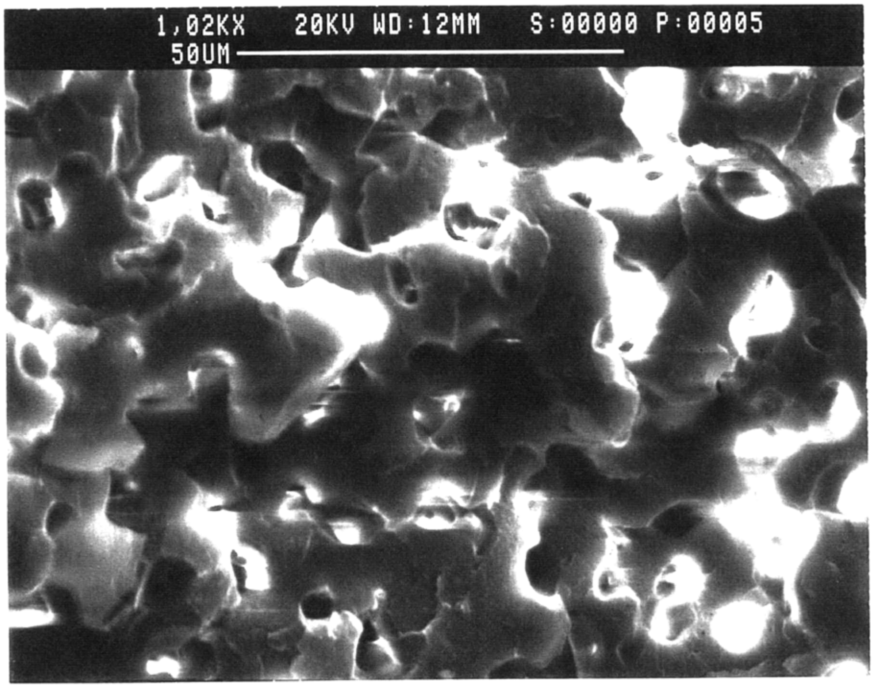

Figure 8.46 SEM micrograph of PP wire coating extruded through 0.080" ϕ, 0.500" L die with nitrogen injection and die pressure drop of 2060 psi.

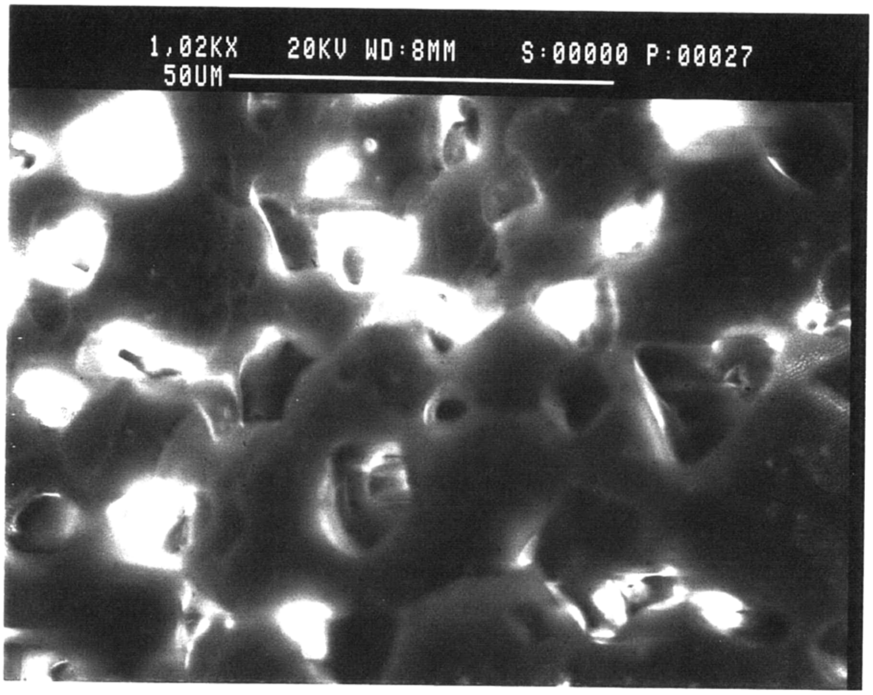

Figure 8.47 SEM micrograph of PP wire coating extruded through 0.080" ϕ, 0.500" L die with nitrogen injection and die pressure drop of 2520 psi.

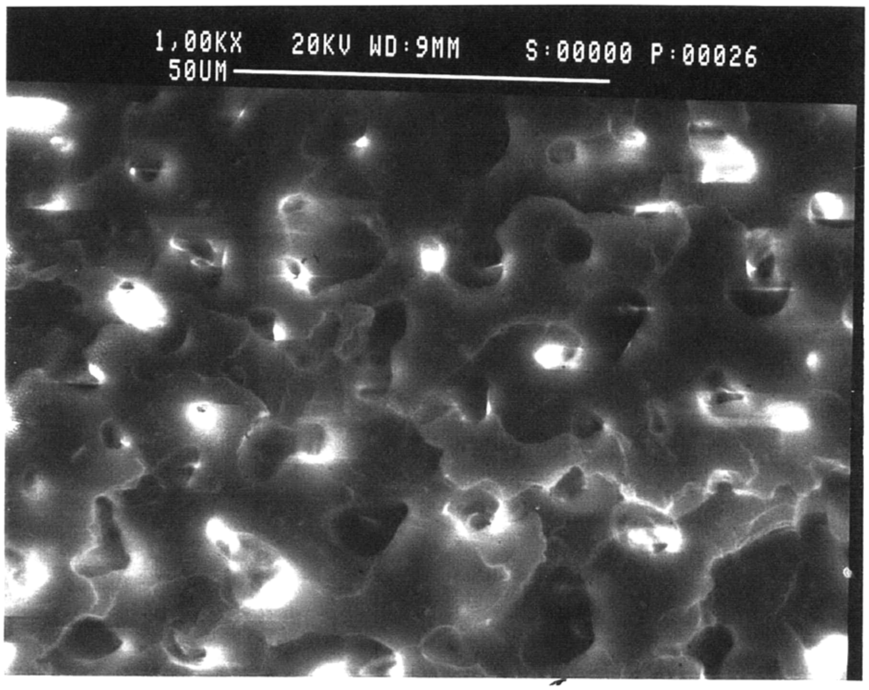

Figure 8.48 SEM micrograph of PP wire coating extruded through 0.080" ϕ, 0.500" L die with nitrogen injection and die pressure drop of 2990 psi.

Effect of die geometry and die temperature

Table 8.8 shows the conditions for the set of experiments performed to evaluate the effect of die geometry and temperature. The die diameter for this set of experiments was 0.080". The die length varied from 0.200" to 0.500". A pressure drop of approximately 2500psi was maintained across the dies in all the cases and the wire speed was held constant at 50 ft/min. The die temperature was lowered from 375°F to 350°F. The die temperature could not be lowered any further due to problems of lack of adhesion between the conductor and the foam below 350°F. Figures 8.49, 8.50 and 8.51 show the effect of die geometry and temperature graphically.

As seen from Figure 8.50 the coating thickness increases with decrease in die length. This can readily be explained by referring to Equation (8.5). The capacitance also varies since the void fraction varies due to change in the die geometry. Figure 8.51 shows this variation in capacitance. The theoretical model developed in Chapter 4 is again used to predict microstructure and the final void fraction. Based on this prediction of void fraction, the dielectric constant and the capacitance are calculated from Equations (8.4) and (8.1) respectively. This predicted capacitance is also plotted in Figure 8.51. As in the case of filament extrusion, it is easily seen that the final void fraction estimates consistently exceed the actual experimental values which lead to lower estimates of capacitance than those that are actually obtained. Figure 8.52 shows a sample micrograph from this experiment set.

0.080"ϕ Dies

Resin	Quantum PP1610PF
Gas	Nitrogen
Extruder rpms	Wayne: Varied Royle: Varied
Wire Speed	50 ft/min

Temperature Settings

Wayne	Zone 1: 350°F	Royle	Zone 1: 375°F	Head Flange: 375°F
	Zone 2: 375°F		Zone 2: 375°F	X-head and Die: As noted
	Zone 3: 375°F		Zone 3: 375°F	
	Zone 4: 375°F		Zone 4: 375°F	
	Adapter: 225°F		Zone 5: 375°F	

Die Temperature [°F]	Die Length [in]	Coating Thickness [1/1000 in]	Capacitance [pF]
375	0.2	47	17.5
	0.3	34	20.1
	0.4	32	21.9
	0.5	28	23.1
350	0.2	50	15.8
	0.3	38	17.3
	0.4	37	17.6
	0.5	35	17.9

Table 8.9 Experimental conditions and data for the 0.080"ϕ die set with nitrogen injection.

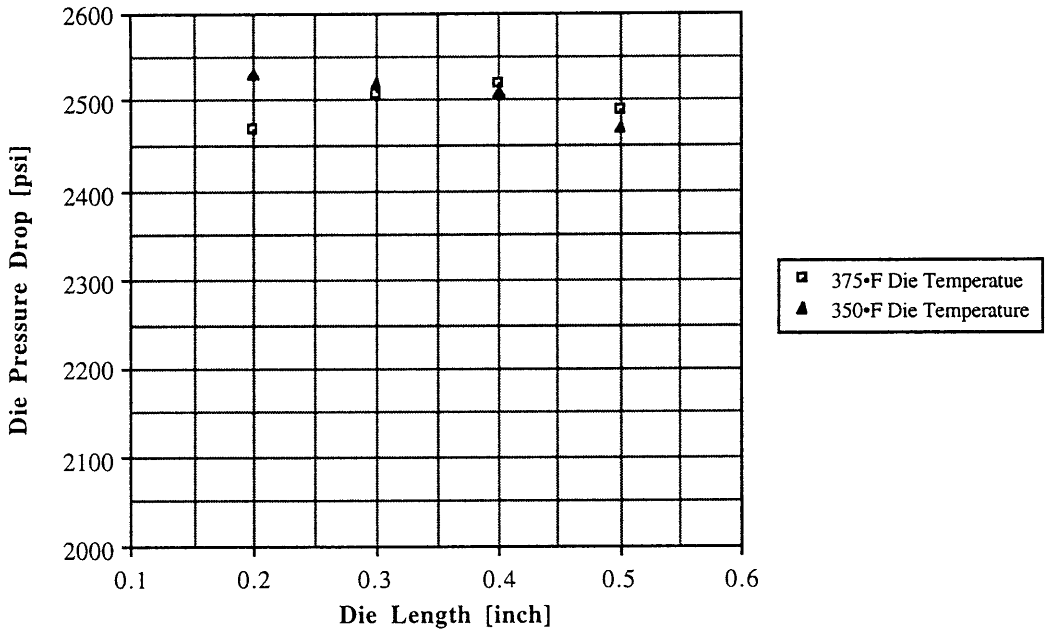

Figure 8.49 Plot of die pressure drop versus die length for a 0.080"ϕ die set with PP and nitrogen injection. Extruder rpms were adjusted to maintain roughly 2500 psi ΔP.

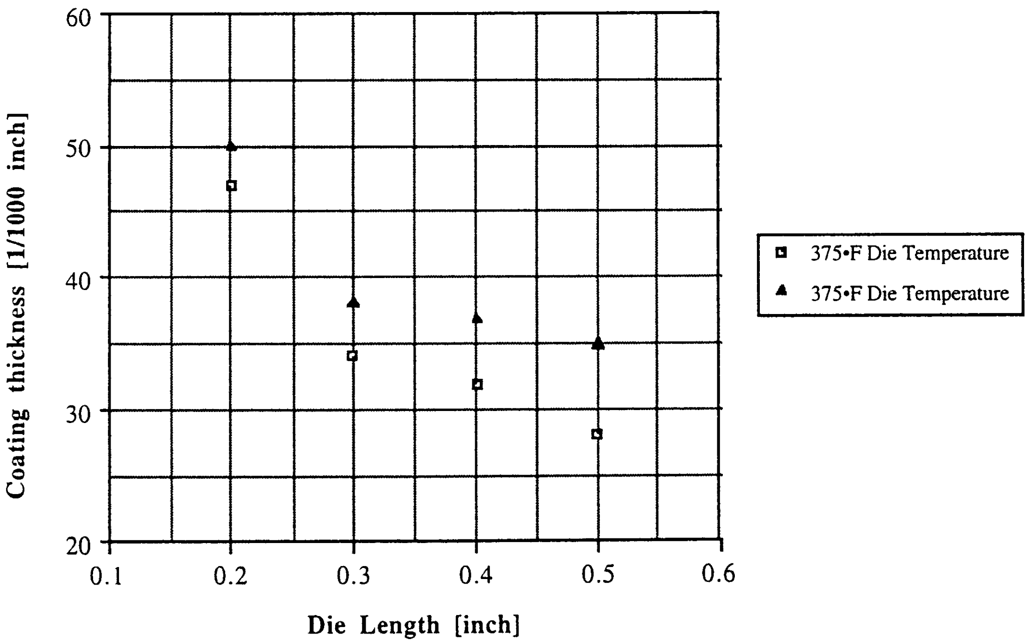

Figure 8.50 Plot of coating thickness versus die length for 0.080"ϕ die set with PP and nitrogen injection.

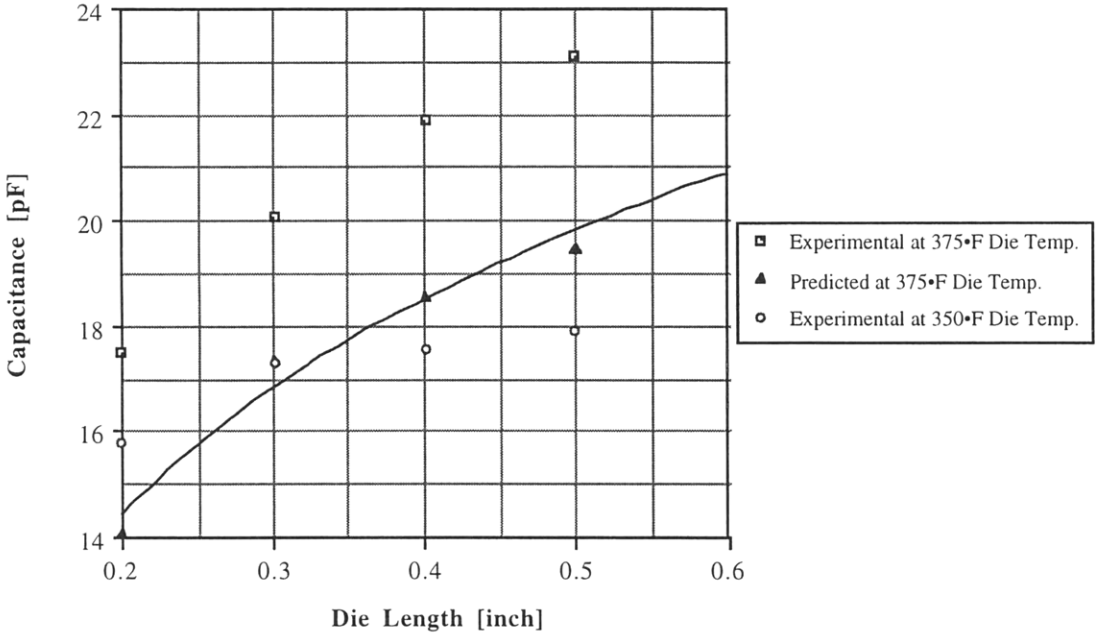

Figure 8.51 Plot of capacitance versus die length for 0.080" ϕ die set with PP and nitrogen injection.

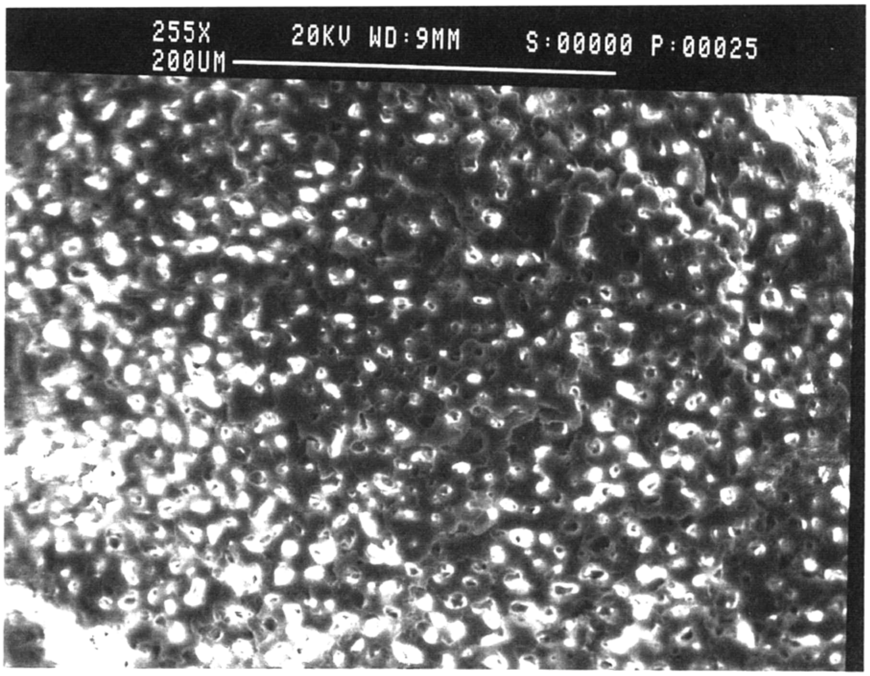

Figure 8.52 SEM micrograph of PP wire coating extruded though 0.080" ϕ, 0.500"L die with nitrogen injection and T_{die}=350°F.

Effect of gas type

After the effects of die geometry, die temperature and die pressure drop have been studied, it is important to ascertain the effects of the type of gas used for the foaming process. The relative effect of using nitrogen versus carbon dioxide injection are summarized in Table 8.9. It is seen from Table 8.9 that the die pressure drop for carbon dioxide injection is lower than the case of nitrogen injection. This can be explained by the significant drop in viscosity due to carbon dioxide injection as is mentioned in the case of filament extrusion.

Figure 8.53 shows that the coating thickness is larger in the case of carbon dioxide injection. This can be explained by the higher flow rate due to reduced viscosity when carbon dioxide is injected. Figure 8.54 shows that the capacitance is much lower when carbon dioxide is used. This again can be explained by the effect of larger insulation OD as well as the fact that the void fraction is larger when carbon dioxide is injected as was seen in the case of filament extrusion.

Figures 8.55 and 8.56 show the micrographs of wire coating samples extruded with injection of nitrogen and carbon dioxide respectively. It is seen from the micrographs that though the cell size of the two samples are close, the injection of carbon dioxide produces higher cell density (number of cells per cubic centimeter) in the final insulation. The higher void fraction in this case is thus a result of higher cell density which is a desirable result.

0.080"ϕ, 0.500"L Die

Resin	Quantum PP1610PF
Gas	As noted
Extruder rpms	Wayne: Varied Royle: Varied
Wire Speed	50 ft/min

Temperature Settings

Wayne	Zone 1: 350°F	Royle	Zone 1: 375°F	Head Flange: 375°F
	Zone 2: 375°F		Zone 2: 375°F	X-head and Die: As 375°F
	Zone 3: 375°F		Zone 3: 375°F	
	Zone 4: 375°F		Zone 4: 375°F	
	Adapter: 225°F		Zone 5: 375°F	

Gas	Die Pressure Drop [psi]	Coating Thickness [1/1000 in]	Capacitance [pF]
Nitrogen	2060	25	25.9
	2520	28	23.1
	2990	30	20.7
Carbon Dioxide	1700	31	20.5
	1900	34	18.9
	2100	42	16.3

Table 8.10 Experimental conditions and data for the 0.080"ϕ, 0.500"L die with nitrogen injection and carbon dioxide injection.

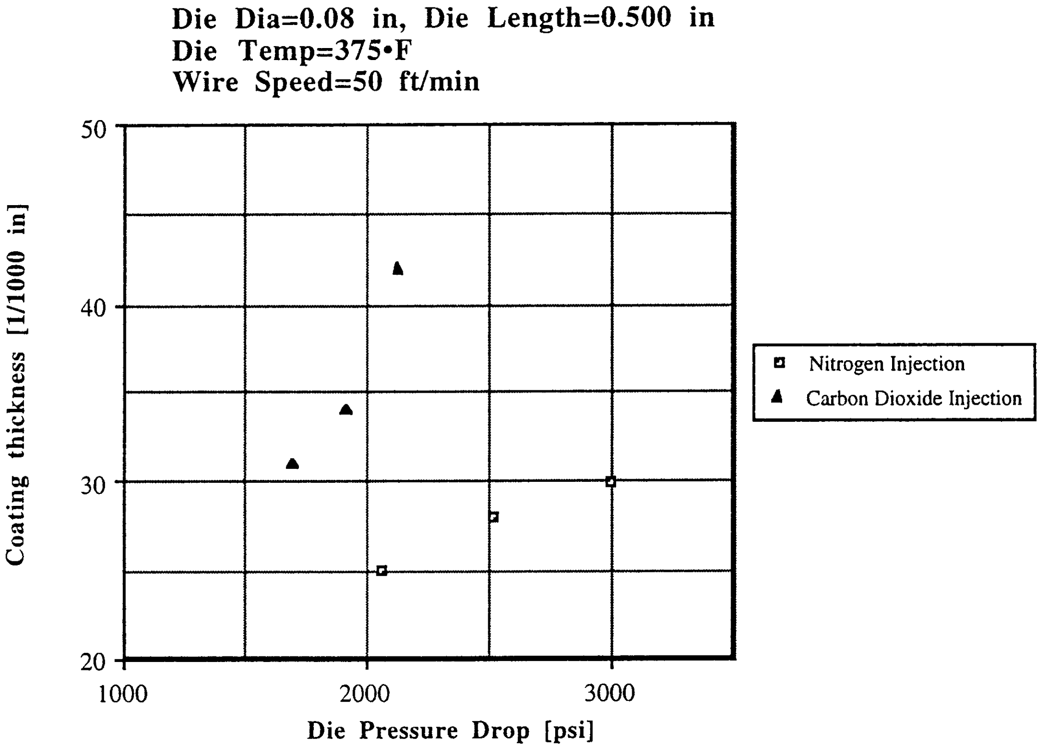

Figure 8.53 Plot of coating thickness versus die pressure drop for different gas types.

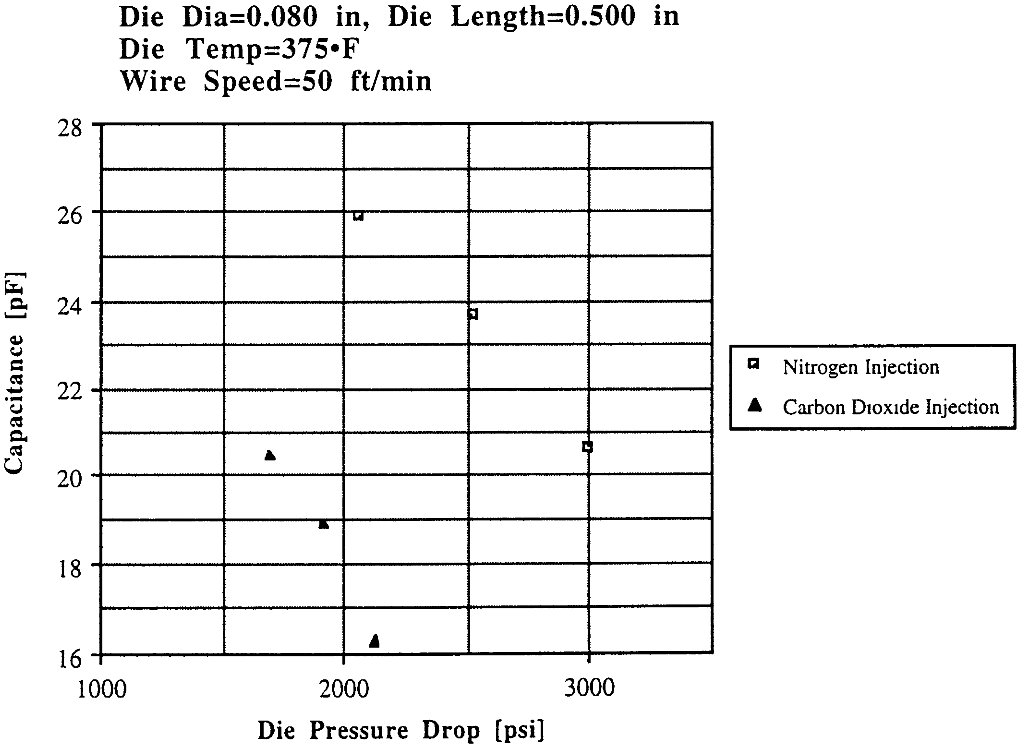

Figure 8.54 Plot of capacitance versus die pressure drop for different gas types.

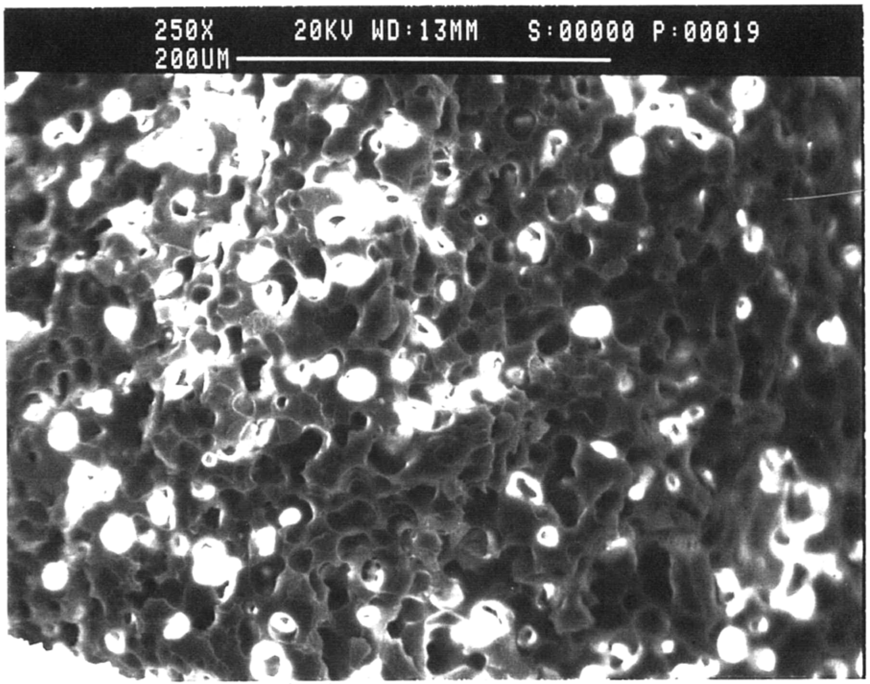

Figure 8.55 SEM micrograph of PP wire coating extruded through 0.080"ϕ, 0.500"L die with nitrogen injection and die pressure drop of 2060 psi.

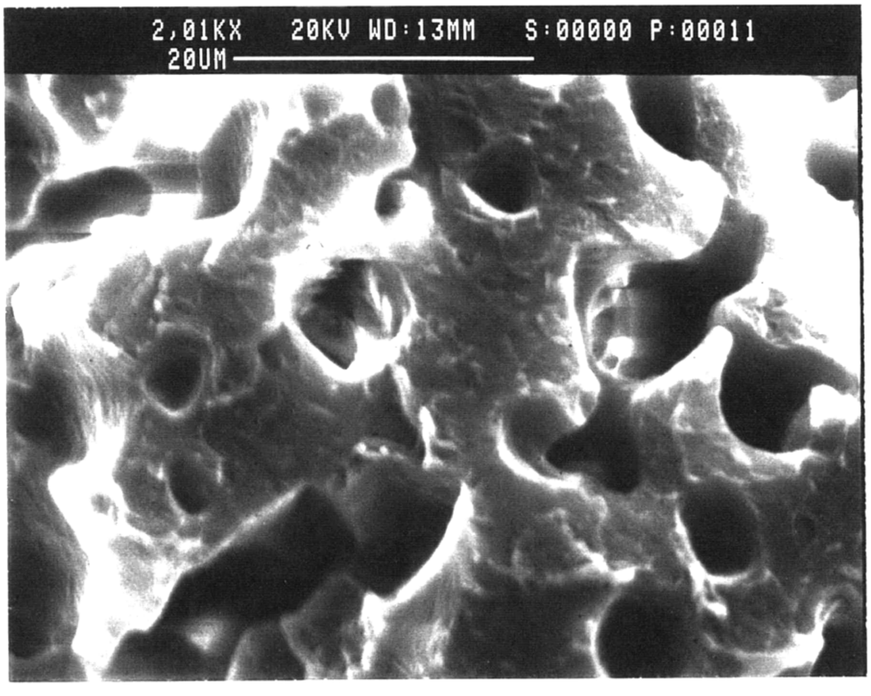

Figure 8.56 SEM micrograph of PP wire coating extruded through 0.080"ϕ, 0.500"L die with carbon dioxide injection and die pressure drop of 2100 psi.

Experiments with 30 AWG Wire

The conditions at which wire coatings could successfully be extruded for the 30 AWG wire were very limited due to the finer gage size of the wire and the inability of the tension adjusting devices to function properly. The wire would frequently break due to lack of proper tension adjustment and so it was not possible to change extrusion parameters over a range of values and determine their effects. However, it was possible to obtain a few samples for some conditions. Figure 8.57 shows two such samples. The conditions at which they were obtained are noted.

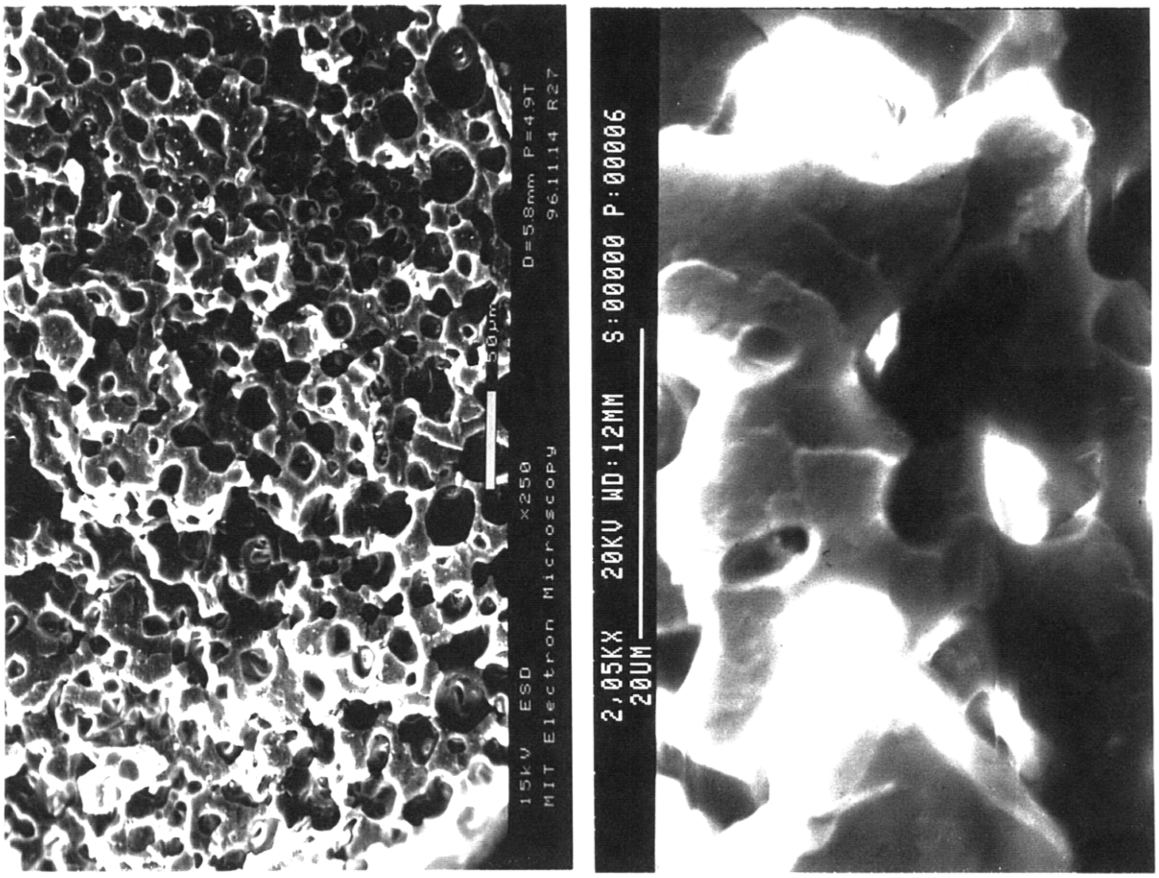

Polymer: PP
Gas: Carbon Dioxide
Die Dia=0.060 in
Die Length=0.400 in
Die Temp=375°F
Wire Velocity=42 ft/min
Insulation OD=0.043 in
K=1.52 (estimated)

Polymer: PP
Gas: Nitrogen
Die Dia=0.050 in
Die Length=0.300 in
Die Temp=375oF
Wire Velocity= 28ft/min
Insulation OD=0.037 in
K=1.54 (estimated)

Figure 8.57 SEM micrographs of extruded 30 AWG wire coatings.

8.4 CONCLUSION

A series of experiments with both filament extrusion dies and wire coating dies has been performed. The experiments have revealed the effect that different extrusion parameters have on the cell microstructure. The comparison between the experimental results and the those that were predicted theoretically with the model developed in Chapter 4 show reasonably good qualitative agreement. The predicted cell sizes are on average about 30% larger than the experimental values while the void fractions are about 10 to 20% lower. The model predicts qualitatively what will happen to cell sizes, cell densities, and void fractions if extrusion parameters are changed. This qualitative agreement between the model and the experimental results has clearly been established.

An important implication of these numerous experiments is that if the present microcellular extrusion system is scaled up, then only a handful of experiments need to be run to evaluate the fitting parameter Ω which is an input to the nucleation rate equation (4.26). Once these few experiments have been performed, the theoretical model can be used to predict the effect of various extrusion parameters on the cell morphology. It will be possible to vastly reduce the number of experiments required, as well as the uncertainty when scaling up such a system. The model can predict the location of some optimal operating point which will depend on the customer's particular requirements.

Thus, a theoretical model in combination with a prototype system has been used in this chapter to determine the feasibility of a future industrial-scale microcellular extrusion system.

CHAPTER 9

CONCLUSIONS, RECOMMENDATIONS AND SUGGESTIONS FOR FUTURE WORK

9.1 CONCLUSIONS

This research has encompassed both theoretical modeling of the microcellular extrusion process and the actual design and fabrication of a prototype system. The prototype has been successfully used to demonstrate the viability of an actual microcellular wire coating line. The accuracy and limitations of the theoretical modeling process were also established with the aid of experiments. These experiments indicate that the predictions of cell size and cell density made with the aid of the model fits the experimental data qualitatively. Thus, there are several important conclusions that can be derived from this research work.

9.1.1 Comparison of modeling predictions and experimental results

There are a few key observations when comparing the modeling results with the experimentally obtained ones. These observations are summarized below.

(1) Cell size predictions are 10 to 40% larger than experimental values.

(2) Cell density predictions are approximately 20% smaller than experimental values.

(3) Void fraction predictions are significantly larger than experimental values.

(4) Modeling predictions and experimental results show qualitative agreement in trends.

9.1.2 Scaling-up implications

If the present prototype is scaled-up, then on the basis of the discussions in the preceding section (Section 9.1.1) , the following conclusions can be arrived at.

(1) Only a minimal number of experiments need to be run as base cases.

(2) Starting with these base cases, the model can be used to predict the effect of parameter variation.

(3) Target specifications (e.g. cell size, cell density, and void fraction) depending on the type of application of the final product can be met. Wire insulation of a specified thickness and electrical characteristics can be produced with relative accuracy and repeatability.

(4) If there is an optimal operating point for the extrusion system, then the model can predict it.

(5) The model can be used to design a decoupled (and thus controllable) wire extrusion system and in the process can save expense on unnecessary hardware and complexity.

9.2 RECOMMENDATIONS AND SUGGESTIONS FOR FUTURE WORK

Recommendations for future work include improvements in modeling efforts as well as in the hardware used to fabricate the system. Future work in the area of microcellular plastics should involve refining the theoretical analysis and dealing with the issues of the model outlined in Section 4.12. There are also many improvements that can be made in the area of stabilizing and controlling the process through the use of better components and equipment.

9.2.1 Recommendations for modeling

The recommendations in the area of modeling and analysis are summarized below:

(1) Enhanced understanding of the thermodynamics of polymer/gas solutions.

(2) Superior knowledge of the rheology of polymer/gas solutions.

(3) Numerical analysis improvement by using a finite difference or finite element scheme for solution of the equations in Chapter 4.

9.2.2. Recommendations for hardware

Improvement in the equipment used for the system can also enhance its performance. These suggested improvements are summarized:

(1) The gas flow injection and metering system should be able to perform reliably and accurately.

(2) The design of adapters and couplings to perform under high pressure will avoid leakage problems in the system.

(3) The crosshead design should be improved to streamline flows which will lead to unnecessary pressure losses and eliminate problems of adherence between conductor and the insulation.

(4) Tension adjustment devices used in the wire coating process should be improved to handle finer size wires.

(5) Superior temperature controllers and heaters should be used for the extruders and dies.

The actual scaling up of a wire line should be proceeded with in order to commercialize the process and to further verify the validity of the analysis.

REFERENCES

Baldwin, D.F., 1994, "Microcellular Polymer Processing and the Design of a Continuous Sheet Processing System," *Ph.D. Thesis in Mechanical Engineering*, Massachusetts Institute of Technology, January.

Cha, S.W., 1994, "A Microcellular Foaming/Forming Process Performed at Ambient Temperature and a Super-Microcellular Foaming Process," *Ph.D. Thesis in Mechanical Engineering*, Massachusetts Institute of Technology, April.

Cha, S.W., Suh, N.P., Baldwin. D.F., and Park, C.B., 1992, "Microcellular Thermoplastic Foamed with Supercritical Fluid," US Patent 5158986.

Collias, D.I. and Baird, D.G., 1992, "Does a Microcellular Structure Improve the Modulus of Toughness of a Polymer Matrix," *Society of Plastics Engineers Technical Papers*, Vol. 38, pp. 1532-1535.

Colton, J.S. and Suh, N.P., 1986, "The Nucleation of Microcellular Thermoplastic Foam: Process Model and Experimental Results," *Advanced Manufacturing Processes*, Vol. 1, No. 7, pp. 485-492.

Colton, J.S. and Suh, N.P., 1987a, "Nucleation of Microcellular Foam: Theory and Practice," *Polymer Engineering and Science*, Vol. 27, pp. 500-503.

Colton, J.S. and Suh, N.P., 1987b "The Nucleation of Microcellular Thermoplastic Foam with Additives: Part 1: Theoretical Considerations," *Polymer Engineering and Science*, Vol. 27, pp. 485-492.

Colton, J.S. and Suh, N.P., 1987c "The Nucleation of Microcellular Thermoplastic Foam with Additives: Part 2: Experimental Results and Discussion," *Polymer Engineering and Science*, Vol. 27, pp. 493-499.

Colton, J.S. and Suh, N.P., 1992 "Microcellular Semi-Crystalline Thermoplastics," U.S. Patent 5160674.

Durril, P.L. and Griskey, R.G., 1966, Diffusion and Solution of Gases in Thermally Softened or Molten Polymers: Part I, "*A.I.Ch.E. Journal*, Vol. 12, pp. 1147-1151.

Durril, P.L. and Griskey, R.G., 1969, Diffusion and Solution of Gases in Thermally Softened or Molten Polymers: Part II, "*A.I.Ch.E. Journal*, Vol. 15, pp. 106-110.

Flory, P.J., 1953, Principles of Polymer Chemistry, Cornell University Press.

Graff, G., ed., Mid-November 1993 Issue, *Modern Plastics Encyclopedia '94 & Buyer's Guide Issue*. McGraw-Hill, Inc., Vol. 70, No. 12, New York. Pp. 24-45.

Gyftopolous, E.P. and Beretta, G.P., 1991, Thermodynamics: Foundations and Applications, Macmillan, New York.

Herrmann, T., 1995, "The Role of a Gear Throttle as a Nucleation Device in Continuous Supermicrocellular Polymer Extrusion," *Diploma Engineer's Thesis*, University of Stuttgart, Germany, and Departmant of Mechanical Engineering, Massachusetts Institute of Technology, Cambridge, March.

Koros, W.J., and Paul, D.R., 1980, "Sorption and Transport of CO_2 Above and Below the Glass Transition of Poly(ethylene terephthalate)," Polymer Engineering and Science, Vol. 20, pp. 14-19.

Kumar, V., 1988, "Process Synthesis for Manufacturing Microcellular Thermoplastic Parts: A Case Study in Axiomatic Design, "*Ph.D. Thesis in Mechanical Engineering*, Massachusetts Institute of Technology, May.

Kumar, V. and Suh, N.P., 1989, "Production of Microcellular Plastic Parts," ASME Winter Annual Meeting, San Francisco.

Kumar, V. and Suh, N.P., 1990, "A Process for Making Microcellular Thermoplastic Plastic Parts," Polymer Science and Engineering, Vol. 30, pp. 1323-1329.

Lundberg, J.L., Wilk, M.B., and Huyett, M.J., 1966, *Journal of Applied Physiscs*, Vol. 31, P.1131.

Martini, J.E., 1981, "The Production and Analysis of Microcellular Foam," *S.M. Thesis in Mechanical Engineering*, Massachusetts Institute of Technology, January.

Martini-Vredensky, J.E., Suh, N.P., and Waldman, F.A., 1984, "Microcellular Closed Cell Foams and Their Method of Manufacture," US Patent 4473665.

Newitt, D.M., and Weale, K.E., 1948, "Solution and Diffusion of Gases in Polystyrene at High Pressures," *Journal of Chemical Science*, Part II, pp. 1541-1549.

Ng, C.Y., 1997, "Extrusion of Microcellular Plastic Using a Tandem Foaming System : Design, Fabrication and Experimentation," *S.M. Thesis in Mechanical Engineering*, Massachusetts Institute of Technology, February.

Park, C.B., 1993, "The Role of Polymer/Gas Solutions in Continuous Processing of Microcellular Polymers," *Ph.D. Thesis in Mechanical Engineering*, Massachusetts Institute of Technology, May.

Park, C.B. and Suh, N.P., 1992a, "Extrusion of Microcellular Filament: A Case Study of Axiomatic Design," Cellular Polymers, MD-Vol. 38, ASME, pp. 69-91.

Patil, R. R., 1995, "Microcellular Processing of Fluoropolymers and the Design of a Microcellular Foam Extrusion System for Wire Coating," *S.M. Thesis in Mechanical Engineering*, Massachusetts Institute of Technology, June.

Tadmor, Z. and Gogos, C.G., 1979, Principles of Polymer Processing, Wiley, New York.

Seeler, K.A., and Kumar, V., 1992, "Fatigue of Notched Microcellular Polycarbonate," Cellular Polymers, MD-Vol. 38, ASME , pp. 93-108.

Seeler, K.A., and Kumar, V., 1993, "Tension-Tension Fatigue of Microcellular Polycarbonate: Initial Results," *Journal of Reinforced Plastics and Composites*, Vol. 12, pp. 359-376.

Suh, N.P., 1990, The Principles of Design, Oxford, New York.

Van Krevelen, D.W., 1976, Properties of Polymers, Elsevier, New York.

Veith, W.R., Tam, P.M., and Michaels, A.S., 1966, *Journal of Colloid and Interface Science*, Vol. 22, pp. 360-370.

Waldman, F.A., 1982, "The Processing of Microcellular Foam," *S.M. Thesis in Mechanical Engineering*, Massachusetts Institute of Technology, January.

Walton, A.G., 1987, "Nucleation in Liquids and Solutions," Nucleation, Zettlemoyer, A.C., ed., M. Dekker, New York.

Weinkauff, D.H., and Paul, D.R., 1990, "Effects of Structural Order on Barrier Properties," Barrier Polymers and Structures, W.J. Koros ed., American Chemical Society, pp. 60-89.

Youn, J., 1984, "Lightweight Polyester Composites," *Ph.D. Thesis in Mechanical Engineering*, Massachusetts Institute of Technology, January.

Youn, J. and Suh, N.P., 1984, "Processing of Microcellular Polyester Composites," *Polymer Composites*, Vol. 6, pp.175-180.

APPENDIX A

EXPLODED VIEW OF THE CROSSHEAD SYSTEM

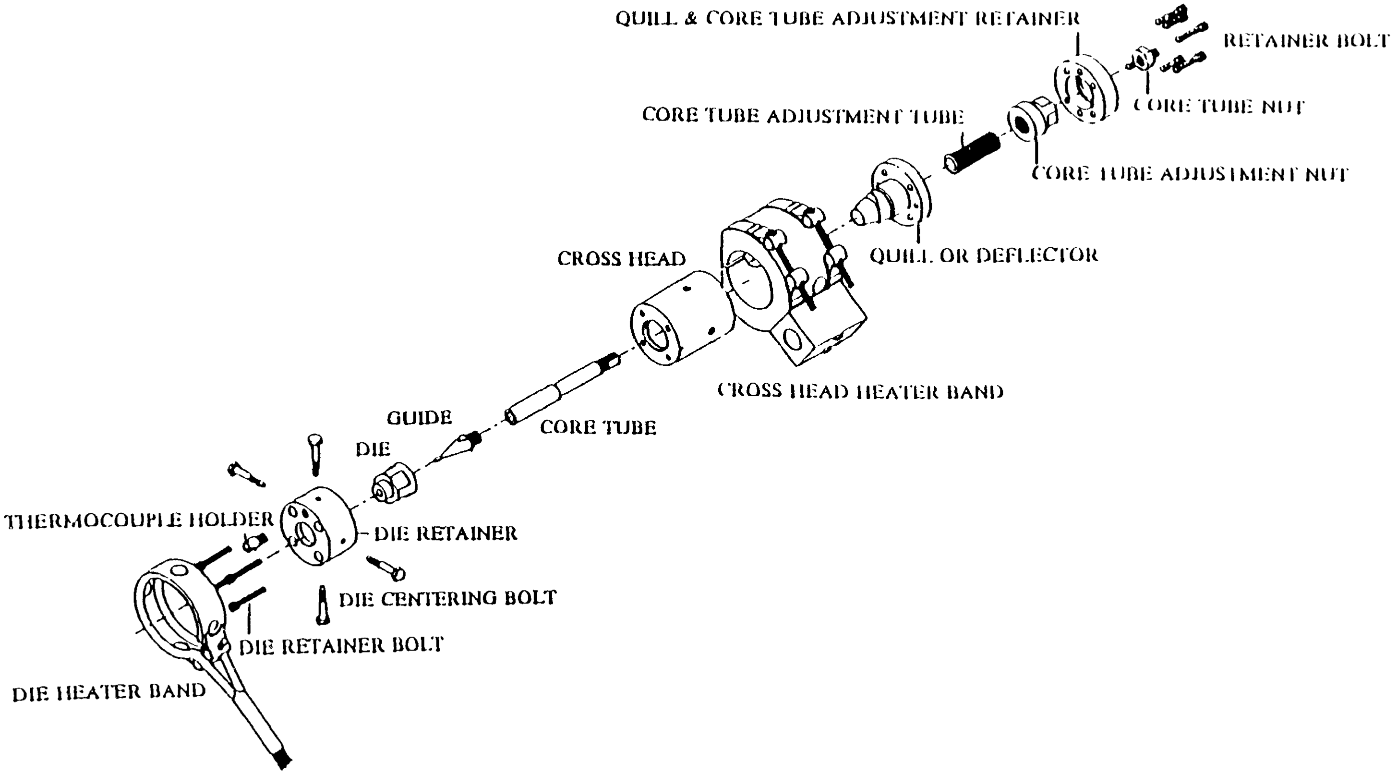

APPENDIX B

HIGH PRESSURE GAS CYLINDER INFORMATION

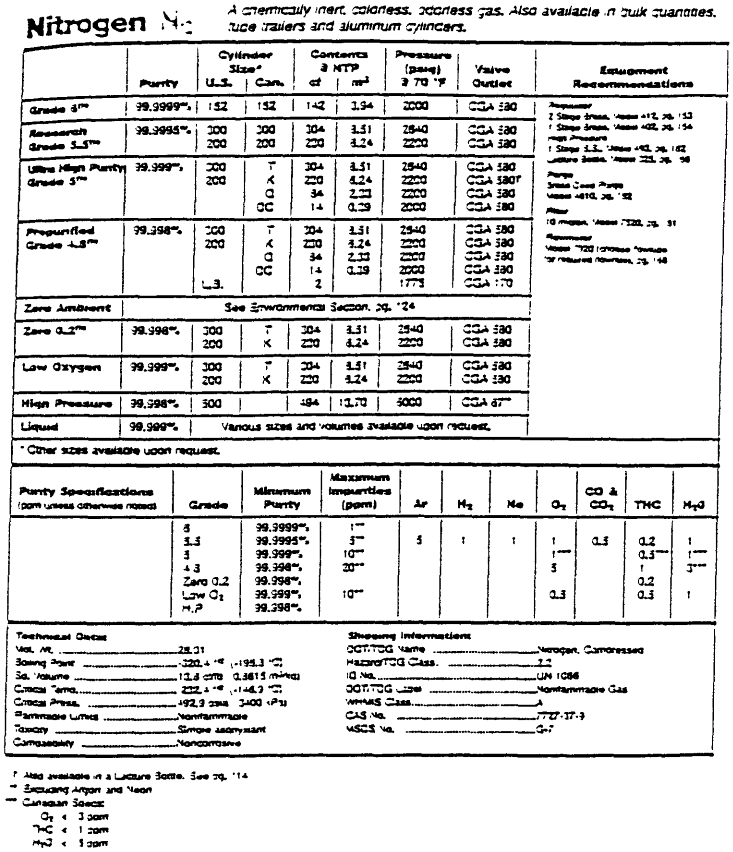

Nitrogen N_2

A chemically inert, colorless, odorless gas. Also available in bulk quantities, tube trailers and aluminum cylinders.

	Purity	Cylinder Size* U.S.	Cylinder Size* Can.	Contents @ NTP cf	Contents @ NTP m³	Pressure (psig) @ 70 °F	Valve Outlet	Equipment Recommendations
Grade 6™	99.9999%	152	152	142	3.94	2000	CGA 580	Regulator 2 Stage Brass, Model 412, pg. 153 1 Stage Brass, Model 402, pg. 154 High Pressure 1 Stage S.S., Model 493, pg. 162 Lecture Bottle, Model 221, pg. 56 Purge Brass Cross Purge Model 4810, pg. 152 Filter 10 micron, Model 7320, pg. 31 Flowmeter Model 7720 (choose flowtube for required flowrates, pg. 148)
Research Grade 5.5™	99.9995%	300 200	300 200	304 220	8.61 6.24	2640 2200	CGA 580 CGA 580	
Ultra High Purity Grade 5™	99.999%	300 200	T K Q QC	304 220 84 14	8.61 6.24 2.38 0.39	2640 2200 2200 2000	CGA 580 CGA 580† CGA 580 CGA 580	
Prepurified Grade 4.8™	99.998%	300 200 L.B.	T K Q QC	304 220 84 14 2	8.61 6.24 2.38 0.39	2640 2200 2200 2000 1775	CGA 580 CGA 580 CGA 580 CGA 580 CGA 170	
Zero Ambient	See Environmental Section, pg. 124							
Zero 0.2™	99.998%	300 200	T K	304 220	8.61 6.24	2640 2200	CGA 580 CGA 580	
Low Oxygen	99.999%	300 200	T K	304 220	8.61 6.24	2640 2200	CGA 580 CGA 580	
High Pressure	99.998%	300		494	13.70	6000	CGA 677	
Liquid	99.999%	Various sizes and volumes available upon request.						

* Other sizes available upon request.

Purity Specifications (ppm unless otherwise noted)	Grade	Minimum Purity	Maximum Impurities (ppm)	Ar	H_2	Ne	O_2	CO & CO_2	THC	H_2O
	6	99.9999%	1**							
	5.5	99.9995%	5**	5	1	1	1	0.5	0.2	1
	5	99.999%	10**				1***		0.5***	1***
	4.8	99.998%	20**				5		1	3***
	Zero 0.2	99.998%							0.2	
	Low O_2	99.999%	10**				0.3		0.5	1
	H.P.	99.998%								

Technical Data

Mol. Wt.	28.01
Boiling Point	-320.4 °F (-195.8 °C)
Sp. Volume	13.8 cf/lb (0.8615 m³/kg)
Critical Temp.	-232.4 °F (-146.9 °C)
Critical Press.	492.9 psia (3400 kPa)
Flammable Limits	Nonflammable
Toxicity	Simple asphyxiant
Compatibility	Noncorrosive

Shipping Information

DOT/TDG Name	Nitrogen, Compressed
Hazard/TDG Class	2.2
ID No.	UN 1066
DOT/TDG Label	Nonflammable Gas
WHMIS Class	A
CAS No.	7727-37-9
MSDS No.	G-7

† Also available in a Lecture Bottle. See pg. 114

** Excluding Argon and Neon

*** Canadian Specs:
O_2 < 3 ppm
THC < 1 ppm
H_2O < 5 ppm

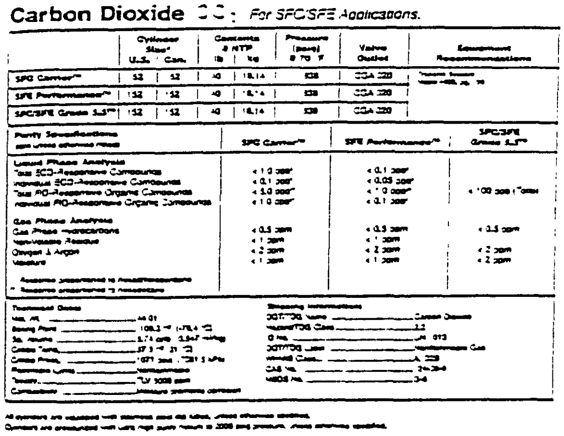

Carbon Dioxide CO_2

For SFC/SFE Applications.

	Cylinder Size* U.S.	Cylinder Size* Can.	Contents @ NTP lb	Contents @ NTP kg	Pressure (psig) @ 70 °F	Valve Outlet	Equipment Recommendations
SFC Carrier™	152	152	40	18.14	838	CGA 320	[illegible]
SFE Performance™	152	152	40	18.14	838	CGA 320	
SFC/SFE Grade 5.5™	152	152	40	18.14	838	CGA 320	

Purity Specifications (ppm unless otherwise noted)	SFC Carrier™	SFE Performance™	SFC/SFE Grade 5.5™
Liquid Phase Analysis			
Total ECD-Responsive Compounds	< 1.0 ppb*	< 0.1 ppb*	
Individual ECD-Responsive Compounds	< 0.1 ppb*	< 0.05 ppb*	
Total FID-Responsive Organic Compounds	< 5.0 ppb**	< 1.0 ppb**	< 100 ppb (Total)
Individual FID-Responsive Organic Compounds	< 1.0 ppb*	< 0.1 ppb*	
Gas Phase Analysis			
Gas Phase Hydrocarbons	< 0.5 ppm	< 0.5 ppm	< 0.5 ppm
Non-Volatile Residue	< 1 ppm	< 1 ppm	
Oxygen & Argon	< 2 ppm	< 2 ppm	< 2 ppm
Moisture	< 1 ppm	< 1 ppm	< 2 ppm

* Response proportional to [illegible]

** Response proportional to [illegible]

Technical Data

Mol. Wt.	44.01
Boiling Point	-109.3 °F (-78.5 °C)
Sp. Volume	8.74 cf/lb (0.547 m³/kg)
Critical Temp.	87.9 °F (31 °C)
Critical Press.	1071 psia (7381.5 kPa)
Flammable Limits	Nonflammable
Toxicity	TLV 5000 ppm
Corrosivity	[illegible]

Shipping Information

DOT/TDG Name	Carbon Dioxide
Hazard/TDG Class	2.2
ID No.	UN 1013
DOT/TDG Label	Nonflammable Gas
WHMIS Class	[illegible]
CAS No.	124-38-9
MSDS No.	[illegible]

[illegible]

[illegible]